# 國立交通大學

## 物理研究所

## 博士論文

金屬叢集的熔化行為:

依據瞬間正則模分析的次序參數

**Melting Behavior of Metallic Clusters:**

**An Order Parameter**

**by Instantaneous Normal Mode Analysis**

研究生：唐平翰

指導教授：吳天鳴　教授

中華民國一零二年六月

# 金屬叢集的熔化行為: 依據瞬間正則模分析的次序參數

# Melting Behavior of Metallic Clusters: An Order Parameterby Instantaneous Normal Mode Analysis

研 究 生：唐平翰　　Student：Ping-Han Tang

指導教授：吳天鳴　教授　　Advisor：Ten-Ming Wu

國 立 交 通 大 學

物 理 研 究 所

博 士 論 文

A Thesis

Submitted to Institute of Physics

College of Science

National Chiao Tung University

in partial Fulfillment of the Requirements

for the Degree of

Doctor of Philosophy

in

Physics

June 2013

Hsinchu, Taiwan, Republic of China

中華民國一零二年六月

# 金屬叢集的熔化行為:
# 依據瞬間正則模分析的次序參數

學生: 唐平翰　　指導教授:吳天鳴　教授

國立交通大學

物理研究所

## 摘要

在此論文中，我們探討兩種金屬叢集 $Ag_{17}Cu_2$ 和 $Ag_{14}$ 的熔化行為，並利用 isothermal Brownian type 的分子動力模擬搭配 Gupta 位能產生其低溫至高溫的組態。在這兩種叢集的比熱隨溫度的變化中，皆在較高溫度顯示出一主峰，我們定義為其熔化溫度，但它們之間的差別在於，在較低的溫度，$Ag_{14}$ 具有一個額外的前峰而 $Ag_{17}Cu_2$ 沒有。我們利用瞬間正則模（INM）分析剖析兩種叢集的動力學行為，並提出了一個新的次序參數，可以具體描述兩種叢集的熔化行為。INM 分析表明，一個叢集的次序參數可以被其瞬間振動態密度所定義，或者可由該叢集旋轉運動的三個正交特徵向量所描述，在此該叢集可視為一轉動剛體。對於所研究的兩種金屬叢集，我們的計算結果顯示，這兩種定義所求得的次序參數大致是一致的，對於低溫至高溫的熔化相變過程的闡述也與此兩種叢集各自的比熱曲線所推論的結果相吻合。此外，此次序參數也提供了更深入的圖像，關聯了叢集的熔化行為與過去成功地應用於塊材系統的熔化相變之對稱性破缺的概念。

**Melting Behavior of Metallic Clusters:**
**An Order Parameter**
**by Instantaneous Normal Modes Analysis**

**Student: Ping-Han Tang** **Advisor: Dr. Ten-Ming Wu**

**Institute of Physics**
**National Chiao Tung University**

# Abstract

In this thesis, we investigate the melting behaviors of two metallic clusters, $Ag_{17}Cu_2$ and $Ag_{14}$, which are generated by an isothermal Brownian-type molecular dynamics simulation with the empirical many-body Gupta potential from low to high temperatures. The temperature variations in the specific heat of these two clusters exhibit at higher temperature a main maximum, at which we define as the melting temperature, but at lower temperature they differ by $Ag_{14}$ possessing an additional prepeak and none in $Ag_{17}Cu_2$. The instantaneous normal mode (INM) analysis is used to dissect dynamics of the two clusters. We propose a new order parameter that specifically describes the melting behaviors of the two clusters. Our INM studies show that the order parameter of a cluster can be defined either by the INM vibrational density of states, or in terms of three orthogonal eigenvectors describing the rotational motions of the cluster by considering it as a rigid body. For the two metallic clusters studied, our calculated results indicate the mutual agreement of the order parameter by these two methods and also the consistent interpretation of the melting transitions at both lower and higher temperatures with those inferred from their respective specific heat. Furthermore, the new order parameter provides an insightful picture between the melting of clusters and the concept of broken symmetry, which is successfully applied to bulk systems for understanding the melting transition.

# 誌謝

感謝八年的碩博生涯中，能夠在吳老師的指導下順利畢業。也感謝父母全心全意的支持和協助，讓我能夠心無旁騖地完成學業。求學的過程中，有物理所的同學和學弟妹們的陪伴，那些一起鞭策念書，一起玩樂的日子，也讓我受益良多。最後，謝謝交大物理所提供了一個良好的研究環境，期待在接下來的博士後研究工作中，能夠盡情發揮所長。

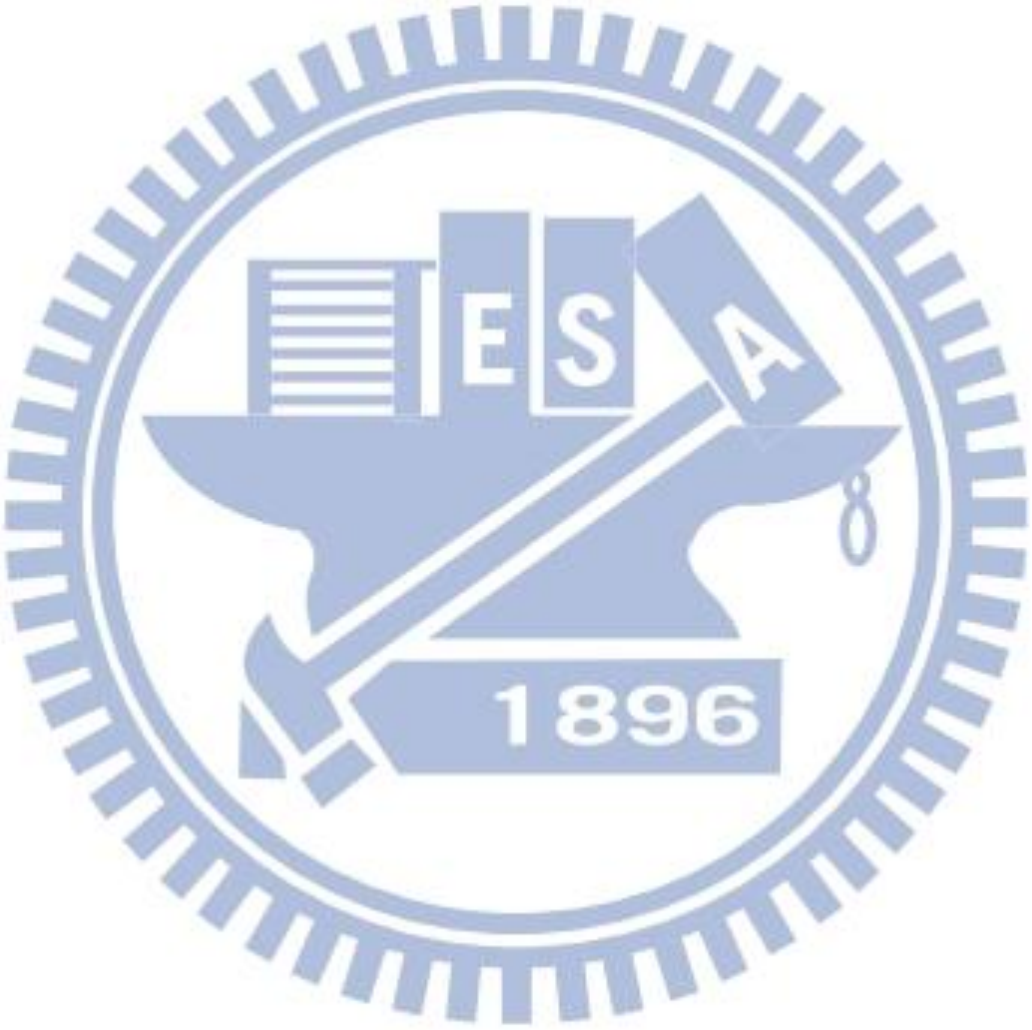

# List of Figures

# List of Tables



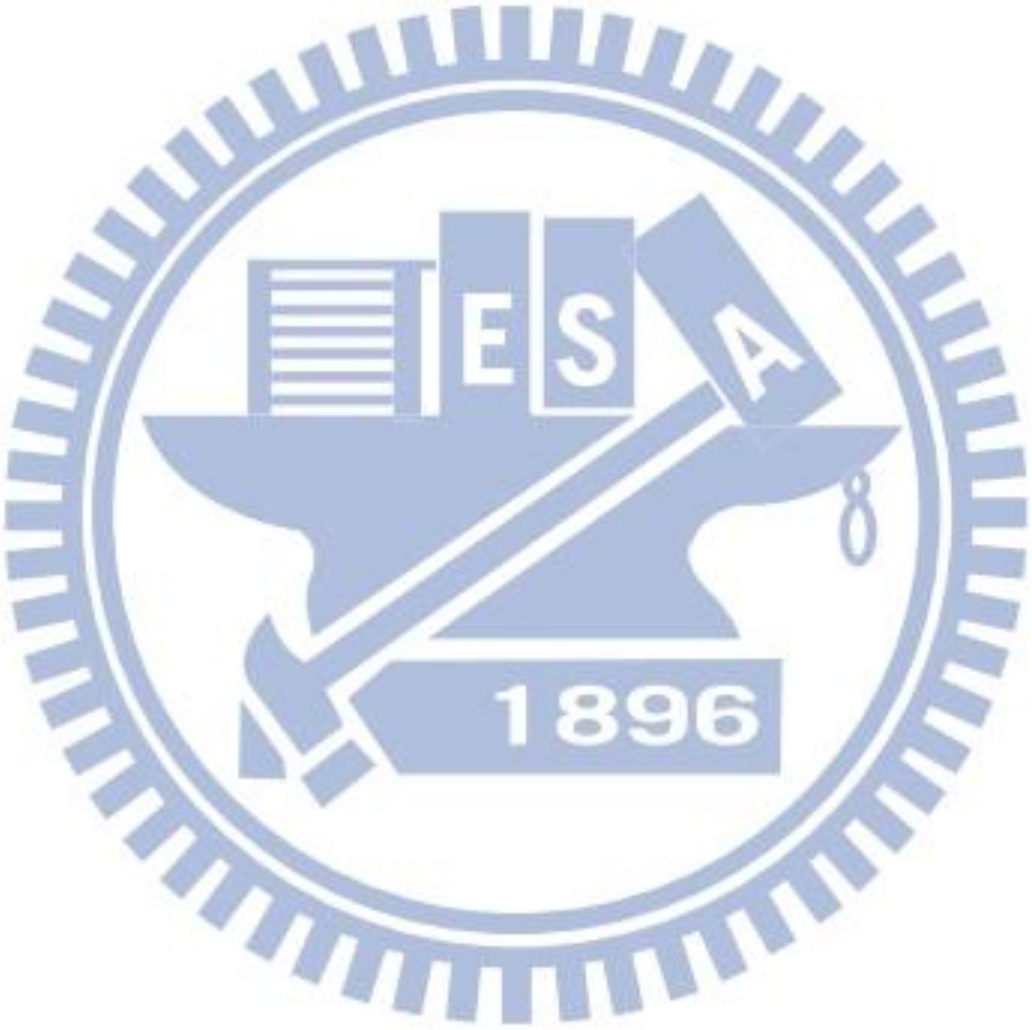

# Content

# Chapter 1
# Introduction

By the development of solid state physics and the refinement in experimental apparatuses, we gradually had comprehensive knowledge about the various phenomena of bulk systems. On the contrary, the physics of small cluster is not developed so rapidly and completely as the bulk system. In general, clusters are an aggregate of atoms that are too large compared to atoms and simple molecules but too small compared to bulk materials. As a result of these two extremes, clusters show extraordinary different properties. For example, a cluster does not have the same structure or atomic arrangements as its bulk counterpart and can change its structure with the addition of just one or few atoms [1]. On the other hand, since the surface-to-volume ratio is very small, the surface effect in bulk materials can be neglected with a good approximation. However, in the case of clusters, most of the atoms lie on the surface (extremely high surface-to-volume ratio) and such a rearrangement consequently produces a drastic effect in their physical and chemical properties [1- 16].

Cluster became a separate physical subject in 1980s when it was established experimentally that solid clusters are characterized by magic numbers of atoms [1]. Clusters composed of these numbers of atoms exhibit characteristically unusual parameters, e.g., maxima in the binding energies of atoms, in the cluster ionization potentials, in the electron affinities, and in the abundances, as functions of the number of atoms comprising the cluster. Magic numbers of solid clusters are observed as local maxima in mass spectra of clusters and also appear in photoionization spectra of clusters, although these require a specific analysis. In the aspect of cluster melting, the occurrence of magic number of cluster atoms is a prime reason for the non-monotonic dependence of these parameters on cluster size. Many experiments and later studies [17- 20] using several different techniques found that the melting temperatures of clusters reduce linearly as a function of the inverse of cluster radius *R*. However, the $1/\mathrm{R}$ dependence breaks down for particles less than around 500 atoms [21- 26]. This argument can be confirmed by recent experiments of charged clusters based on mobility measurements in gases for clusters of a given sort and size [27]. The reason for these is the structure-magic numbers corresponding to closed shells, ether of atoms or of electrons.

A general description of the melting transition in a cluster from the solid-like to liquid-like phase is far more complicated than its bulk counterpart [28]. Due to their finite sizes, the kind of sharp transition at a well-defined melting temperature often observed in bulk systems has been replaced in clusters by a more gradual transition that spans a temperature range. This finite-size-effect transition has been predicted to scale as the inverse of the cluster particle number [29, 30].

Thermodynamics, the melting point of a bulk material is the temperature at which the free energies of the material in the liquid and solid phases are precisely equal. For clusters, a finite range of the melting transition means the coexistence of the solid-like and liquid-like phases in the vicinity of the "melting point" of the cluster. This specific property of clusters was discovered first from computer simulations of Lennard-Jones clusters [31- 34] and soon thereafter was interpreted and explored further [35- 40] for Lennard-Jones clusters with completed atomic shells. Later, for small atomic systems, phase coexistence in the vicinity of the phase transition was found to be a universal property [41]. In the two-state model, in which only the solid-like and liquid-like phases are involved, this coexistence phenomenon involves the cluster passing back and forth in some random fashion between (or among) different phase-like isomers so that part of time the cluster spends in the solid-like phase and the rest of the time it resides in the liquid-like phase. The specific heat $C_V$ is by far still the most frequently used quantity to feature the melting transition of clusters. Differing from the bulk system, where there is a discontinuous jump at the melting, the temperature variation of $C_V$ in a cluster may exhibit a single main peak with perhaps a prepeak appearing at a lower temperature [21, 22, 25, 42- 46]. In either a bulk or a cluster, the melting temperature $T_m$ is customarily defined as the position of the maximum of the main peak.

A microscopic understanding of the melting transition in a cluster requires an order parameter that manifests its structural change from the solid-like to liquid-like phase. In the literature, such microscopic order parameters have indeed been proffered. The short-time average of temperature in the microcanonical ensemble provides a concrete evidence for the coexistence of isomers that were found to assume the solid-like and liquid-like phases within a temperature range and one quite often specifies the coexistence as a signature of cluster melting [35, 47- 49]. Structures of the clusters in the coexistence region were analyzed also by the method of common neighbor pairs [50]. Another quantity is the potential energy function commonly used for addressing the transition between two coexistence cluster isomers that are individually stable in the Landau free energy but are separated by an energy barrier [51]. There are, moreover, some geometric order parameters that are applied to characterize transition between two stable isomers and their coexistence [52], and these order parameters are calculated on the basis of the short-time average in simulations. An approach along the same line is the bond-orientational order parameter which is applied to investigate the structural variation of clusters along pathways in configuration space [53, 54]. The structural transitions of clusters are recently understood by using simultaneously two bond-orientational order parameters [55, 56]. Analogous to the Lindemann parameter used for bulk systems, the root-mean-square bond length fluctuation constant $\delta$ continues receiving much attention in computer simulations. An abrupt change of $\delta$ with temperature variation

means the structure of a cluster changes dramatically; however, the temperature for the sudden change in $\delta$ is usually not consistent with the melting point inferred from specific heat $C_V$. Thus, I remark here that the parameter $\delta$ does not work so well for clusters [45, 57, 58].

In this thesis, I will investigate the dynamics and melting behavior of metallic clusters from the viewpoint of potential energy landscape [59, 60] by exploiting the *instantaneous normal mode* (*INM*) analysis [61, 62]. The *INM* theory is an approach originally motivated for understanding the short-time dynamics of liquids from the point of view of the potential energy landscape [61, 62]. Considerable efforts have been devoted in recent years to transpose the INM theory into an analytic tool and fruitful dynamic properties of bulk systems have in fact been reported for simple liquids [63, 64], amorphous materials [65] biological systems [66], etc. On the other hand, the analyses for cluster dynamics and thermodynamics from the viewpoint of potential energy landscape have been developed independently [28, 67]. In a series of papers in 1990, Stratt and Adams [68-70] have advanced using the strategy of INM for clusters. These series of works have been inspired conceptually by the so-called inherent structures in a liquid [59, 60] and by early theoretical attempts of Berry *et al.* [35, 47, 48, 71-78], who developed statistical mechanical models for clusters, studied the various cluster dynamical properties and the finite-sized effect on cluster melting, and corroborated their findings by comparing them with the simulation data of argon clusters. Despite the insight provided by the INM theory, the tactics to exploit the cluster dynamics with the INM analysis remains an endeavor to be further explored. The major impediment lies in the particle number. Whereas in the bulk system the particle number is infinite in the thermodynamic limit, the particle number in the cluster is, however, finite. Even with a cluster that contains less than a hundred of particles, its energy landscape has a complex multi-dimensional space. One fundamental and unique feature for a cluster but not for a bulk system is that it has rotational motions about three principal axes. This unique trait for clusters causes the INM in some aspects different from the bulk systems and we propose that these particular aspects that are specific to clusters can be exploited to describe the melting phenomenon of a cluster.

I will study in this thesis the melting behaviors of two metallic clusters: $Ag_{17}Cu_2$ bimetallic cluster (BC) and $Ag_{14}$ pure metallic cluster (MC). The main difference in the melting behavior between $Ag_{14}$ and $Ag_{17}Cu_2$ clusters lies in the temperature variation of their $C_V$ which both possess a main maximum but the $C_V$ of $Ag_{14}$ exhibits in addition a prepeak at a lower temperature. The difference is resulted from that the structures of the two clusters at their respective lowest-energy state (LES) are quite different geometrically. According to the studies of $Cu_{14}$ [46] whose $C_V$ also shows a main peak and a prepeak as that of $Ag_{14}$, the origin of the prepeak is due to the migrational relocation of the floating atom in the cluster as the temperature of the cluster is raised from the LES.

In the context of the INM analysis, I propose a new order parameter $\tau(T)$ to interpret the melting behaviors of the two metallic clusters [79, 80]. Two general approaches are proposed to calculate $\tau(T)$. In one, $\tau(T)$ is defined in terms of the INM vibrational density of states of individual atoms; in another, $\tau(T)$ is defined considering the cluster as a rigid body with its rotational motions described by three orthogonal eigenvectors. For the two cluster studied in this thesis, we show numerically that the two

approaches for defining the order parameter dictate almost equivalent results. Also, our results indicate that this new order parameter $\tau(T)$ interprets pretty well the melting behavior of cluster and the predicted melting temperature for each of the two clusters is in fairly good agreement with that inferred from the specific heat $C_V$ of the cluster [81]. In addition, the order parameter $\tau$ ($T$) provides an insightful interpretation between the melting of clusters and the concept of broken symmetry which has been found successful in studies of the melting transition of bulk systems [82].

In Chapter two, I will give a brief review of the INM theory, in which the order parameter $\tau(T)$ will also be given in this Chapter. In Chapter three, I first give a brief introduction about the group theory and identify the symmetry entities for the lowest energy structures of the two clusters studied in this thesis. With the symmetry entities of each cluster, the atoms in the cluster are classified into subsets of atoms and this classification is found to be associated with the melting behavior of the cluster. In Chapter four, I give a brief description of the isothermal Brownian-type molecular dynamics simulation technique used in this thesis and introduce the Gupta empirical potential that was used for particle interactions in simulations. In the same chapter, the calculations for thermal and dynamical properties, including $C_V$ and $\delta$, are given as well. I present the results of the INM analysis for $Ag_{17}Cu_2$ and $Ag_{14}$ in Chapter five and six, respectively. In terms of the INM analysis, the results of the order parameter $\tau(T)$ for describing the melting behaviors of the two clusters are discussed in the two Chapters. In Chapter seven, I follow an intuitive method originally proposed by Madan, Keyes and Seeley to evaluate the diffusion coefficient of $Ag_{14}$ cluster, which also can be referred as another approach to describe the melting phenomenon of the cluster. Finally, conclusions of my thesis are given in Chapter eight.

# Chapter 2
# Instantaneous Normal Mode Theory for Clusters

## 2.1 INM theory for short time dynamics

In this section, I use the INM method to study the short time dynamics of metallic clusters. Consider a cluster of $n$ metallic atoms with mass $m_j$ ($j$ = 1,…,$n$), which may be of different species. The positions of these atoms in the 3-dimensional real space are denoted as

$$\boldsymbol{R} \equiv \left(\boldsymbol{r}_1, \cdots, \boldsymbol{r}_n\right) = \left(r_{1x}, r_{1y}, r_{1z}, \cdots, r_{nx}, r_{ny}, r_{nz}\right). \tag{2.1}$$

The potential energy $V(\boldsymbol{R})$ of the cluster evaluated at $\boldsymbol{R}$ is a function in 3$n$-dimensional space. The Lagrangian of the cluster under this coordinate system is written as

$$L = \frac{1}{2}\sum_j m_j \left(\dot{r}_{jx}^2 + \dot{r}_{jy}^2 + \dot{r}_{jz}^2\right) - V(\boldsymbol{R}). \tag{2.2}$$

In a short-time scale, a harmonic approximation can be applied to $V(\boldsymbol{R})$, which is expanded up to the second order terms with respect to the displacements of particles from an initial configuration $\boldsymbol{R}_0$. Therefore, the Lagrangian under the harmonic approximation at $\boldsymbol{R}_0$ is given as

$$\begin{aligned} L = {} & \frac{1}{2}\sum_j m_j \left(\dot{r}_{jx}^2 + \dot{r}_{jy}^2 + \dot{r}_{jz}^2\right) - V(\boldsymbol{R}_0) + \boldsymbol{F}(\boldsymbol{R}_0)\cdot(\boldsymbol{R}-\boldsymbol{R}_0) \\ & -\frac{1}{2}(\boldsymbol{R}-\boldsymbol{R}_0)\cdot\mathbf{D}(\boldsymbol{R}_0)\cdot(\boldsymbol{R}-\boldsymbol{R}_0) + \cdots \end{aligned}, \tag{2.3}$$

with

$$F_{j\nu}(\boldsymbol{R}_0) = -\left.\frac{\partial V(\boldsymbol{R})}{\partial r_{j\nu}}\right|_{\boldsymbol{R}_0}, \tag{2.4}$$

and

$$\mathrm{D}_{i\mu,jv}(\boldsymbol{R}_0)=\left.\frac{\partial^2 V(\boldsymbol{R}_0)}{\partial r_{i\mu}\partial r_{jv}}\right|_{\boldsymbol{R}_0}, \tag{2.5}$$

where $i\mu$ ($jv$) refers to the atom $i$ ($j$) that in Cartesian coordinates takes on $\mu = x$, $y$, $z$ ($v = x$, $y$, $z$). The $\boldsymbol{F}(\boldsymbol{R}_0)$ is a 3n-dimesional vector that describes the forces acted on particles at configuration $\boldsymbol{R}_0$; Appearing in the second-order term of the harmonic approximation of $V(\boldsymbol{R})$, $\mathbf{D}(\boldsymbol{R}_0)$ is the so-called 3*n*×3*n dynamic matrix*. In order to obtain the normal modes of the Lagrangian under the harmonic approximation, I introduce the mass-weighted coordinates:

$$\begin{aligned}\mathbf{Z}&\equiv(\mathbf{z}_1,\cdots,\mathbf{z}_n)=\left(\mathrm{z}_{1x},\mathrm{z}_{1y},\mathrm{z}_{1z},\cdots,\mathrm{z}_{nx},\mathrm{z}_{ny},\mathrm{z}_{nz}\right)\\&=\left(\sqrt{m_1}r_{1x},\sqrt{m_1}r_{1y},\sqrt{m_1}r_{1z},\cdots,\sqrt{m_n}r_{nx},\sqrt{m_n}r_{ny},\sqrt{m_n}r_{nz}\right)\end{aligned}. \tag{2.6}$$

In this transformation, the position vector of each atom is multiplied by the square root of its mass so that the mass-weighted coordinates are only a linear rescaling of the 3*n*-dimensional coordinates in real space. Accordingly, the approximated Lagrangian in the mass-weighted coordinates can be rewritten as:

$$\begin{aligned}L=&\frac{1}{2}\sum_j\left(\dot{\mathrm{z}}_{jx}^2+\dot{\mathrm{z}}_{jy}^2+\dot{\mathrm{z}}_{jz}^2\right)-V(\mathbf{Z_0})+\mathbf{f}(\mathbf{Z_0})\cdot(\mathbf{Z}-\mathbf{Z_0})\\&-\frac{1}{2}(\mathbf{Z}-\mathbf{Z_0})\cdot\boldsymbol{K}(\mathbf{Z_0})\cdot(\mathbf{Z}-\mathbf{Z_0})+\cdots\end{aligned}, \tag{2.7}$$

where

$$\mathrm{f}_{jv}(\mathbf{Z}_0)=-\left.\frac{\partial V(\mathbf{Z})}{\partial z_{jv}}\right|_{\mathbf{Z}_0}=-\frac{1}{\sqrt{m_j}}\left.\frac{\partial V(\boldsymbol{R})}{\partial r_{jv}}\right|_{\boldsymbol{R}_0}, \tag{2.8}$$

and

$$K_{i\mu,jv}(\mathbf{Z}_0)=\frac{1}{\sqrt{m_i m_j}}\left.\frac{\partial^2 V(\boldsymbol{R})}{\partial r_{i\mu}\partial r_{jv}}\right|_{\boldsymbol{R}_0}, \tag{2.9}$$

$\mathbf{f}(\mathbf{Z}_0)$ is the first derivative of the potential energy $V(\mathbf{Z})$ with respect to the mass-weighted coordinates at $\mathbf{Z}_0$ and is related to $\boldsymbol{F}(\boldsymbol{R}_0)$ through a factor $1/\sqrt{m_j}$. With the expression in Eq. (2.9) as a general form that can be applied for atoms of different species, $\boldsymbol{K}(\mathbf{Z}_0)$ is referred to as the *Hessian matrix*, whose elements are the second derivatives of the total potential energy with respect to the mass-weighted coordinates. Here, I define $\boldsymbol{\eta}$ as the displacements of atoms in a short-time scale from the initial mass-weighted configuration $\mathbf{Z}_0$. That is,

$$\boldsymbol{\eta}\equiv\mathbf{Z}-\mathbf{Z}_0=(\boldsymbol{\eta}_1,\cdots,\boldsymbol{\eta}_n)=\left(\eta_{1x},\ \eta_{1y},\ \eta_{1z},\ \cdots,\ \eta_{nx},\ \eta_{ny},\ \eta_{nz}\right). \tag{2.10}$$

By changing to the new variable $\boldsymbol{\eta}$, the approximated Lagrangian becomes as

$$L=\frac{1}{2}\sum_j^n\dot{\eta}_{jx}^2+\dot{\eta}_{jy}^2+\dot{\eta}_{jz}^2-V_0+\mathbf{f}\cdot\boldsymbol{\eta}-\frac{1}{2}\boldsymbol{\eta}\cdot\boldsymbol{K}\cdot\boldsymbol{\eta}. \tag{2.11}$$

In the next, the Hessian matrix $\boldsymbol{K}$ can be diagonalized by an orthogonal matrix $\boldsymbol{U}$ via the

equation

$$\omega_\alpha^2 = \sum_{i\mu}\sum_{j\nu} U_{\alpha,i\mu} K_{i\mu,j\nu} U_{\alpha,j\nu}\,, \tag{2.12}$$

where the orthogonal matrix $\boldsymbol{U}$ can be constructed by the 3$n$ eigenvectors obtained from diagonalization of the Hessian matrix $\boldsymbol{K}$ evaluated at the initial configuration $\boldsymbol{R}_0$. The 3$n$ normalized eigenvectors of $\boldsymbol{K}$ are denoted as $\mathbf{e}_j^\alpha$, with $\alpha = 1,\cdots,3n$, where $\mathbf{e}_j^\alpha$ is the 3-dimensional displacement vector of the $j$-th atom in the $\alpha$-th INM. The eigenvalues of the Hessian matrix $\boldsymbol{K}$ are given as $\omega_\alpha^2$, where $\omega_\alpha$ is referred as the frequency of the INM and, of course, depends on $\boldsymbol{R}_0$. Since the configurations at which the Hessian matrices are evaluated may not correspond in general to the local minima of $V(\boldsymbol{R})$, the eigenvalues are not guaranteed positive definite and the normal mode frequencies $\omega_\alpha$ may thus be either real or imaginary.

Accordingly, in terms of the orthogonal matrix $\boldsymbol{U}$, we introduce the INM coordinates $q_\alpha$, $\alpha = 1,\cdots,3n$, which are transformed from the displacement $\boldsymbol{\eta}$ via the following equation:

$$q_\alpha = \sum_{j\nu} U_{\alpha,j\nu}\eta_{j\nu} = \sum_{j\nu} \mathrm{e}_{j\nu}^\alpha \cdot \eta_{j\nu} \tag{2.13}$$

The $3n$ instantaneous normal mode coordinates $q_\alpha$ are linearly independent and form a basis set in the 3n-dimensional space of the mass-weighted coordinates. Following the coordinate transformation from $\boldsymbol{\eta}$ to $\boldsymbol{q}$, we notice that $\mathbf{f}$ defined in Eq. (2.8) should be transformed as

$$\tilde{\mathrm{f}}_\alpha = \sum_{j\nu} U_{\alpha,j\nu}\mathrm{f}_{j\nu} \tag{2.14}$$

with $\alpha = 1,\cdots,3n$. Therefore, the Lagrangian in the harmonic approximation can be expressed by the instantaneous normal modes coordinates as

$$L = \frac{1}{2}\sum_\alpha \dot{q}_\alpha^2 - V_0 + \sum_\alpha \tilde{\mathrm{f}}_\alpha q_\alpha - \frac{1}{2}\sum_\alpha \omega_\alpha^2 q_\alpha^2 \tag{2.15}$$

By substituting Eq. (2.15) into the Lagrange equation for each INM coordinate $q_\alpha$, we obtain 3$n$ independent differential equations which are given as

$$\ddot{q}_\alpha + \omega_\alpha^2 q_\alpha = \tilde{\mathrm{f}}_\alpha \tag{2.16}$$

By defining a shifted normal mode coordinate,

$$x_\alpha = q_\alpha - \frac{\tilde{\mathrm{f}}_\alpha}{\omega_\alpha^2}\,, \tag{2.17}$$

we have the following equation of motion for each INM degree of freedom in the $3n$-dimensional space

$$\ddot{x}_\alpha + \omega_\alpha^2 x_\alpha = 0\,. \tag{2.18}$$

The equation (2.18) is just the equation of motion of a simple harmonic oscillator with frequency $\omega_\alpha$ and its solution is simply given as:

$$x_\alpha(t) = x_\alpha(0)\cos(\omega_\alpha t) + \frac{\dot{x}_\alpha(0)}{\omega_\alpha}\sin(\omega_\alpha t)\,, \tag{2.19}$$

where $x_\alpha(0)$ is related to the initial positions of atoms in the cluster and $\dot{x}_\alpha(0)$, which is the time derivative of $x_\alpha(t)$ at initial, is associated with the velocities of the atoms. In the α-th INM coordinate,

$$\dot{x}_\alpha = \dot{q}_\alpha\,. \tag{2.20}$$

After substituting the solution in Eq. (2.19) into Eq. (2.17), the instantaneous normal modes $q_\alpha$ at time t are explicitly written as

$$q_\alpha(t) = x_\alpha(0)\cos(\omega_\alpha t) + \frac{\dot{x}_\alpha(0)}{\omega_\alpha}\sin(\omega_\alpha t) + \frac{\tilde{f}_\alpha}{\omega_\alpha^2}\,. \tag{2.21}$$

With the inverse transformation of Eq. (2.13), we can obtain the short-time evolution of the cluster in the mass-weighted coordinate system.

In terms of Eq. (2.21), we can determine a harmonic approximation for the short-time dynamics of a cluster. For a cluster system, the dynamics includes the translation and rotation of the whole cluster and vibrations among particles in the cluster. The derivation for the INM theory is quite general and applicable to any clusters of single species or alloys at any temperatures. However, for the physical quantities related to the vibrational motions of a cluster, like the velocity autocorrelation function and its power spectrum that will be considered in Sec. 2.2.4, the contributions due to the translational and rotational motions of the cluster should be excluded. In the next section, I will introduce the method to determine the translational and rotational INNs and show how to exclude their contributions from the INM analysis

## 2.2 Instantaneous normal mode analysis

### 2.2.1 INM density of states

In INM theory, the most fundamental physical quantity is the density of states. The normalized *INM density of states* (*DOS*) of a *n*-particle cluster is written as

$$D(\omega)=\left\langle \frac{1}{3n}\sum_{\alpha=1}^{3n}\delta(\omega-\omega_\alpha)\right\rangle, \tag{2.22}$$

where the brackets indicate an ensemble average over cluster configurations. Generally, $D(\omega)$ is divided into two lobes, $D^{(s)}(\omega)$, and $D^{(u)}(\omega)$, which are the DOS of the stable INMs (denoted by the superscript *s*) with real frequencies $\omega$ and the unstable INMs (denoted by the superscript *u*) with imaginary frequencies $\omega_\alpha = i\lambda_\alpha$, respectively. The normalization of $D(\omega)$ yields a unit area under the curves of $D^{(s)}(\omega)$ and $D^{(u)}(\omega)$, which are usually plotted in the positive and negative axes of $\omega$, respectively[62, 63].

Among the INMs, there are three zero-eigenvalue normal modes, which correspond to the three-dimensional translational motion of the center-of-mass of the system. For the bulk system, such as a liquid or glass, the remaining INMs describe the vibrational motions of the atoms, whereas for the finite-sized system such as a cluster which composes of given number of atoms, the remaining INMs include contributions from three rotational degrees of freedom of the whole cluster and 3*n*-6 vibrational degrees of freedom among atoms. In the following, I provide two methods to distinguish the rotational INMs from the remaining INMs.

### 2.2.2 Rotational INMs

At given instant, the degrees of freedom associated with the rotational motions of the whole cluster can be sorted out by the following two methods [60, 83]:

*Method I:* In one method, referred as *Method I* in this thesis, the clusters are assumed to have an extremely weak rotation-vibration coupling so that a cluster at given instant is treated as a rigid body. Based on the conservation of the total angular momentum [84], the normalized eigenvectors of the three purely rotational modes, denoted as $\left(R'_x, R'_y, R'_z\right)$, of a cluster at a configuration $\boldsymbol{R}_0$ can be expressed as [79, 85] (see A.1)

$$\mathbf{e}_j^{R'_x}=\sqrt{\frac{m_j}{I_x}}\begin{bmatrix}0\\-r'_{jz}\\r'_{jy}\end{bmatrix},\ \mathbf{e}_j^{R'_y}=\sqrt{\frac{m_j}{I_y}}\begin{bmatrix}r'_{jz}\\0\\-r'_{jx}\end{bmatrix},\ \mathbf{e}_j^{R'_z}=\sqrt{\frac{m_j}{I_z}}\begin{bmatrix}-r'_{jy}\\r'_{jx}\\0\end{bmatrix}, \tag{2.23}$$

where $r'_{j\mu}(\mu = x, y, z)$ are the Cartesian position coordinates of the *j*-th atom in the body frame of the

cluster whose origin is chosen at the center-of-mass. In this body frame, the coordinate axes coincide with the principal axes of the cluster. With respect to each one of the three principal axes, the moment of inertia $I_\mu$ is defined as

$$I_\mu = m\sum_{j=1}^{n}\left(r'^2_{j\nu} + r'^2_{j\eta}\right), \tag{2.24}$$

where we assume $\mu \neq \nu \neq \eta$ are cyclic in *x*, *y*, and *z*. In this method, the rotational and vibrational degrees of freedom at an instant are assumed to be completely decoupled. The three purely rotational eigenvectors are mutually orthonormal and they form a set of basis vectors in the 3-dimensional subspace which are used to describe the rotational degrees of freedom of a cluster configuration at given instant. However, one should notice that the purely rotational bases of cluster configurations at two successive instants may not be transformable by merely rotating the principal axes of the cluster in a real space. The reason is that there exists in a cluster the inherent rotation-vibration couplings which may cause a mixing between the instantaneous subspaces of the rotation and vibration from one instant to the next.

The procedure to exclude the degrees of freedom associated with the three purely rotational modes from the Hessian matrix is the standard projection technique [70, 85], in which a *3n*×*3n* projection matrix $\boldsymbol{Q}(\boldsymbol{R}_0)$ constructed from three purely rotational eigenvectors $\mathbf{e}_j^\alpha$, with $\left(\alpha = R'_x, R'_y, R'_z\right)$, is defined as

$$Q_{i\mu,j\nu}(\boldsymbol{R}_0) = \sum_{\alpha=R'_x,R'_y,R'_z} \mathrm{e}^\alpha_{i\mu}\cdot \mathrm{e}^\alpha_{j\nu}, \tag{2.25}$$

where $\mathrm{e}^\alpha_{j\nu}$, with $\nu = x, y, z$ is the Cartesian component of $\mathbf{e}_j^\alpha$. To project out the rotational degrees of freedom, one defines a projected Hessian matrix as

$$\boldsymbol{K}^{(p)}(\boldsymbol{R}_0) = \left[\mathbf{I}_{3n} - \boldsymbol{Q}(\boldsymbol{R}_0)\right]\cdot \boldsymbol{K}\left(\boldsymbol{R}_0\right)\cdot\left[\mathbf{I}_{3n} - \boldsymbol{Q}(\boldsymbol{R}_0)\right], \tag{2.26}$$

where $\mathbf{I}_{3n}$ is the *3n* × *3n* unit matrix. The diagonalization of $\boldsymbol{K}^{(p)}(\boldsymbol{R}_0)$ then yields purely vibrational eigenvectors with nonzero eigenvalues. Implicit in this procedure is that the clusters under consideration are close to rigid and their rotational and vibrational degrees of freedom are supposedly decoupled. This method works generally, however, for those clusters in which the rotation-vibration couplings are extremely weak. However, under the INM approximation, the instantaneous rotation of a cluster is considered as a rigid body with the cluster structure at the instant and its total angular momentum is regarded as a constant so that one may simply apply this method for the cluster configurations at every instant.

*Method II:* Strictly speaking, the three purely rotational eigenvectors are not the eigenmodes of the Hessian matrix $\boldsymbol{K}(\boldsymbol{R}_0)$ but approximate ones when the rotation-vibration couplings become significant. In another method, referred as *Method II* in this thesis, it was pointed out by Adams and Stratt [70] that the three rotational INMs in the cluster are coupled with the vibrational degrees of freedom resulting in the mixing modes of the former and the extent of mixing increases with cluster temperature. The authors then proposed another projection scheme to separate out the rotational contributions from the INM

density of states. Technically, one appeals to the three rotational eigenmodes in the Hessian matrix $\boldsymbol{K}(\boldsymbol{R_0})$ that possess the largest angular momentum values and The three INMs are denoted as $(L_1, L_2, L_3)$. For each one of the INMs, the normalized INM eigenvector is proportional to the velocity whose vector property describes the instantaneous directions of the atomic motions in the center-of-mass coordinate system of the cluster. Accordingly, the magnitude of the rotational angular momentum in the INM $\alpha$, with $\alpha = L_1$, $L_2$, $L_3$ can be approximated as

$$L_\alpha = c\left|\sum_{j=1}^{n}\sqrt{m_j}\left(\boldsymbol{r}_j \times \mathbf{e}_j^\alpha\right)\right|, \tag{2.27}$$

where $\boldsymbol{r}_j$ is the position vector of the $j$-th atom with mass $m_j$ and $c$ is a proportionality constant between the instantaneous velocities of particles and the normalized INM eigenvector. In this scheme, the rotational INMs are thus recognized as three with the largest $L_\alpha$ values. Here, two remarks are in order. First, with the INM eigenvectors $\mathbf{e}_j^\alpha$ defined above in the mass-weighted form, $c$ is different from the one given in Ref. [70] for atoms with equal mass. Second, the instantaneous cluster motions in the three rotational INMs generally behave as rotations of the whole cluster, although mixing with vibrations is to some extent seen among atoms.

The three purely rotational modes obtained from *Method I* construct a rotational subspace for describing the rotational motion of the whole cluster, even at a configuration that is not at a local minima of potential landscapes. However, in *Method II*, the three INM eigenvectors associated with $(L_1, L_2, L_3)$ of a cluster coincide with those of the purely rotational modes, only for the configuration of the cluster at a local minimum in the potential energy landscape. If a cluster configuration is deviated from a local minimum, the three INMs $(L_1, L_2, L_3)$ would mix in some extent with the vibrational natures. Accordingly, to examine the overlap between the subspace spanned by the INM eigenvectors of $(L_1, L_2, L_3)$ and that by the purely rotational modes $(R'_x, R'_y, R'_z)$, I define the following quantity:

$$J(L_k) = \left\langle \sum_{\eta=x,y,z}\left(\sum_{j=1}^{n}\mathbf{e}_j^{L_k}\cdot\mathbf{e}_j^{R'_\eta}\right)^2\right\rangle. \tag{2.28}$$

As so defined, $J(L_k)$ measures the projection of the rotational INM eigenvector $\mathbf{e}_j^{L_k}$ onto the subspace spanned by the eigenvectors of the purely rotational modes $(R'_x, R'_y, R'_z)$. Note that the two subspaces are completely overlapped whenever $J(L_k) = 1$, $k = 1, 2, 3$, whereas for $J(L_k)$<1 the eigenvector $\mathbf{e}_j^{L_k}$ hybridizes with the degrees of freedom of the vibrational INMs and the two subspaces are not completely overlapped; the less the value of $J(L_k)$ is, the stronger is the hybridization.

### 2.2.3 Vibrational INM density of states

Return to the theme of vibrational INM density of states of clusters. The definition in Eq. (2.22) should be modified by excluding the three-translational and three-rotational INMs and the histogram for the frequencies of the remaining INMs gives rise to the normalized *vibrational INM DOS* of a cluster,

which is expressed as

$$D_{vib}(\omega)=\left\langle \frac{1}{3n-6}\sum_{\alpha=1}^{3n-6}\delta(\omega-\omega_\alpha)\right\rangle. \tag{2.29}$$

To make further progress, I introduce the projector $\hat{P}_j^\alpha$, which sorts out the INM of the atom *j* in a cluster with the eigenmode $\alpha$. In Cartesian coordinates *x*, *y*, and *z*, it reads

$$\hat{P}_j^\alpha=\left|\mathbf{e}_j^\alpha\right|^2=\mathbf{e}_j^\alpha\cdot\mathbf{e}_j^\alpha. \tag{2.30}$$

Due to the normalization of an INM eigenvector, $\hat{P}_j^\alpha$ obeys the following two sum rules:

$$\sum_{j=1}^{n}\hat{P}_j^\alpha=1, \tag{2.31}$$

and

$$\sum_{\alpha=1}^{3n}\hat{P}_j^\alpha=3, \tag{2.32}$$

where the equation in (2.32) is due to the completeness of all INMs of a Hessian matrix and the numeric constant 3 is due to the 3 degrees of freedom of each atom. The projectors for the translation and rotation of the cluster are defined accordingly and are, respectively, expressed as

$$\hat{P}_j^T\equiv\hat{P}_j^{T_x}+\hat{P}_j^{T_y}+\hat{P}_j^{T_z}, \tag{2.33}$$

and

$$\hat{P}_j^R\equiv\hat{P}_j^{L_1}+\hat{P}_j^{L_2}+\hat{P}_j^{L_3}, \tag{2.34}$$

where $(T_x,T_y,T_z)$ are the three translational INMs and $(L_1,L_2,L_3)$ are the three rotational INMs sorted out by *Method II*. In addition, the $\hat{P}_j^{vib}$ is used to define the total-vibrational projector of a cluster. That is

$$\hat{P}_j^{vib}=\sum_{\alpha=1}^{3n-6}\hat{P}_j^\alpha. \tag{2.35}$$

Hence, the completeness relation in Eq. (2.32) can be separated into the translational, rotational and vibrational components

$$\sum_{\alpha=1}^{3n}\hat{P}_j^\alpha=\hat{P}_j^T+\hat{P}_j^R+\hat{P}_j^{vib}=3. \tag{2.36}$$

With $\hat{P}_j^\alpha$, one can calculate the *j*-th atom contribution to the vibrational INM DOS via the formula

$$D_j(\omega)=\left\langle \frac{1}{3n-6}\sum_{\alpha=1}^{3n-6}\hat{P}_j^\alpha\delta(\omega-\omega_\alpha)\right\rangle. \tag{2.37}$$

Obviously $D_j(\omega)$ is not normalized. With $D_j(\omega)$ so defined, the vibrational INM DOS of all atoms in a cluster, $D_{vib}(\omega)$, satisfies another sum rule,

$$D_{vib}(\omega)=\sum_{j=1}^{n}D_j(\omega). \tag{2.38}$$

Note that $D_j(\omega)$ includes also the real- and imaginary frequency lobes, which are given respectively as

$$D_j^{(s)}(\omega)=\left\langle \frac{1}{3n-6}\sum_{\alpha=1}^{\mathrm{Re}}\hat{P}_j^{\alpha}\delta(\omega-\omega_\alpha)\right\rangle,\ D_j^{(u)}(\lambda)=\left\langle \frac{1}{3n-6}\sum_{\alpha=1}^{\mathrm{Im}}\hat{P}_j^{\alpha}\delta(\lambda-\lambda_\alpha)\right\rangle, \tag{2.39}$$

where the summations for the DOS of the stable and unstable lobes are over INMs of the real and imaginary frequencies, respectively. Therefore, the integration of $D_j(\omega)$ over frequency yields

$$I_j=\int D_j(\omega)d\omega=\int_0^{\infty}D_j^{(s)}(\omega)d\omega+\int_0^{\infty}D_j^{(u)}(\lambda)d\lambda=\frac{1}{3n-6}\left\langle\sum_{\alpha=1}^{3n-6}\hat{P}_j^{\alpha}\right\rangle. \tag{2.40}$$

Since $D_j(\omega)$ is not normalized, the value of $I_j$ is not one. Thus, $I_j$ is an ensemble average of all vibrational projectors associated with the *j*-th atom. Furthermore, due to the sum rule of $\hat{P}_j^{\alpha}$ in Eq. (2.36), $I_j$ is governed moreover by the following equation:

$$I_j=\frac{1}{3n-6}\left\langle\sum_{\alpha=1}^{3n-6}\hat{P}_j^{\alpha}\right\rangle=\frac{1}{3n-6}\left(3-P_j^T-P_j^R\right)=\frac{1}{3n-6}P_j^{vib}, \tag{2.41}$$

where the translational and rotational projections $P_j^T\equiv\langle\hat{P}_j^T\rangle$ and $P_j^R\equiv\langle\hat{P}_j^R\rangle$ are the ensemble averages of $\hat{P}_j^T$ and $\hat{P}_j^R$ of atom *j*, respectively, and $P_j^{vib}$ is the ensemble average of total-vibrational projector $\langle\hat{P}_j^{vib}\rangle$. The $I_j$ in Eq. (2.41) is, thus, cast into a form readily related to the translational and rotational projections of the INMs. In the event that a cluster experiences no external force, the $P_j^T$ value is constant for all cluster configurations. In this case, $I_j$ is simply related to the negative of the rotational projection $P_j^R$.

In the another aspect, for the cluster at lowest energy state (LES), the vibrational INM DOS is defined similarly as

$$D_{vib}^{(LES)}(\omega)=\sum_{\beta=1}^{3n-6}\delta_{\omega,\omega_\beta}, \tag{2.42}$$

where $\omega_\beta$ is the $\beta$-th vibrational-mode frequency pertaining to the LES and the symbol $\delta_{\omega,\omega_\beta}$ is the Kronecker delta. Furthermore the corresponding projectors can be employed to calculate the *j*-th atom vibrational INM DOS in the LES and we have (cf. Eq. (2.37))

$$D_j^{(LES)}(\omega)=\frac{1}{3n-6}\sum_{\beta=1}^{3n-6}\hat{P}_j^{\beta}\delta_{\omega,\omega_\beta}. \tag{2.43}$$

The summation of $D_j^{(LES)}(\omega)$ over all frequencies leads accordingly to

$$I_j^{(LES)}=\frac{1}{3n-6}\sum_{\beta=1}^{3n-6}\hat{P}_j^{\beta}, \tag{2.44}$$

which can easily be shown to satisfy

$$I_j^{(LES)} = \frac{3 - P_j^T - P_j^R}{3n - 6}. \tag{2.45}$$

I emphasize that $I_j$ defined in this subsection is a crucial quantity whose thermal variation sheds light on the melting behavior of a cluster that I will address below.

### 2.2.4 Relation to velocity autocorrelation function

The displacements of atoms in a cluster are confined within a finite region in space and do not continue to increase with time [68] as in the bulk liquids whose mean square displacements of atoms show the asymptotic behavior of growing linearly with time so that, predicted by mean square displacements of its atoms, the diffusion coefficient of atom in a cluster should be zero. As a result, there remains an ambiguity in the study of the dynamical properties of a cluster that resorts to the mean-square displacement of atoms. Even so, the velocity autocorrelation function (VAF) also provides fruitful information of dynamical properties in a cluster, some methods were proposed to calculate the diffusion coefficient of a cluster via the VAF and will be discussed in the Chapter 7. Here, I will discuss the VAF and its power spectrum of a cluster. The definition of the VAF for a cluster is given as the following formula

$$C(t) = \frac{\left\langle \sum_j^n \boldsymbol{v}_j(0) \cdot \boldsymbol{v}_j(t) \right\rangle}{\left\langle \sum_j^n \boldsymbol{v}_j(0) \cdot \boldsymbol{v}_j(0) \right\rangle}, \tag{2.46}$$

where $n$ is the number of atoms in a cluster and $\boldsymbol{v}_j$ is the velocity of the *j*-th atom. The VAF defined by Eq. (2.46) is a general form adequate to a cluster even containing different species of atoms. On the other hand, in the calculation of the VAF due to the vibrational motions of atoms in a cluster, the velocities of individual atoms should be corrected by subtracting out the parts corresponding to translational as well as the rotational motion of the whole cluster. Failing to make these corrections will result in a non-zero value of the long-time limit of $C(t)$. For a cluster at low temperatures, the $C(t)$ will exhibits a behavior like a under-damping oscillation as a result of atoms in the solid-like structure vibrating at a equilibrium position owing to thermal energy. As raising to high temperatures, the behavior at the beginning of $C(t)$ will decrease to a dip and, after subsequently going through the dip, follows by a decaying tail, which is a characteristics of liquid-like behavior corresponding to the diffusion phenomenon. Further, one can examine the behavior of the VAF by its related power spectrum,

$$\Omega(\omega) = 2\int_0^\infty C(t)\cos(\omega t)dt. \tag{2.47}$$

Since the VAF is an even function in time, its power spectrum is evaluated from the Fourier cosine transformation. In the solid-like phase, the power spectrum behaves like a superposition of many

spikes broadened by thermal disturbance; in the liquid-like phase, the power spectrum will become smoother and, at zero frequency, give a nonzero value related to the diffusion phenomenon. These features are similar as for the bulk systems.

Now, I will give an short-time approximation for the VAF with its definition in Eq. (2.46) by considering the velocities of particles in Eq. (2.46) described under the INM coordinates $q_\alpha$, so that the associated power spectrum in Eq. (2.47) also can be described under INM approximation. I give the formal derivation in Appendix A.2. By connecting the relation between the INM coordinates and mass-weighted coordinates in Eq. (2.13) and the equation of motion of INMs in Eq. (2.21), we have

$$C(t) \approx \frac{\sum_j^n \frac{1}{m_j}\left(\int_0^\infty D_j^{(s)}(\omega)\cos(\omega t)d\omega + \int_0^\infty D_j^{(u)}(\lambda)\cosh(\lambda t)d\lambda\right)}{\sum_j^n \frac{1}{m_j}\left(\int_0^\infty D_j^{(s)}(\omega)d\omega + \int_0^\infty D_j^{(u)}(\lambda)d\lambda\right)}, \qquad (2.48)$$

where $D_j^{(s)}(\omega)$ and $D_j^{(u)}(\lambda)$ are defined in Eq. (2.39), and the numerator and the denominator have been separated into the contributions due to the stable and unstable branches. I should point out that the formula in Eq. (2.48) with both stable and unstable branches accurately predicts $C(t)$ in the short-time regime; however, the prediction diverges badly in the long-time limit due to the imaginary-frequency term. In the stable-INM approximation [86, 87], in which the contribution due to the imaginary-frequency lobe is neglected, the $C(t)$ is further simplified to

$$C^{\mathrm{INM,s}}(t) = \frac{\sum_j^n \frac{1}{m_j}\int_0^\infty D_j^{(s)}(\omega)\cos(\omega t)d\omega}{\sum_j^n \frac{I_j^{(s)}}{m_j}}, \qquad (2.49)$$

with

$$I_j^{(s)} = \int_0^\infty D_j^{(s)}(\omega)d\omega, \qquad (2.50)$$

After making the inverse cosine transform for Eq.(2.49), the power spectral density in the stable-INM approximation is given as

$$\Omega^{\mathrm{INM,s}} \equiv \frac{\pi\sum_j D_j^{(s)}(\omega)/m_j}{\sum_j^n I_j^{(s)}/m_j}, \qquad (2.51)$$

which plays a similar role as that $\Omega(\omega)$ described above in Eq.(2.47). At low temperatures the imaginary-frequency INMs are absent and the two quantities $\Omega^{\mathrm{INM,s}}$ and $\Omega(\omega)$ are expected to be equal.

If the cluster is composed by atoms of the same species, with $m_j = m$ for all $j$ in Eq.(2.48), one cancels out $1/\mathrm{m}$ there. Also, by Eq. (2.38), we know that $D_{vib}^{(s)}(\omega) = \sum_j^n D_j^{(s)}(\omega)$ and $D_{vib}^{(u)}(\omega) = \sum_j^n D_j^{(u)}(\omega)$, and the denominator in Eq. (2.48) become to one due to Eq. (2.40), namely,

$$C(t) \approx \int_0^\infty D_{vib}^{(s)}(\omega)\cos(\omega t)d\omega + \int_0^\infty D_{vib}^{(u)}(\lambda)\cosh(\lambda t)d\omega . \quad (2.52)$$

Correspondingly, in the stable-INM approximation, the $C(t)$ is further simplified into

$$C^{\mathrm{INM,s}}(t) = \frac{1}{I^{(s)}}\int_0^\infty D^{(s)}(\omega)\cos(\omega t)d\omega , \quad (2.53)$$

with the renormalized factor,

$$I^{(s)} = \int_0^\infty D_{vib}^{(s)}(\omega)d\omega . \quad (2.54)$$

The power spectral density in the stable-INM approximation is given as

$$\Omega^{\mathrm{INM,s}} \equiv \pi D^{(s)}(\omega)/I^{(s)} , \quad (2.55)$$

which can be compared with, $\Omega(\omega)$, the power spectrum of a cluster defined in Eq. (2.47).

In general, the behaviors of $C(t)$ and its power spectral density $\Omega(\omega)$ are very different between bulk systems in the solid and liquid phases. However, for a cluster system, not only the two quantities vary with temperature, but also the contributions of individual atom to $C(t)$ and $\Omega(\omega)$ are very sensitive with its corresponding special position in the cluster structure at of lower temperatures. Thus a method that gives a quantitative and deeper insight is to dissect the contributions of individual atom to the VAF of the whole cluster, and I consider the normalized VAF for the $j$-th atom in a cluster as

$$C_j(t) = \frac{\langle \boldsymbol{v}_j(0)\cdot\boldsymbol{v}_j(t)\rangle}{\langle \boldsymbol{v}_j(0)\cdot\boldsymbol{v}_j(0)\rangle} . \quad (2.56)$$

Here, the subscript $j$ of $C_j(t)$ denotes the specified atom that contributes to the VAF. In liquid, the average over atoms in $C(t)$ is carried out to improve the statistical accuracy since the dynamical motion for each of all atoms is assumed the same, while in the solid, in which atoms are fixed in position, and characterized by arrangements of their neighbors, $C_j(t)$ distinct from each other depend on their corresponding local structures. This feature for cluster systems will become more explicit than bulk system due to its shell structures. From Eq. (2.56), one can examine the behavior of the VAF of individual atom and its related power spectrum,

$$\Omega_j(\omega) = 2\int_0^\infty C_j(t)\cos(\omega t)dt . \quad (2.57)$$

Since the $C_j(t)$ exhibits different characteristics for atoms at different positions in the structure of the cluster. The atomic power spectrum of the solid-like phase will depend on its position in the structure. However, in the liquid-like phase, the atoms of a cluster will mix together and are not characterized by their positions. Consequently, the atomic power spectra averaged over configurations are only distinguishable for the species with different masses.

According to the definition of $C_j(t)$ in Eq. (2.56), there is no summation over atoms. In the INM approximation, $C_j(t)$ can be formulated readily by inferring from Eq.(2.48) as

$$C_j(t) \approx \frac{\int_0^\infty D_j^{(s)}(\omega)\cos(\omega t)d\omega + \int_0^\infty D_j^{(u)}(\lambda)\cosh(\lambda t)d\omega}{\int_0^\infty D_j^{(s)}(\omega)d\omega + \int_0^\infty D_j^{(u)}(\lambda)d\omega}, \tag{2.58}$$

where the denominator equals $I_j$ and the INM DOS have been separated into the stable and unstable branches as in Eq. (2.48). In the stable-INM approximation [86, 87], the $C_j(t)$ is further simplified to

$$C_j^{\mathrm{INM,s}}(t) = \frac{1}{I_j^{(s)}}\int D_j^{(s)}(\omega)\cos(\omega t)d\omega, \tag{2.59}$$

with the renormalized factor,

$$I_j^{(s)} = \int_0^\infty D_j^{(s)}(\omega)d\omega. \tag{2.60}$$

By an inverse cosine transform for Eq. (2.59), the atomic power spectrum in the stable-INM approximation is given as

$$\Omega_j^{\mathrm{INM},s} \equiv \pi D_j^{(s)}(\omega)/I_j^{(s)}. \tag{2.61}$$

Also, at low temperatures the imaginary-frequency INMs are absent and the two quantities $\Omega_j^{\mathrm{INM,s}}$ and $\Omega_j(\omega)$ are expected to be equal.

## 2.3 Order parameter by instantaneous normal modes

In Sec. 2.2.3, for an cluster of $n$ atoms, I define a quantity $I_j$ of atom $j$ in Eq. (2.41), which is referred as a summation of all vibrational projections, $P_j^{vib}$, of atom $j$. The $I_j$ values of the cluster may be classified according to the point group character of the cluster structure at the LES. The group character of the LES is well identified so that the $I_j$ values of all atoms may be split into a number of branches each of which corresponds to a subset of the structure. Moreover, as the structure of a cluster is deformed from the LES by thermal fluctuation, the symmetry of the LES is broken and the group character of the cluster is different from that of the LES. This causes the $I_j$ values of the atoms, which are originally split into a number of branches, to be defiled and then mixed up. As the temperature of the cluster raises to the melting point, the $I_j$ values of all atoms will merge entirely into a small range, within which the $I_j$ value of each atom fluctuates, as a result of the almost destruction of the LES. At this stage, the atoms in the cluster are unable to distinguish by the symmetry character of the lowest energy structure.

In the following, I define an order parameter $\tau(T)$ for a pure cluster of n atoms by the standard deviation of $I_j$ values of all atoms at a temperature $T$ so that the melting phenomenon of the cluster can be characterized by this new order parameter. The order parameter is given as

$$\tau(T) = \frac{\sigma_I(T)}{\sigma_I(0)}, \tag{2.62}$$

with

$$\sigma_I(T) = \sqrt{\overline{I_j^2} - \left(\overline{I_j}\right)^2}, \tag{2.63}$$

and

$$\overline{I_j^\ell} = \frac{1}{n}\sum_{j=1}^{n} I_j^\ell, \tag{2.64}$$

where $\ell$ =1 or 2 and the bar notation in Eq. (2.64) denotes an arithmetic average over atoms in the cluster. Physically, the order parameter $\tau(T)$ is a quantity measuring the ordering of a cluster's structures at a finite temperature relative to its LES. At low temperatures, atoms generally vibrate about the equilibrium positions of the LES so that the value of $\tau(T)$ is of the order of unity. As the structure of a cluster becomes liquid-like at a high temperature, $\tau(T)$ approaches to an extremely small value due to the finite size of the cluster.

By Eq. (2.41), the order parameter $\tau(T)$ can be written alternatively in terms of the rotational projection $P_j^R$, viz.,

$$\tau(T) = \frac{\sigma_R(T)}{\sigma_R(0)}, \tag{2.65}$$

where

$$\sigma_R(T) = \sqrt{\left(P_j^R\right)^2 - \left(\overline{P_j^R}\right)^2}, \tag{2.66}$$

with

$$\overline{P_j^R} = \frac{1}{n}\sum_{j=1}^{n}\left\langle \hat{P}_j^R \right\rangle, \tag{2.67}$$

and

$$\overline{\left(P_j^R\right)^2} = \frac{1}{n}\sum_{j=1}^{n}\left\langle \hat{P}_j^R \right\rangle^2, \tag{2.68}$$

Equations (2.67) and (2.68) involve two averages; the values of $\overline{P_J^R}$ and $\overline{(P_J^R)^2}$ are obtained by first averaging over cluster configurations and then over atoms in a cluster. Here a notice should be given: In principle, the $P_j^R$ of a cluster configuration is calculated with the INM eigenvectors of $(L_1, L_2, L_3)$ based on *Method II* given in Sec. 2.2.2. However, by replacing the three INM eigenvectors with those purely rotational eigenvectors given in Eq. (2.23), a reasonable approximation of the rotational projector reads

$$\hat{P}_j^R \simeq \sum_{\eta=x,y,z}\left|\mathbf{e}_j^{R'_\eta}\right|^2 = \frac{I_{jx}}{I_x} + \frac{I_{jy}}{I_y} + \frac{I_{jz}}{I_z}, \tag{2.69}$$

in which

$$I_{j\mu} = m\left(r'^2_{j\nu} + r'^2_{j\eta}\right), \tag{2.70}$$

with $\mu \neq \nu \neq \eta$ assuming cyclic in *x*, *y*, and *z* as before. In Eq. (2.69), $\hat{P}_j^R$ has therefore been approximated as a sum of three ratios and each ratio measures the contribution of the atom *j* in the moment of inertia of a cluster's configuration with respective to one of its principal axes. By substituting this approximate $\hat{P}_j^R$ into Eqs. (2.67) and (2.68), $\overline{P_J^R}$ and $\overline{(P_J^R)^2}$ can be shown explicitly as

$$\overline{P_j^R} \simeq \frac{1}{n}\sum_{j=1}^{n}\left\langle \frac{I_{jx}}{I_x} + \frac{I_{jy}}{I_y} + \frac{I_{jz}}{I_z} \right\rangle, \tag{2.71}$$

$$\overline{\left(P_j^R\right)^2} \simeq \frac{1}{n}\sum_{j=1}^{n}\left\langle \frac{I_{jx}}{I_x} + \frac{I_{jy}}{I_y} + \frac{I_{jz}}{I_z} \right\rangle^2. \tag{2.72}$$

As the approximate $\overline{P_J^R}$ and $\overline{(P_J^R)^2}$ are applied to calculate the standard deviation $\sigma_R(T)$ in Eq. (2.66), we are led to an approximate analytic expression of the order parameter $\tau(T)$. The calculation using this analytical expression for $\tau(T)$ is certainly numerically straightforward.

It is worth mentioning, furthermore, two advantages in using the approximate $\tau(T)$: (a) Theoretically, $\tau(T)$ has been reduced to a geometric one which is more directly related to the cluster structure, and (b) the computation of $\tau(T)$ are considerably easier and simplified by the unnecessity of dealing with the Hessian matrix and subsequent diagonalization. Although the approximate $\tau(T)$ is simply related to the cluster structures, the order parameter $\tau(T)$ is nevertheless conceptually originated from the curvatures of potential energy landscape, which are more fundamental for they contain the dynamic information and determine the structural transition of a cluster.

# Chapter 3
# Point Group Theory for the Lowest Energy Structure of Clusters

In this chapter, by point group theory, I investigate the symmetric properties of clusters at the lowest energy structure (LES). In the first section, I will introduce the basic concept of point group theory. In Sec. 3.2, the $C_{3v}$ and $D_{5h}$ axial point groups, to which the $Ag_{17}Cu_2$ and $Ag_{14}$ clusters at the LES, respectively, are illustrated.

## 3.1 Basic concept of point group theory

In this section, I will introduce the definition of a group and show the multiplication structures of elements in a group by *multiplication table*. According to the multiplication structures, I classify the elements in a group into some subsets; this classification is helpful for understanding the properties of a group more concretely.

### 3.1.1 Definition of group

In group theory, we use symbols to denote the elements of group in a wider sense. They may represent a number, matrix, linear operator, or geometrical operations such as the rotation of a rigid body, and the collection of elements must possess the definite group properties:

> *Any collection of elements* $\{A, B, \cdots, R, \cdots\}$ *has the group property if an associative law of combination is valid under the specified manipulation for any sequence of element and for any ordered pair R and S, there is a unique product, written as RS, which(in some agreed sense) is equivalent to some single element T which is also in the collection.*

However, a collection which possesses this group property is not sufficient to form a group and there are some other rules that the collection should obey. I give the complete conditions for a group in a more formal definition.

> *A collection of elements form a group G, if* (a) *it possesses the group property* (b) *it contains a unit element E such that RE=R for all R in G;* (c)*it contains for every element R an inverse, which may be called* $R^{-1}$*, such that* $RR^{-1}=E$

One may doubt in condition (b) and (c) whether the right unit or right inverse elements would be the left unit or left inverse? Actually, this answer is yes. It can be proven that the right unit or inverse are also the left unit or inverse. Therefore, this property is implied naturally in condition (b) and (c), the additional statements about this are unnecessary.

### 3.1.2 Generator, subgroup, coset, class

In general, the *order* of a group is defined by its number of elements. In the point group theory, we concern mainly with groups of finite order and in this case the properties of a group of order $g$ are conveniently summarized in a multiplication table which sets out systematically the products of all $g^2$ pairs of elements. Basically, the multiplication table is the array and an example is shown in Table 3.1.

Table 3.1 The general form of the multiplication table for a group including four elements *A*, *B*, *C* and *D*

| | *A* | *B* | *C* | *D* |
|---|---|---|---|---|
| *A* | *AA* | *AB* | *AC* | *AD* |
| *B* | *BA* | *BB* | *BC* | *BD* |
| *C* | *CA* | *CB* | *CC* | *CD* |
| *D* | *DA* | *DB* | *DC* | *DD* |

By examining the multiplication table, one can notice that all the elements of a group of order g may be expressed as products among a limited number of elements called *generators*. Consider a more simple case, if $R$ is in G, $R^2, R^3, \ldots, R^n, \ldots$ are also in G, G will be of infinite order unless $R^n = E$ for some value of $n$. The set of elements $\{R^2, R^3, \cdots, R^n(=E)\}$ is called *a cyclic group* of order *n*. Here I have adopted the usual algebraic terminology and write $RR\cdots R = R^n$. The usual "laws of indices" are then valid and note that $R^0 = E$.

The definition of a group by means of its generators is an exceedingly useful devise. The generator provides a simple method for classifying the symmetry of groups, and this is particularly useful for example given in Sec. 3.2. Therefore, I give a formal definition of generator

*A set P of elements of a group G is a system of generators of the group if every element of G can be written as the product of a finite number of factors, each of which is either an element of P or the inverse of such an element.*

By the definition of a generator, each element of a group can be written as a product of (positive or negative) integer powers of the generators.

Any collection of the elements of $G$ which by themselves form a group H is called a *subgroup* of G. Actually, except two kinds of trivial subgroup (or called *improper subgroup*), the unit element only and the whole group itself, other subgroup are said to be *proper subgroups*. We should notice that the subgroups of a group do not correspond to a way to partition the group. For this point, we notice that the unit element $E$ must be a member of every subgroup.

A useful method to specifically partition a group into distinct sets of elements (no element common to two or more sets) is to introduce the idea of *coset*. Let $\mathrm{H} = \{A_1, A_2, \cdots, A_h\}$ and suppose that $R_1$, $R_2$, … are elements of G but not contained in H. Then, the collection defined by

$$R_k H = \{R_k A_1,\ R_k A_2,\ \cdots,\ R_h A_h\} \tag{3.1}$$

is called the left coset of H with respect to $R_k$. The following is some properties of cosets:

*(i) Every elements of a group appears either in the subgroup or in one of its cosets.*
*(ii) No element can be common to both a subgroup and one of its cosets.*
*(iii) No element can be common to two different cosets of the same subgroup.*
*(iv) No coset can contain the same element more than once.*

As a result of above properties of cosets, we can completely partition a group into the distinct cosets. That is, each element of group can be specifically classified into a subgroup or its cosets. It is inferred that

*The order h of any subgroup H must be a divisor of the order g of the group $G$.*

By the way, it is also possible to define the left cosets. For a finite group, it can be shown that the left cosets and right cosets give exactly the same partition of the group, though the left and right cosets with respect to one particular element are not necessarily identical.

Another way to partition the group is by using the definition of class. Before introducing that, we consider a relation in the following statement

*An element $B$ is said to be conjugate to $A$ with respect to $R$ if $B = RAR^{-1}$*

We gather elements conjugate to $A$ into a collection, as $R$ runs through the whole group G. We search

the distinct collections via changing the element $A$ one by one of group $\mathrm{G}$ and the distinct collections are called classes. We see at once that for any two elements belong to the same class, they will be conjugate to each other with respect to some element of this group.

# 3.2 Axial point group

The clusters studied in this thesis include the $Ag_{14}$ and $Ag_{17}Cu_2$ metallic clusters, whose lowest-energy structures (LES) belong to $\mathrm{C_{3v}}$ and $\mathrm{D_{5h}}$ axial point group, respectively. In general, the axial point group of a cluster structure usually can be characterized by a *n*-fold principle axis, with which the cluster rotates through $2\pi k/n$ $(k = 0, 1, \cdots, n-1)$ will return to its original structure, and whose number of fold is larger than any other axis. Customarily, this *n*-fold principal axis is chosen to be the z axis and is depicted in Fig. 3.1, in which the symbol $\mathrm{C_2}$ means any other 2-fold axis possesses the 2-fold rotational symmetry and the symbol $\sigma$ is a mirror plane that reflects points from one side to the other side and keeps original structure of a cluster. I will explain in detail later by introducing the symmetrical properties of the $\mathrm{C_{3v}}$ and $\mathrm{D_{5h}}$ axial point groups.

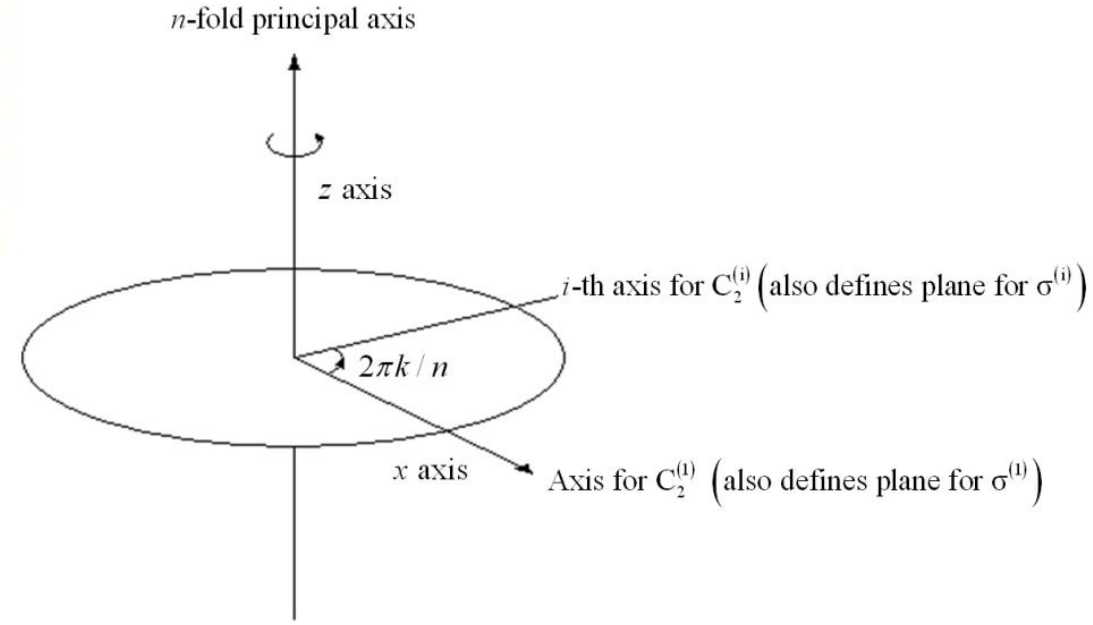


Fig. 3.1 Conventionally, If an object belongs to the axial point group of n-fold rotational symmetry, the n-fold principal axis is fixed to parallel to the z-axis. For every rotation of $2\pi k/n$ (k ∈ integer) with respect to principal axis, the object maintains the original structure. The other symbol $C_2$ represents the rotational symmetry of every rotation $\pi$ with respect to 2-fold rotational axis normal to the principal axis and, customarily, the 2-fold axis is set to be the x-axis. Another is the reflection symmetry with respect to a plane which is denoted by the symbol σ.

### 3.2.1 $C_{3v}$ axial point group

In this subsection, I illustrate the symmetric properties of $C_{3v}$ axial point group for the lowest energy structure (LES) of metallic cluster $Ag_{14}$, which is shown in Fig. 3.2. The LES consists of an icosahedron and a floating atom which is located outside it at an equal distance from three atoms that form a triangular facet of the icosahedron. The icosahedron is not perfect but a slightly deformed one. By removing away the floating atom, the deformed icosahedral geometry can be relaxed into a perfect icosahedron whose surface consists of 20 identical equilateral triangular facets with a bond-length side of 2.689 Å. By comparing the structure of this perfect icosahedron with the deformed one in $Ag_{14}$, we find that their major difference lies in the very small expansion of the triangular facet capped on top by the floating atom and the expanded triangular facet is still equilateral but now having a bond-length of 2.705 Å.

Differing from the perfect icosahedrons, which has the $I_h$ point group symmetry, the geometric structure of the LES of $Ag_{14}$ takes on the $C_{3v}$ point group with the z-axis passing through the central atom inside the icosahedron and the adatom, which are depicted in Fig. 3.2. [88] The 12 atoms at the vertices of the deformed icosahedron can be recognized as four equilateral triangles on four different planes perpendicular to z-axis shown in Fig. 3.2 (b), (c) and (d). In (d), the three atoms of each equilateral triangle have an equal distance from the floating atom. According to the $C_{3v}$ point group, atoms of the LES of $Ag_{14}$ are classified into six subsets, denoted by different colors as shown in Fig. 3.2. The central atom and the floating atom are two subsets each of single atom and are denoted hereafter as *C* and *F*, respectively. The other 12 atoms are differentiated into four subsets, with each subset containing the three atoms consisting of one equilateral triangle mentioned above. With distances from the *F* atom at 2.681, 4.579, 5.438, and 6.573 Å, the four subsets of atoms are $S_1$, $S_2$, $S_3$ and $S_4$ representing from the nearest to the farthest distance, respectively (shown in Fig. 3.2(c)). In the following, I will introduce symmetry operations of the $C_{3v}$ axial point group and it can be evidenced that the six subsets of $Ag_{14}$ are unable to mix by any of these operations.

With the LES of $Ag_{14}$ as an example, I define the three-fold rotational symmetry, which is about the z-axis depicted in Fig. 3.3(a). The $C_3$ is used to denote this rotational symmetry operation for every counterclockwise rotation $2\pi/3$ with respect to the principal axis and each power of $C_3$ keeps the rotational invariance of original structure. Apparently, there are three symmetry elements $\{C_3, \bar{C}_3(=C_3^2), \cdots, E(=C_3^3)\}$ generated by the $C_3$ generator, and they form a typical cyclic subgroup by the definition given in Sec. 3.1.2. On the other hand, another typical symmetry element is the reflection symmetry with respect to a plane, in which the points are reflected from one side of the plane to the other side and the original structure is kept invariantly (shown in Fig. 3.3(b)). By convention, the refection symmetry about a mirror plane is denoted by $\sigma$. In the LES of metallic cluster $Ag_{14}$, one can easily find three mirror planes that contain the principal axis and are vertical to the x-y plane and each plane contains one atom in each of the $S_1$, $S_2$, $S_3$ and $S_4$ subsets. Conventionally, $\sigma_v$ is used to denote this kind of mirror planes. So, the one parallel to the x-axis is assigned as $\sigma_v^{(1)}$, and the other two are

$\sigma_v^{(2)}$ and $\sigma_v^{(3)}$, with the superscript increasing as in the counterclockwise direction with respect to the principal axis. For a point group with both the symmetry operations $C_3$ with rotational symmetry about a principal axis and $\sigma_v^{(i)}$ with refection planes passing through the principal axis, this group is called the $C_{3v}$ axial point group. Thus, in the $C_{3v}$ axial point group, we use the capital "C" to denote the rotational symmetry about the principal axis and the subscript "3" means that there is a 3-fold rotational symmetry and the subscript "v" denotes the vertical reflection planes that contain the principal axis. Further, we notice that one can generate other $\sigma_v^{(i)}$ by multiplying $\sigma_v^{(1)}$ with powers of $C_3$, so that $\sigma_v^{(1)}$ can be considered as a new generator of the $C_{3v}$ axial point group. and this is the critical characteristics to distinguish from the $C_3$ point group [89] (which can be generalized to $C_{nv}$ and the $C_n$ axial point group). The detail multiplications of elements in the $C_{3v}$ axial point group are expressed in Table 3.2, in which one can easily check group properties. The subgroups, cosets, classes and generators of the $C_{3v}$ axial point group are given in Table 3.3.

Table 3.2 Multiplication table of $C_{3v}$ axial point group

| | $E$ | $C_3$ | $\bar{C}_3$ | $\sigma^{(1)}$ | $\sigma^{(2)}$ | $\sigma^{(3)}$ |
|---|---|---|---|---|---|---|
| $E$ | $E$ | $C_3$ | $\bar{C}_3$ | $\sigma^{(1)}$ | $\sigma^{(2)}$ | $\sigma^{(3)}$ |
| $C_3$ | $C_3$ | $\bar{C}_3$ | $E$ | $\sigma^{(3)}$ | $\sigma^{(1)}$ | $\sigma^{(2)}$ |
| $\bar{C}_3$ | $\bar{C}_3$ | $E$ | $C_3$ | $\sigma^{(2)}$ | $\sigma^{(3)}$ | $\sigma^{(1)}$ |
| $\sigma^{(1)}$ | $\sigma^{(1)}$ | $\sigma^{(2)}$ | $\sigma^{(3)}$ | $E$ | $C_3$ | $\bar{C}_3$ |
| $\sigma^{(2)}$ | $\sigma^{(2)}$ | $\sigma^{(3)}$ | $\sigma^{(1)}$ | $\bar{C}_3$ | $E$ | $C_3$ |
| $\sigma^{(3)}$ | $\sigma^{(3)}$ | $\sigma^{(1)}$ | $\sigma^{(2)}$ | $C_3$ | $\bar{C}_3$ | $E$ |

Table 3.3 The symmetry operators of the $C_{3v}$ axial point group are given in the 2nd and 3rd rows. The elements in the 2st row form a proper subgroup. The elements in the same block belong to a class. Generators are mark by red. Left coset is in the 3rd row.

| **$C_{3v}$ axial point group** | | |
|---|---|---|
| $E$ | $C_3$ | $\bar{C}_3$ |
| $\sigma_v^{(1)}$ | $\sigma_v^{(2)}$ | $\sigma_v^{(3)}$ |

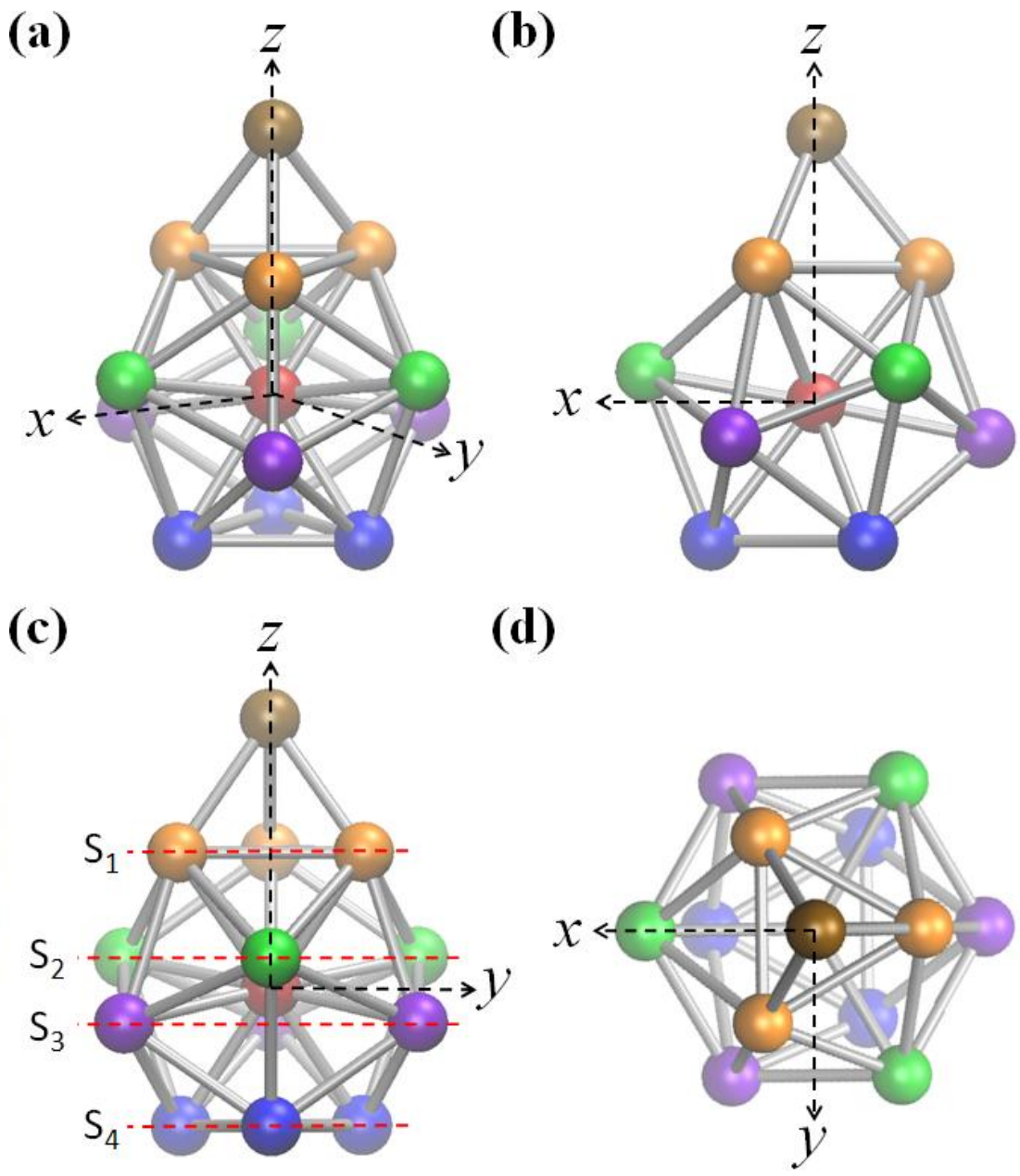


Fig. 3.2 (a) The lowest energy structure (LES) of metallic cluster $Ag_{14}$ in 3-dimensional real space. According to the $C_{3v}$ axial point group, the atoms can be classified into six subsets denoted by different colors. The origin of the coordinate systems is set at the central atom (red). The z axis passes through the central and floating (brown) atoms and the x axis, normal to the z axis, is in the plane that contains the z axis and a green atom. (b), (c) and (d) are the three projected views of the LES. In (b), the LES is projected on to the x-z plane. In (c), the LES is projected on to the y-z plane. The red broken lines indicate the four equilateral triangles that are normal to the z-axis and contain the atoms of the four subsets $S_1$, $S_2$, $S_3$ and $S_4$, which are colored with orange, green, purple and blue, respectively. In (d), the LES is projected on to the x-y plane. The three atoms of each $S_1$, $S_2$, $S_3$ and $S_4$ subsets are in a plane and indeed form an equilateral triangle.

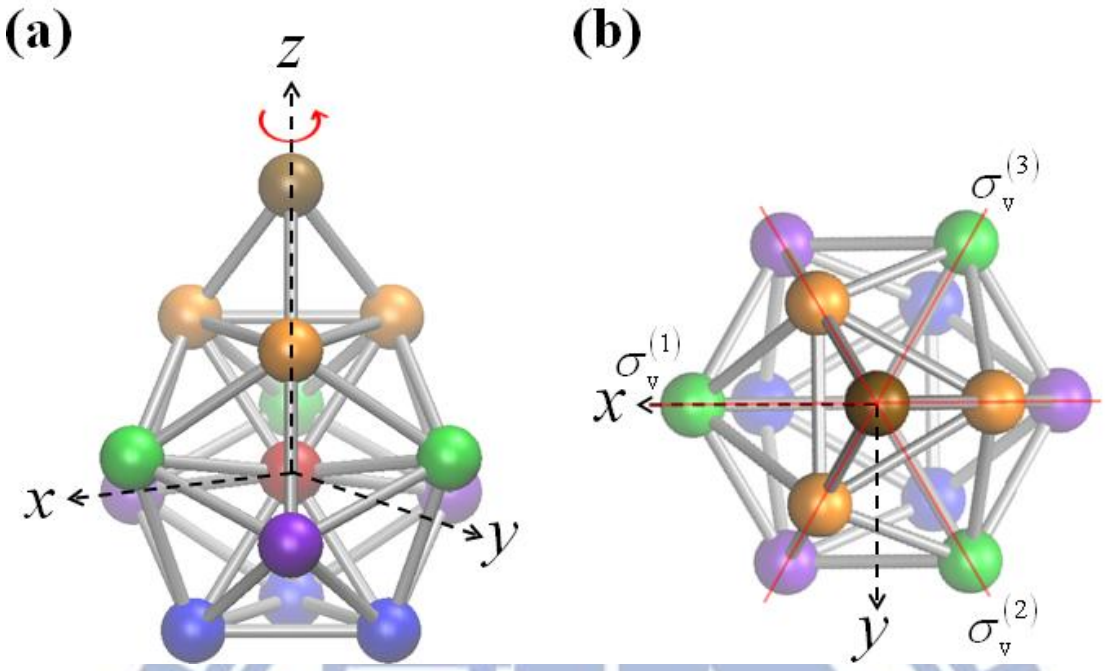


Fig. 3.3 The symmetry operations of the $C_{3v}$ axial point group for $Ag_{14}$: (a) the rotational operations $C_3, \bar{C}_3(=C_3^2), \cdots, E(=C_3^3)$ with respect to the principal axis, (b) the reflection planes denoted by $\sigma_v^{(1)}$, $\sigma_v^{(2)}$, $\sigma_v^{(3)}$.

### 3.2.2 $D_{5h}$ axial point group

Metallic cluster $Ag_{17}Cu_2$ takes on its LES characterized by two "center" Cu atoms locating inside 17 "surface" Ag atoms, with the 19 atoms forming two icosahedra with a partial overlap (see Fig. 3.4), The LES of $Ag_{17}Cu_2$ is consistent with our understanding of a bimetallic cluster (BC) that an atom of smaller size prefers to be surrounded by atoms of larger size (ionic radii of Cu and Ag are 0.96 Å and 1.26 Å, respectively). This mixing tendency arises from the size-mismatched disparity and has previously been noted in the literature for the noble-metal-based BCs [90- 92]. This subsection is concerned with a study for the LES of $Ag_{17}Cu_2$ from the point group theory. In this LES, the 19 atoms of $Ag_{17}Cu_2$ cluster are thus classified into four subsets shown in Fig. 3.4. The four subsets consist of the two centrally located Cu atoms, the top and bottom Ag atoms, the five Ag atoms occupying the middle pentagonal ring, and the ten Ag atoms sitting in the upper and lower pentagonal rings, which I denote hereafter as $Cu^{(2)}$, $Ag^{(2)}$, $Ag^{(5)}$, and $Ag^{(10)}$, respectively.

The LES of $Ag_{17}Cu_2$ belongs to the $D_{5h}$ symmetry [88] of point group (shown in Fig. 3.5(a)), which is described in the following: With the principal axis that goes along the two Cu atoms, the LES corresponds to $C_5$ symmetry operation. The axes of 2-fold rotational symmetry are the ones that are perpendicular to the principal axis and pass through one of the Ag atoms in the middle pentagonal ring, which is in the xy-plane. As shown in Fig. 3.5(b) and (c), rotating the atoms in the cluster an angle of $\pi$ with respect to one of the axes of 2-fold rotational symmetry sends the structure of the cluster into

itself. Conventionally, the 2-fold rotational symmetries are denoted as $C_2^{(i)}$ with $i$=1 to 5: $C_2^{(1)}$ is referred to the one with the x-axis as the rotational axis and the others are indicated with superscript (i) increasing in the counterclockwise direction with respect to the principal axis. Totally, there are five two-fold rotational symmetric operators, which can be generated by multiplying $C_2^{(1)}$ with each of the five operators $C_5, C_5^2, \bar{C}_5^2 (= C_5^3), \bar{C}_5 (= C_5^4), E (= C_5^5)$, so that the $C_2^{(1)}$ can be referred as a new generator of $D_{5h}$ axial point group.

Further, we should consider the reflection symmetry. As shown in Fig. 3.5(b), there are five mirror planes, with each plane containing the principal axis and one 2-fold rotational axis of the $C_2^{(i)}$ operation. We use $\sigma_v^{(i)}$, with $i$=1 to 5, to denote the five reflection symmetries with respect to each one of the five mirror planes. Indicated in Fig. 3.5(c), the other reflection plane is the horizontal plane containing the middle pentagonal ring. With respect to this refection place, the atoms above and below it reflect to each other such that the cluster structure maintains and we denote this symmetry operation as $\sigma_h$. One can notice that $\sigma_h$ is another generator, which generates the five $\sigma_v^{(i)}$ by the multiplication of $\sigma_h C_2^{(i)}$. On the other hands, due to the existence of $C_2$ axis, we should additionally consider *dihedral plane* which contains the principal axis and bisects the angle between any adjacent pair of red lines in Fig. 3.5(b). However, in $D_{5h}$ axial point group, no reflection symmetry would correspond to the dihedral plane. In convention, the capital "D" is used to denote the axial point group that possesses the $C_2$ rotational symmetry. Moreover, in the subscript of "$D_{5h}$", the "5" denotes the five-fold rotational symmetry and the "h" means the reflection symmetry about the horizontal plane.

Finally, I introduce a non-intuitive symmetry operation $S_5$, which is defined by a two-step symmetry operation with $C_5$ is operating first and $\sigma_h$ following, such that this newly defined operator is expressed as $S_5 = \sigma_h C_5$. According to the definition of a group given in Sec. 3.1.1, the product of any two elements of a group is still an element of this group; however, this two-step operation is not included in the afore-mentioned symmetry operations, thus it's nessasary to include the symmetry operation $S_5$ and its inverse $\bar{S}_5$ into the $D_{5h}$ axial point group.

Table 3.4 The symmetry operators of the $D_{5h}$ axial point group. The elements in the 2nd row form a proper subgroup. The elements in the same block belong to a class. Generators are mark by red. Left cosets are in the 3rd, 4th and 5th rows. The elements in the lower block with bold lines are generated by multiplying $\sigma_h$ with elements in the upper block with bold lines. The operator $S_5$ is defined by $\sigma_h C_5$ and $\bar{S}_5$ is its inverse.

| **$D_{5h}$ axial point group** | | | | |
|---|---|---|---|---|
| $E$ | $C_5$ | $\bar{C}_5$ | $C_5^2$ | $\bar{C}_5^2$ |
| $C_2^{(1)}$ | $C_2^{(3)}$ | $C_2^{(4)}$ | $C_2^{(5)}$ | $C_2^{(2)}$ |
| $\sigma_h$ | $S_5$ | $\bar{S}_5$ | $S_5^3$ | $\bar{S}_5^3$ |
| $\sigma_v^{(1)}$ | $\sigma_v^{(3)}$ | $\sigma_v^{(4)}$ | $\sigma_v^{(5)}$ | $\sigma_v^{(2)}$ |

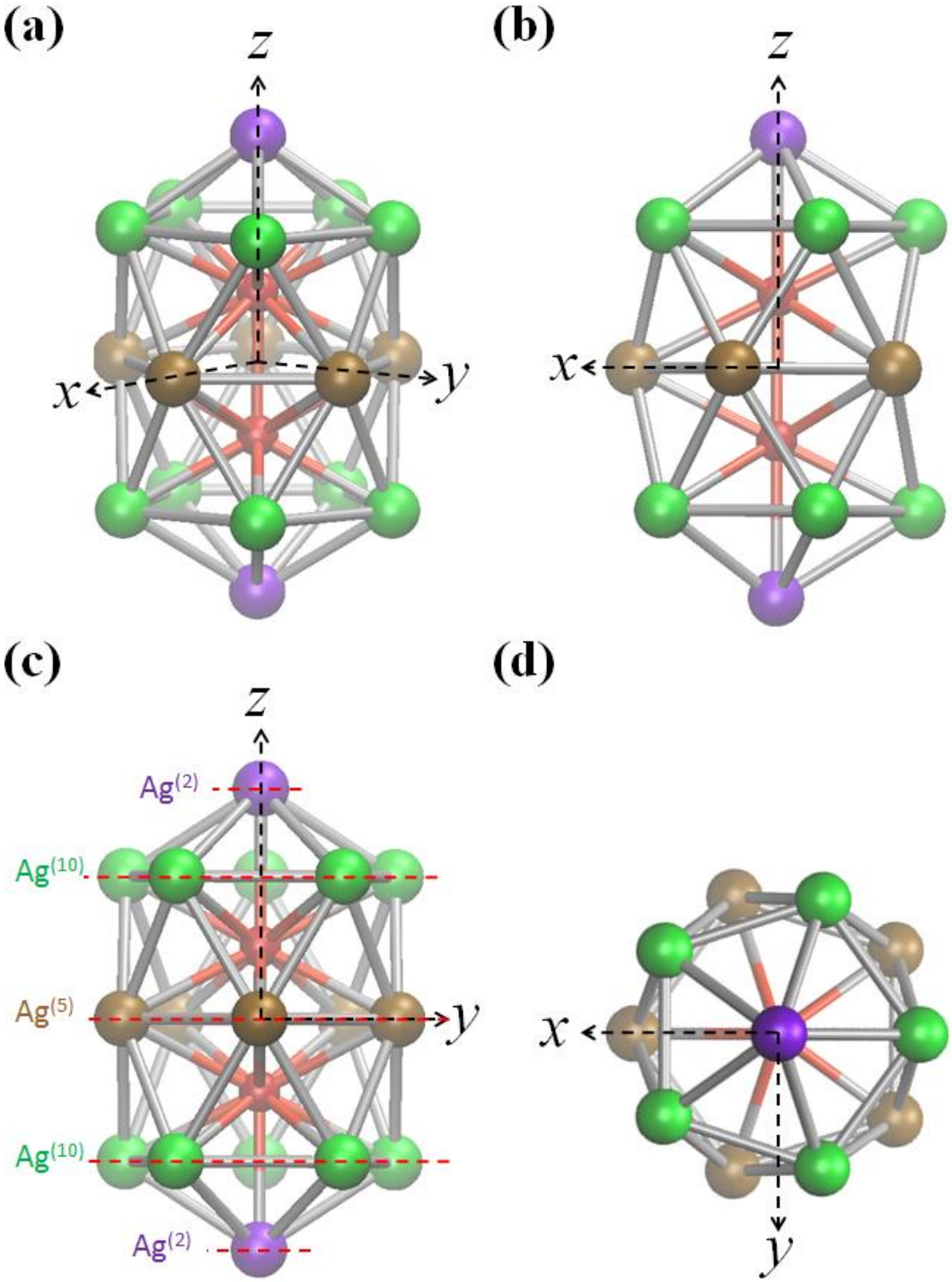


Fig. 3.4 (a) The LES of $Ag_{17}Cu_2$ cluster in three-dimensional space. According to the $D_{5h}$ axial point group, the atoms can be classified into four subsets distinguished by different colors. There are two Cu atoms, colored in red, inside the cluster. With the origin of the coordinate system at the center of the two Cu atoms, the z-axis passes through the two Cu atoms and the x-axis is normal to the z-axis and passes through one Ag atom in the middle pentagonal ring, which is in the xy-plane. In (b), (c) and (d), the LES is projected on to the x-z, y-z and x-y planes, respectively. In (c), the red broken lines indicate the three subsets of Ag atoms.

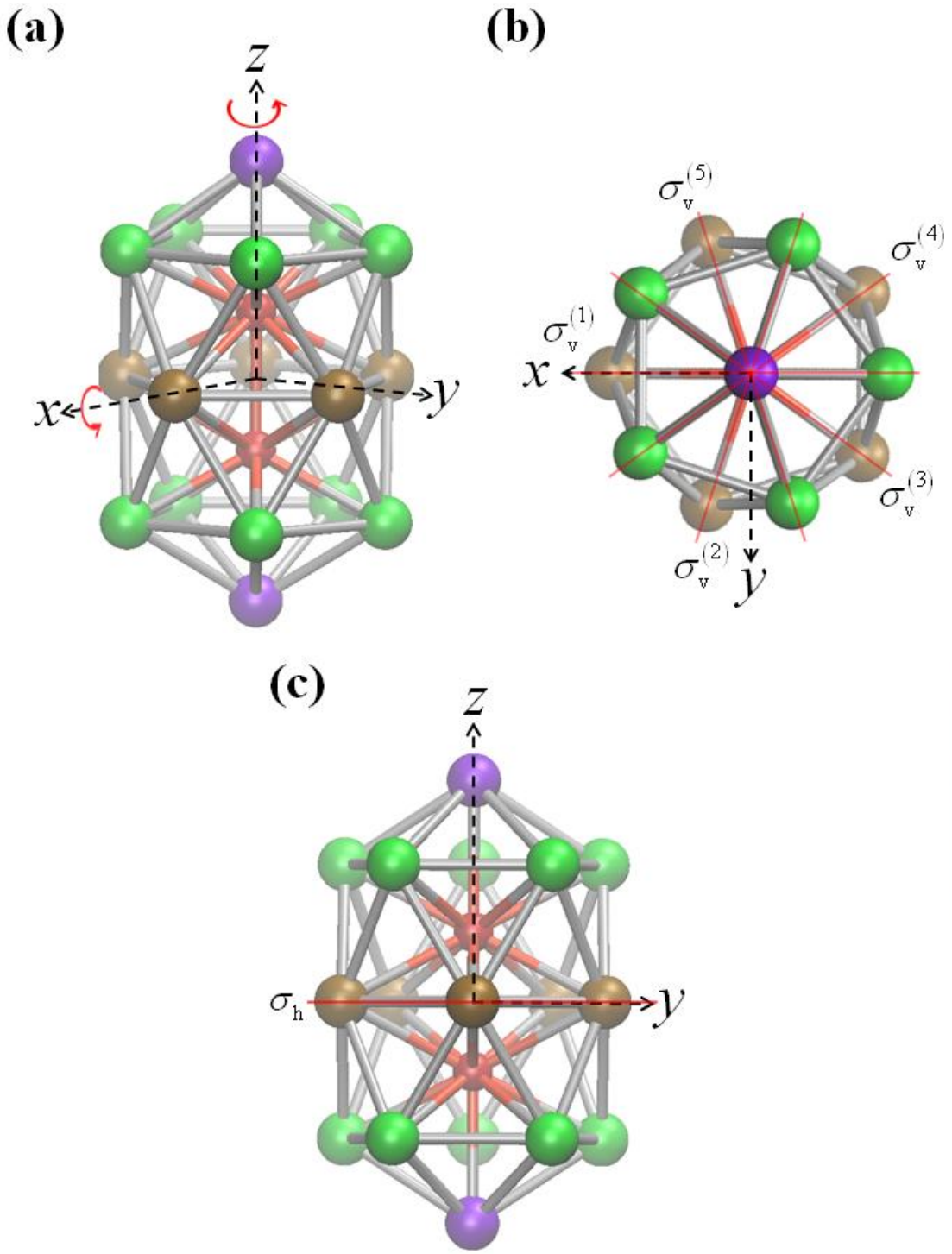


Fig. 3.5 The $D_{5h}$ axial point group of $Ag_{17}Cu_2$. In (a) the two red arrows indicate the $C_5$ and $C_2$ symmetries with respect to the z- and x-axis, respectively. In (b), the red solid line indicates the reflection plane, denoted as $\sigma_h$, normal to the principal axis. In (c), the red solid lines indicate the five reflection planes, denoted as $\sigma_v^{(i)}$ with *i*=1 to 5, with each one containing the principal axis and one of the 2-fold rotational axes.

# Chapter 4 Simulation, Model and Specific Heat

## 4.1 Isothermal Brownian-type molecular dynamics

In this thesis, the isothermal Brownian-type MD simulation is used to generate the cluster configurations of at different temperatures. I give a brief description of the isothermal Brownian-type MD simulation since considerable technical details have been given in Refs. [45, 46, 58]. In Lai *et al*. works, they employed the modified cubic coupling scheme which was originally developed for studying the thermal properties of pure metallic clusters [58] and subsequently generalized to alloy clusters [45, 46]. Let us consider a bimetallic cluster $A_{n_a}B_{n_b}$, where $n_a$ ($n_b$) is the number of atoms of *a*-type (*b*-type). The equations of motion, which describe its *x*-component at a temperature *T*, can be written as

$$\dot{x}_{ia} = \frac{p_{i_a,x}}{m_a} \tag{4.1}$$

$$\dot{p}_{i_a,x} = -\frac{\partial E_n}{\partial x_{i_a}} - \frac{\alpha_a e_{0,a}}{nL_0}\mu_{a.x}^3 \frac{p_{i_a,x}}{\tilde{p}_{0,a}} - \frac{\beta_a e_{0,a}}{nL_0} v_{a,x}\left(\frac{p_{i_a,x}^2}{\tilde{p}_{0,a}^2} - d_0\right) - \frac{\vartheta e_{0,a}}{nL_0}\eta_{a,x}\frac{p_{i_a,x}^3}{\tilde{p}_{0,a}^3}, \tag{4.2}$$

in which $x_{i_a}$ and $p_{i_a,x}$ are the *x*-component position coordinate and momentum, respectively, and the subscript $i_a$ refers to the *i*-th atom of type *a*. The $\mu_{a,x}$, $v_{a,x}$ and $\eta_{a,x}$ variables are the *x*-component pseudo-friction coefficients of *a*-type atom and they are introduced to simulate the heat bath degrees of freedom. The entities $L_0$ and $e_{0,a}$ are constant parameters and $\alpha_a$, $\beta_a$, $\vartheta_a$, and $\tilde{p}_{0,a}$ are all functions of *T*. For b-type atoms, we simply replace the subscript *a* by *b* in Eqs. (4.1) and (4.2). The same set of equations hold for the *y* and *z* components. The explicit expressions of all of these quantities and the detailed numerical procedure to be effected are well described in Refs. [45, 46, 58] to which the interested readers are referred. The lowest energy structure of the cluster is searched by a technique described in Refs. [81] and [90], in which an optimization algorithm are developed to predict structures of pure metallic and nonmetallic clusters via combining two state-of-the-art methods, the

genetic algorithm and the basin hopping approach. Beginning at the LES, the cluster at a finite temperature can be prepared by the MD run, in which the cluster temperature is raised gradually from zero [58, 79]. In all of these simulations, atoms at a finite temperature are traced by their labels which are tagged at their LES.

For clusters $Ag_{17}Cu_2$ and $Ag_{14}$, at every increment 10K, I analyzed total $10^6$ configurations generated by the simulation within an interval of $10^{-8}$s to investigate the melting phenomenon of the cluster,

# 4.2 Empirical n-body Gupta potential

## 4.2.1 Gupta potential for $Ag_{17}Cu_2$

Intrinsically, the interactions between atoms in a cluster are many-body in nature. The inextricable complexity of Coulomb interactions between valence electrons and ions renders a first-principles derivation of a many-particle potential energy function a formidable task. Here, we employ the *n*-body Gupta potential function [93], which is widely accepted in the literature as a substitution. The empirical potentials for $Ag_{17}Cu_2$ can be written as

$$E_n = \sum_{i=1}^{n} \left\{ V_r(i) - \left[ V_a(i) \right]^{1/2} \right\} \tag{4.3}$$

where *n* is the number of particles in the cluster, the repulsive term $V_r$ is

$$V_r(r_{ij}) = \sum_{j=1(j\neq i)}^{n} A_{ij} \exp\left[ -p_{ij} \left( \frac{r_{ij}}{r_{ij}^{(0)}} - 1 \right) \right] \tag{4.4}$$

and the attractive term $V_a$, due to the hybridization of valence electrons, is

$$V_a(r_{ij}) = \sum_{j=1(j\neq i)}^{n} \xi_{ij} \exp\left[ -2q_{ij} \left( \frac{r_{ij}}{r_{ij}^{(0)}} - 1 \right) \right] \tag{4.5}$$

The parameters $A_{ij}$, $\xi_{ij}$, $p_{ij}$, $q_{ij}$, , and $r_{ij}^{(0)}$ for the Ag–Cu are obtained from the work of Mottet *et al*. [94] and are given in Table 4.1. I give the derivation of Hessian matrix of Gupta potential in Appendix A.3

Table 4.1 Gupta-type potential parameters for the bimetallic clusters Ag-Cu taken from Mottet *et al*. (Ref. [94]). The $r_{ij}^{(0)}$ for Ag-Cu is calculated by averaging the $r_{ij}^{(0)}$ of Ag-Ag and Cu-Cu.

| $ij$ | $A_{ij}$(eV) | $\xi_{ij}$ | $p_{ij}$ | $q_{ij}$ | $r_{ij}^{(0)}$(Å) |
|---|---|---|---|---|---|
| Cu-Cu | 0.0894 | 1.2799 | 10.55 | 2.43 | 2.56 |
| Ag-Cu | 0.0977 | 1.2275 | 10.7 | 2.805 | 2.725 |
| Ag-Ag | 0.1031 | 1.1895 | 10.85 | 3.180 | 2.89 |

### 4.2.2 Gupta potential for $Ag_{14}$

For metallic cluster $Ag_{14}$, as described in Yen *et al*. works for Ag-based cluster [81], they employed the empirical *n*-body Gupta potential [93] which reads

$$E_n = \sum_{i=1}^{n} \left\{ V_r(i) - \left[ V_a(i) \right]^{1/2} \right\} \tag{4.6}$$

where $n$ is the number of particles in the cluster. Since atoms in the cluster $Ag_{14}$ are of the same species, the repulsive term $V_r$ and the attractive term $V_a$ in Eq. (4.6) are, respectively, reduced to

$$V_r(i) = \sum_{j=1(j\neq i)}^{n} A \exp\left[ -p\left( \frac{r_{ij}}{r^{(0)}} - 1 \right) \right], \tag{4.7}$$

and

$$V_a(i) = \sum_{j=1(j\neq i)}^{n} \xi \exp\left[ -2q\left( \frac{r_{ij}}{r^{(0)}} - 1 \right) \right], \tag{4.8}$$

where the parameters $A$, $p$, $q$ and $r^{(0)}$ have been determined by fitting to measured bulk values. For the metal Ag, these parameters are taken from Rapallo *et al.* [92] and they are given in the 4th row of Table 4.1.

## 4.3 Calculation of specific heat

For the thermal property, the specific heat $C_V$ is considered to determine the melting temperature, The computation of this quantity is straightforward since the configuration energies were readily recorded by Eq. (4.3). In statistical mechanics, one can define the specific heat as [45, 58]

$$C_V = \frac{\left\langle E_{total}^2 \right\rangle - \left\langle E_{total} \right\rangle^2}{k_B T^2} \tag{4.9}$$

where $E_{total}$ is the total kinetic energy plus the potential energy $E_n$ given in Eq.(4.3) or (4.6) by taking a time average (see Eq. (10) in Ref. [58]). To determine the melting temperature of a cluster, we begin at $T$ = 0 K and heat it up to high temperatures. The temporal variations of the position coordinates of all atoms in the cluster at different $T$ are then recorded. Rather long elapsed times in the range of $(1 - 3) \times 10^{-7}$s were performed so that the calculated $C_V$ vs. $T$ curve develops as smooth as possible.

## 4.4 Root-mean-square bond length fluctuation constant

So far, a popular order parameter for cluster is the root-mean-square (RMS) relative bond length fluctuation $\delta$, which reflects details of the geometric property of a cluster, is defined by

$$\delta = \frac{1}{n(n-1)} \sum_{i=1}^{n} \sum_{j \neq i}^{n} \frac{\sqrt{\langle r_{ij}^2 \rangle - \langle r_{ij} \rangle^2}}{\langle r_{ij} \rangle} \tag{4.10}$$

where $r_{ij}$ is the bond length of atom *i* and *j* and *n* is the number of atom in the cluster. Due to the $\delta$ related to the geometric change, it is also known as the Lindemann-like parameter. The occurrence of an abrupt change of $\delta$ around some temperature range means that the structure of cluster changes drastically [58].

# Chapter 5
# INM Analysis for Melting Behavior of $Ag_{17}Cu_2$ Bimetallic Cluster

## 5.1 Introduction

This chapter is concerned with an INM study for the dynamics and melting behavior of $Ag_{17}Cu_2$ bimetallic cluster (BC). My motivation comes from a recent work of Yen *et al*. [81] who reported simulation results on 14-atom Ag-based BCs. In their work, they applied the isothermal Brownian-type molecular dynamic (MD) simulations to the Ag-based BCs and calculated the velocity autocorrelation function (VAF) and its Fourier-transformed power spectral density $\Omega^{(i)}(\omega)$, where the superscript *i* is referred to the *i*-th atom in the cluster. Starting from their lowest energy states, the BCs are heated up to high temperatures. The melting behaviors of the BCs are therefore studied with their specific heat data and $\Omega^{(i)}(\omega)$.

Similarly, starting from the lowest energy state, which has been shown in Fig. 3.4, the $Ag_{17}Cu_2$ BC is also heated up to high temperatures. The specific heat $C_V$ data of $Ag_{17}Cu_2$ is, thus, obtained and shown in Fig. 5.1. In this figure with a single peak, the main maximum position of $C_V$, which we define to be the cluster's melting temperature, is located at $T_m$ ≈890 K. However, the temperature variation in the $C_V$ curve of $Ag_{17}Cu_2$ is not consistent with its relative root-mean-square bond length fluctuation constant δ, which has a drastic change at in a low-temperature range (see Fig. 5.2). In this chapter, in addition to applying the same MD technique (mentioned in Sec. 4.1) to $Ag_{17}Cu_2$ to obtain VAF and $\Omega^{(i)}(\omega)$, I further analyze the simulation data in terms of the INM analysis, by evaluating the order parameter given in Sec. 2.3 from low to high temperatures and comparing the results with the specific-heat data of $Ag_{17}Cu_2$.

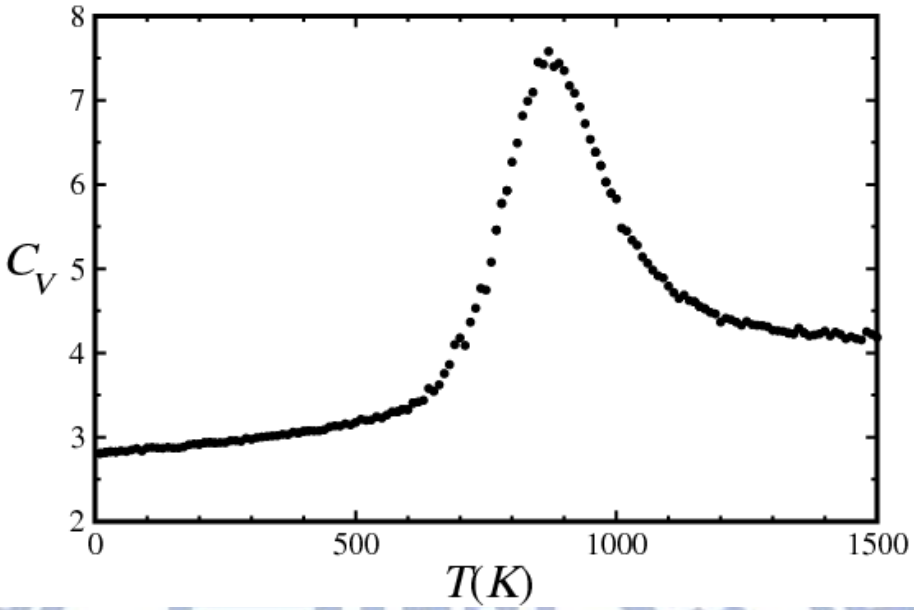


Fig. 5.1 Specific heat $C_V$ of $Ag_{17}Cu_2$ (closed circle) calculated using the isothermal Brownian-type MD simulation [79].

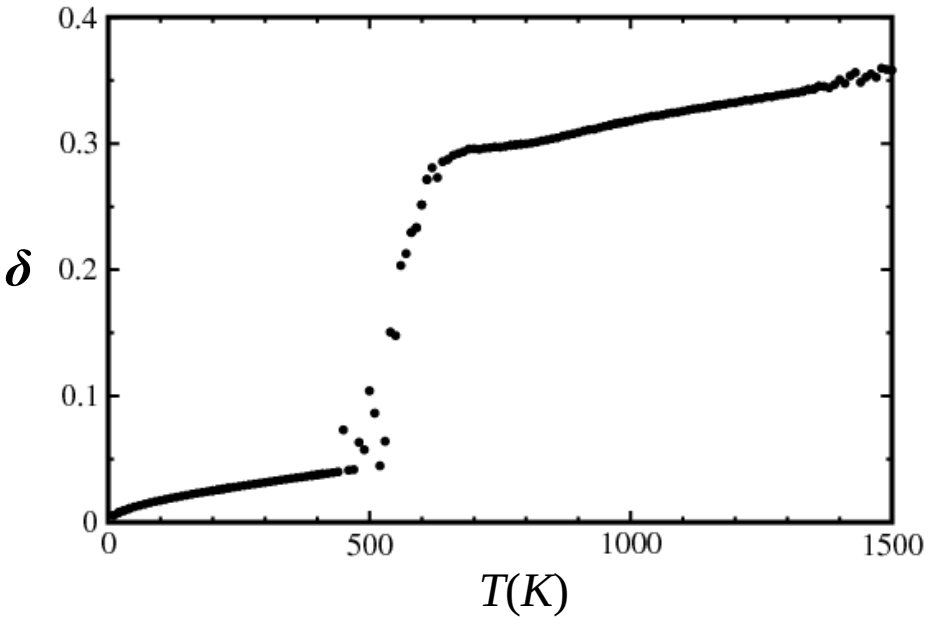


Fig. 5.2 The variation of the root-mean-square bond length fluctuation constant δ with temperature for Ag atoms in $Ag_{17}Cu_2$ [95].

## 5.2 Temperature variation of the INM spectra

In this section, I show the results of INM spectra of $Ag_{17}Cu_2$, including the vibrational DOS, projected vibrational DOS and their temperature variations, from which the melting behavior of the cluster is revealed. The INM DOS are obtained by averaging over $10^6$ configurations generated by the Brownian-type MD simulations with a time step of $10^{-15}$s within a total interval of $10^{-8}$s. At such a long time scale, the calculated velocity autocorrelation function (VAF) $C(t)$ and all $C_i(t)$ even at $T$ = 100 K have vanished already. Consequently, a reliable power spectra can be obtained via Fourier-cosine transformation for the VAFs by integrating to a finite long time tail.

### 5.2.1 Vibational DOS

The normalized INM spectra of $Ag_{17}Cu_2$ with and without the rotational modes defined in Eq. (2.29) are shown in Fig. 5.3. In general, we find no noticeable difference at low $T$ for the vibrational spectra obtained by the two methods described in Sec. 2.2.2 to remove the rotational INMs. Slight difference is observed, however, at low frequencies at high $T$. In order to measure the coupling strength between the rotational and vibrational motions, I calculate the projection $J(L_k)$ of the INM eigenvectors derived from $(L_1,L_2,L_3)$ onto the subspace spanned by the three purely rotational eigenvectors. The results are presented in Fig. 5.4, which shows how the overlap of the subspaces spanned by the two sets of rotational eigenvectors varies with temperature. Undoubtedly, the two subspaces completely overlap at zero temperature and still overlap to a large extent at low temperatures. Among the three INMs of $(L_1,L_2,L_3)$, the $L_1$ and $L_3$ modes have the largest and least values of $J(L_k)$ at all temperatures, respectively. The overlap of the two subspaces is significantly reduced at high temperatures: At $T$ = 1500 K, $J(L_1)$ roughly lowers to 63% and $J(L_3)$ to 40%, implying a stronger coupling for the rotation-vibration at high temperatures. Based on this observation, we confine our discussion in the following to only the vibrational INM spectra calculated by *Method II*. However, for $I_j$ and $\tau(T)$ defined in Eq. (2.41) and Eq. (2.62), which require the INM eigenvectors, I will touch on these quantities appealing to *Method I* or/and *Method II* for the purpose of comparison.

At $T$=100 K, the vibrational spectra show structural characteristics that all vibrational modes possess real frequencies, displaying indeed a solid-like picture, one would expect the configurations of the cluster to be around the lowest energy state of the potential energy landscape. Up to 600 K, the INM spectra are generally smoothed out. Here we observe some vibrational modes with imaginary frequencies. This suggests a transition process in which the cluster at higher temperatures possesses enough kinetic energy to stray sufficiently far from the lowest energy state that enhances its chance to crossover the energy barriers to the first and higher lowest minima. As temperature is increased further to 1100 K, one noticeable feature is that the INM spectra display a large portion of imaginary-frequency vibrational INM and this structural trait is consistent with a liquid-like behavior, in which the cluster at sufficiently high temperatures would go around everywhere the potential energy landscape.

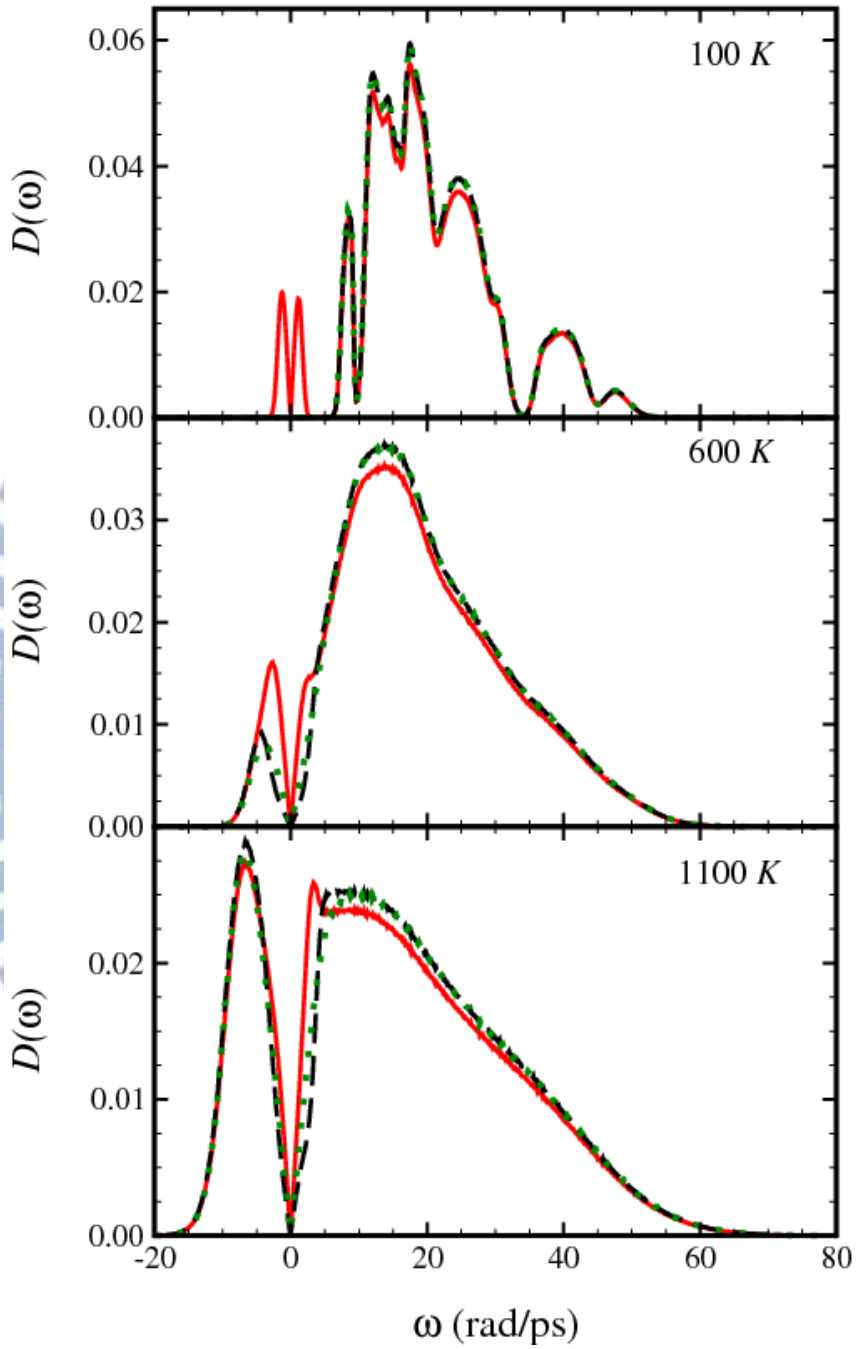


Fig. 5.3 Normalized INM spectra $D_{vib}(\omega)$ of $Ag_{17}Cu_2$ at 100, 600, and 1100K. The red-solid lines are the spectra showing the contributions of rotations and vibrations. The black-dashed and green-dotted lines are the spectra obtained by removing the rotational contribution following *Method I* and *II* introduced in Sec. 2.2.2, respectively.

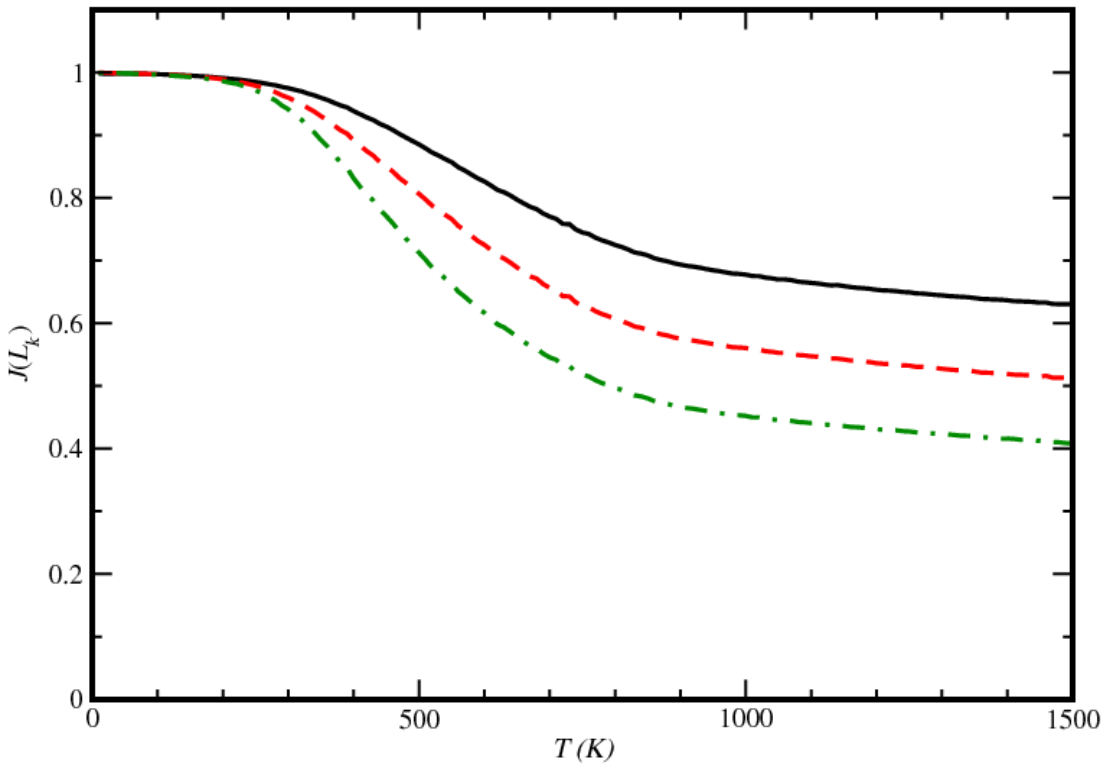


Fig. 5.4 Temperature variation of $J(L_k)$ for measuring the projection of the INM with $L_k$ onto the subspace spanned by the three purely rotational eigenvectors for $Ag_{17}Cu_2$. The black-solid, red-dashed, and green-dotted-dashed lines are for the INMs of $L_1$, $L_2$, and $L_3$, respectively.

### 5.2.2 Projected vibrational DOS

To understand the INM spectra of individual atoms in the cluster at low temperature, it is instructive to examine the vibrational-mode DOS $D_{vib}^{(LES)}(\omega)$ of $Ag_{17}Cu_2$ defined in Eq. (2.43) with the translational and rotational modes excluded. As shown in Fig. 5.5, the vibrational-mode DOS uncovers the degeneracy of each vibrational frequency. By considering the symmetry properties of the LES, which belongs to the $D_{5h}$ point group [88] as pointed out in Chapter 3, the vibrational frequencies of $Ag_{17}Cu_2$ in the LES are either non-degenerate or doubly degenerate and this lowest energy geometry is thus classified into four subsets (see Fig. 3.4). In this classification, $D_j^{(LES)}(\omega)$ of atoms in the same subset is thus the same.

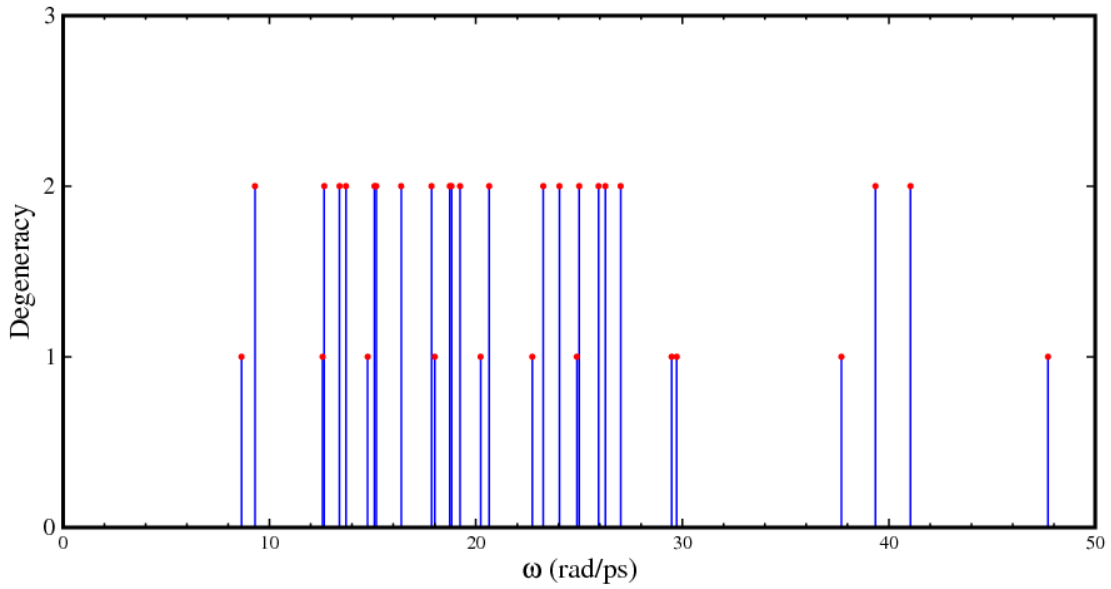


Fig. 5.5 The vibrational instantaneous normal mode frequencies of $Ag_{17}Cu_2$ in the lowest energy structure. The frequencies are either non-degenerate or doubly degenerate

In the same manner, the atoms in the $Ag_{17}Cu_2$ cluster at finite temperatures can be classified into four subsets according to the following procedure: A chosen number of atoms at a finite temperature can be obtained from those at the lowest energy state by tracing the atom labels in the simulation at a temperature that is raised gradually from zero. After this simulation process for raising temperature, I identify the atoms by their original subsets at zero temperature. At low temperatures, one can sensibly recognize the four subsets of atoms by the structures of the cluster, since the relative positions of atoms are roughly the same as those at zero temperature. Thus, the classification of atoms into the four subsets generally reflects the structures of the cluster at low temperatures. However, this is not so at high temperatures where the cluster is more appropriately realized by the liquid-like picture with its atoms of the same mass becoming completely random so that the subsets of atoms of $Ag^{(2)}$, $Ag^{(5)}$, and $Ag^{(10)}$ lose

the identities they had at zero temperature. As a result, atoms at high temperatures are only distinguishable by their masses.

Owing to the same response of atoms in a subset, we make an average of $D_j(\omega)$ for atoms in the same subset, i.e.,

$$D_X(\omega) = \frac{1}{n_X}\sum_{j=1}^{n_X} D_j(\omega) \tag{5.1}$$

with the subscript $X$ = $Cu^{(2)}$, $Ag^{(2)}$, $Ag^{(5)}$, and $Ag^{(10)}$ and $j$ runs for the total number of $n_X$ atoms in subset $X$. The $D_X(\omega)$ is, therefore, considered as the averaged contribution of one atom in subset $X$ to all vibrational INM with frequency $\omega$. In Fig. 5.6, The $D_X(\omega)$ at $T = 100$K for the four subsets of atoms of the $Ag_{17}Cu_2$ cluster are presented and, in the same figure, the $D_X^{(LES)}(\omega)$ at the LES is also presented for comparison. It can be seen that $D_X^{(LES)}(\omega)$ is a bundle of thin straight lines. Considering $D_X^{(LES)}(\omega)$ in Fig. 5.6 (a), its vibrational modes above ω=37 rad/ps are dominated by Cu atoms whose four $D_X^{(LES)}(\omega)$ have the highest values. This is in contrast to the modes dominated by Ag atoms (in Fig. 5.6 (b)–(d)) with ω less than 30 rad/ps where $D_X^{(LES)}(\omega)$ are dominant. A comparison between $D_X(\omega)$ at T=100K and $D_X^{(LES)}(\omega)$ of each subset of atoms indicates a general feature of the temperature effects for transposing the vibrational spectrum from thin straight lines into a continuous function. Indeed, due to the thermal effects, the vibrational frequency gap at T=100K between ω=30 and 37 rad/ps in $D_X^{(LES)}(\omega)$ is gradually filled up as in the $D_X(\omega)$, but there is an exception at ω=35 rad/ps where all $D_X(\omega)$ are identically zero.

The temperature variations for the vibrational INM spectra of individual atoms are shown in Fig. 5.7. We note first of all that the spectra of the two Cu atoms are indiscernible on the scales used in Fig. 5.7 for all temperatures, with a general behavior which may be summarized as follows: At $T$ =100 K, we observe three main peaks located at $\omega$ ≈23, 40, and 48 rad/ps and a lower one at $\omega$ ≈12 rad/ps. The peaks at the highest and lowest frequencies are smeared out to become shoulders at $T$ =200 K and the latter completely disappear at $T$ =300 K. For the 17 Ag atoms, their spectra at $T$ =100 K spread mainly the frequency range from $\omega$ =5 to 35 rad/ps, with a separated minor structure appearing around 40 rad/ps, and they are in fact structurally discernible; these characteristic structures, however, get smudged as the temperature increases and gradually become blurred among atoms at much higher temperatures. One general feature that can be gleaned from Fig. 5.7 is that the imaginary-frequency INM DOS for both Cu and Ag atoms emerge at $T$ ≈300 K, become noticeable at $T$ ≈600 K for Cu atoms and 400 K for Ag atoms, and thereafter grow into a significant portion at much higher temperatures.

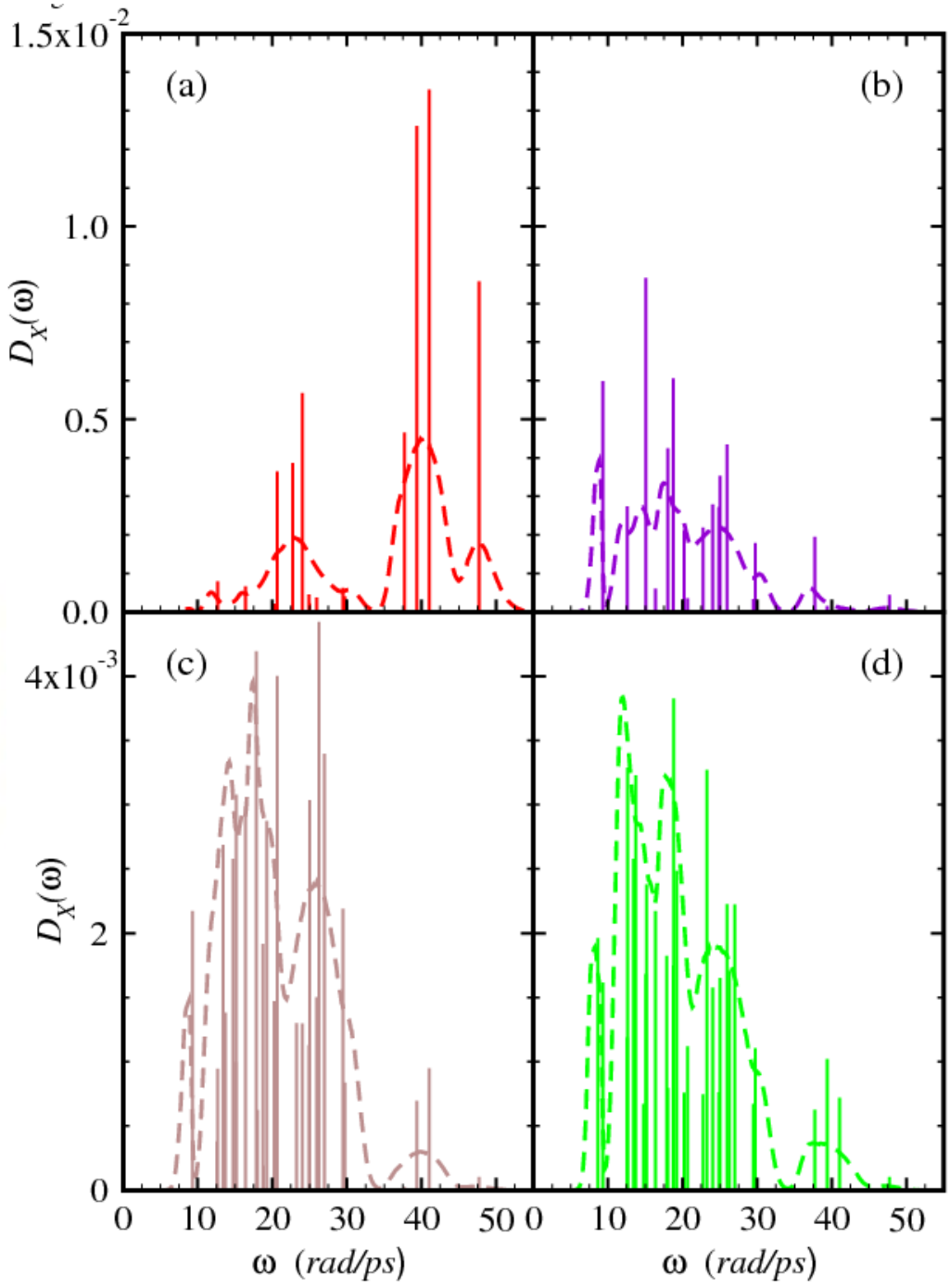


Fig. 5.6 Vibrational DOS $D_X(\omega)$ of subsets $X$ of $Ag_{17}Cu_2$, with (a) $X$ =$Cu^{(2)}$, (b) $X$ =$Ag^{(2)}$, (c) $X$ =$Ag^{(5)}$, and (d) $X$ =$Ag^{(10)}$. The thin straight lines and dashed curves refer to the $Ag_{17}Cu_2$ cluster in the LES and at T=100K, respectively.

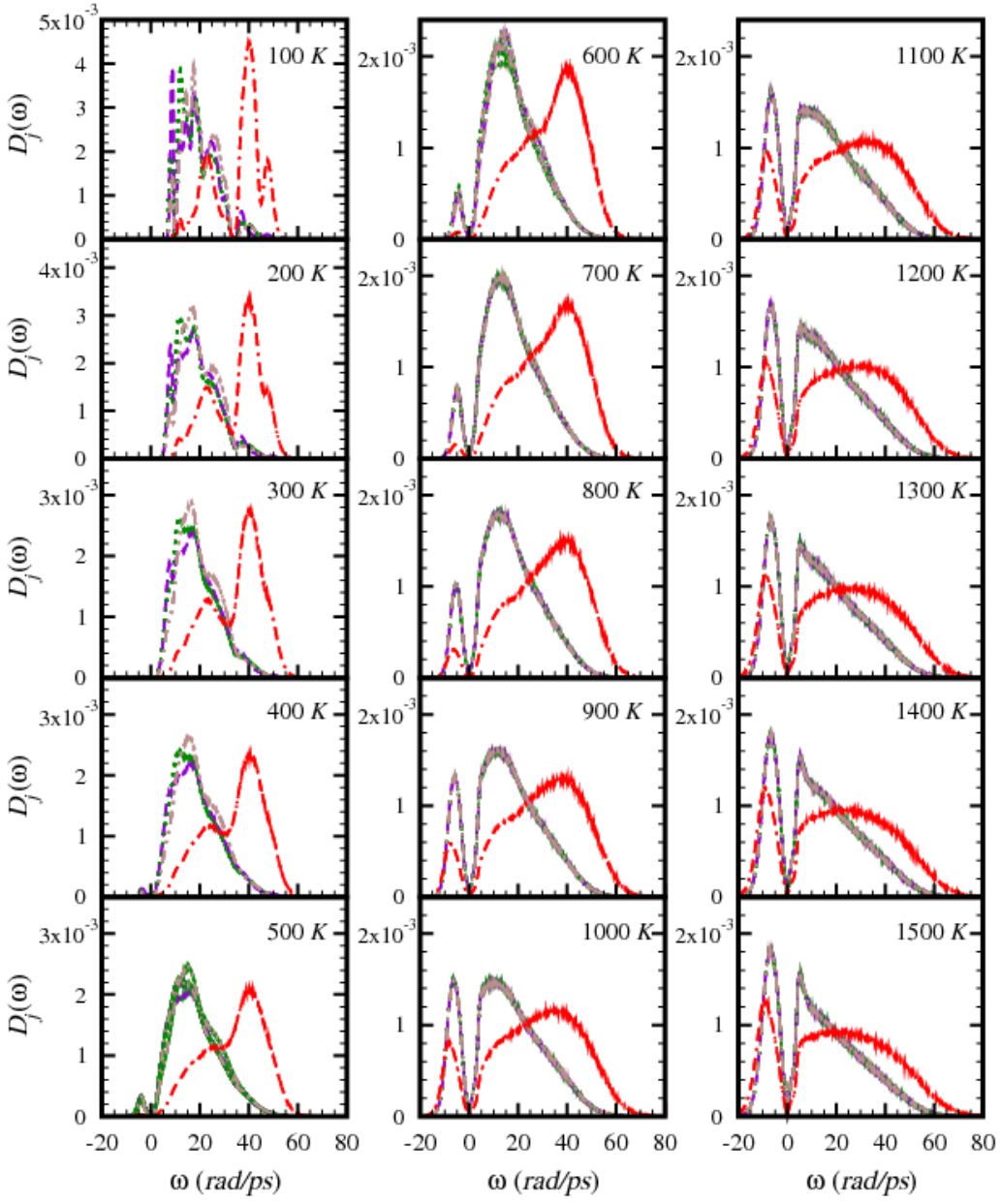


Fig. 5.7 Temperature variation of the vibrational INM spectra $D_j(\omega)$ of atoms in $Ag_{17}Cu_2$ from 100 to 1500 K. The spectra are obtained by the *Method II* described in Sec. 2.2.2. The dashed lines (orange) are for Cu atoms and the full lines (green) are for Ag atoms.

### 5.2.3 Power spectrum of velocity autocorrelation function

Obtained via the isothermal Brownian-type molecular dynamic (MD) simulations, the temperature variations of the VAF and its power spectral density of an individual Ag atom in $Ag_{17}Cu_2$ are displayed with the red lines in Fig. 5.8 and those for a Cu atom are displayed in Fig. 5.9. The comparison between $C_i(t)$ and its time Fourier transformed, $\Omega^{(i)}(\omega)$, of individual atoms obtained by the INM theory and the simulation results are also presented in Fig. 5.8 and Fig. 5.9 for the Ag and Cu atoms, respectively. We have calculated $C_i(t)$ with the INM DOS using Eq. (2.58) and in the stable-INM approximation by Eq. (2.59). At $T$ = 100 K, without any imaginary-frequency INM, the results of the INM theory and the stable-INM approximation are the same and the calculated $C_i(t)$ of both Ag and Cu atoms are rather close to those obtained by simulations (see Fig. 5.8 and Fig. 5.9). For the power spectra $\Omega^{(i)}(\omega)$, the locations of the peaks of the two kinds of atoms predicted by the INM theory generally coincide with those of the simulation results but they are much broader in width. At $T$= 500 K, because of the imaginary frequency INMs, the $C_i(t)$ calculated by the INM theory deviates somewhat from the simulated results after 0.1 ps; the deviation is stronger for the Ag atom (Fig. 5.8) than that for the Cu atom (Fig. 5.9), due to more imaginary-frequency INM in the $D_j(\omega)$ of Ag atoms. At this temperature, the spike-like structures in the simulated $\Omega^{(i)}(\omega)$ are seen to be cut away in the INM theory. At $T$ = 900 and 1500 K, the $C_i(t)$ calculated by the INM theory yields accurately the simulation results roughly within 80 fs, which is the same time scale for the cases of bulk liquids [96, 97], but diverges strongly in the longtime limit due to the imaginary-frequency INMs. It is worth mentioning that for the Ag-atom $C_i(t)$ at $T$ = 900 K both the stable-INM approximation and the simulation result display an over-damped behavior over a long time scale. At the same temperature 900 K, the behavior of $C_i(t)$ obtained by simulations for the Cu atom is, however, under-damped in noticeable contrast to that in the stable-INM approximation showing too fast damping (see Fig. 5.9).

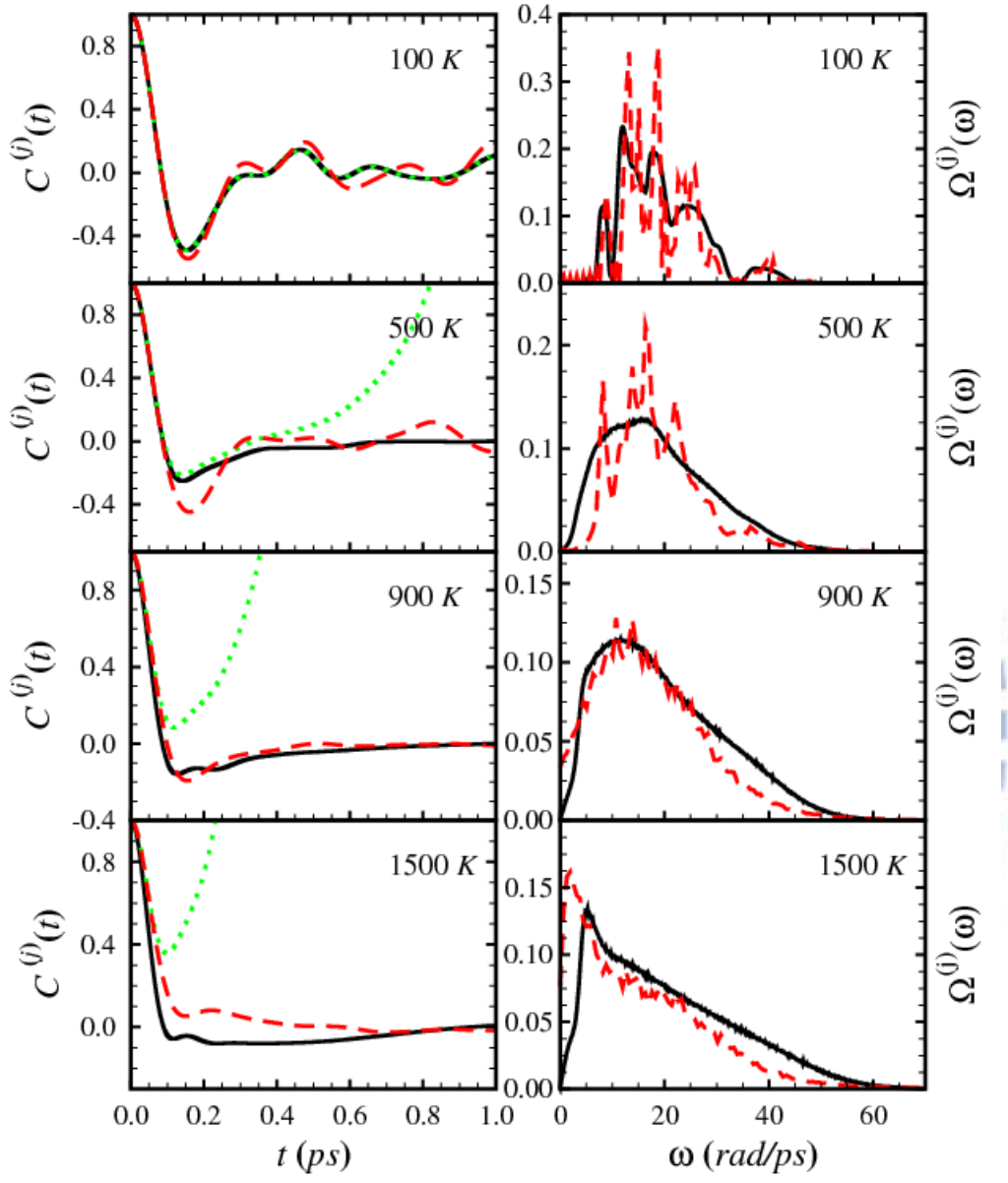


Fig. 5.8. VAF $C_j(t)$ and power spectrum $\Omega^{(i)}(\omega)$ of an Ag atom in $Ag_{17}Cu_2$ at 100, 500, 900, and 1500 K. The Ag atom is one in the $Ag^{(10)}$ subset [see Fig. 3.4]. For $C_j(t)$ and $\Omega^{(i)}(\omega)$, the full lines are the results calculated in the stable-INM approximation and the dashed lines are the results from MD simulations. The dotted lines in $C_j(t)$ are results calculated with both real- and imaginary-frequency INMs. All vibrational INM spectra used in the calculations are obtained by *Method II*.

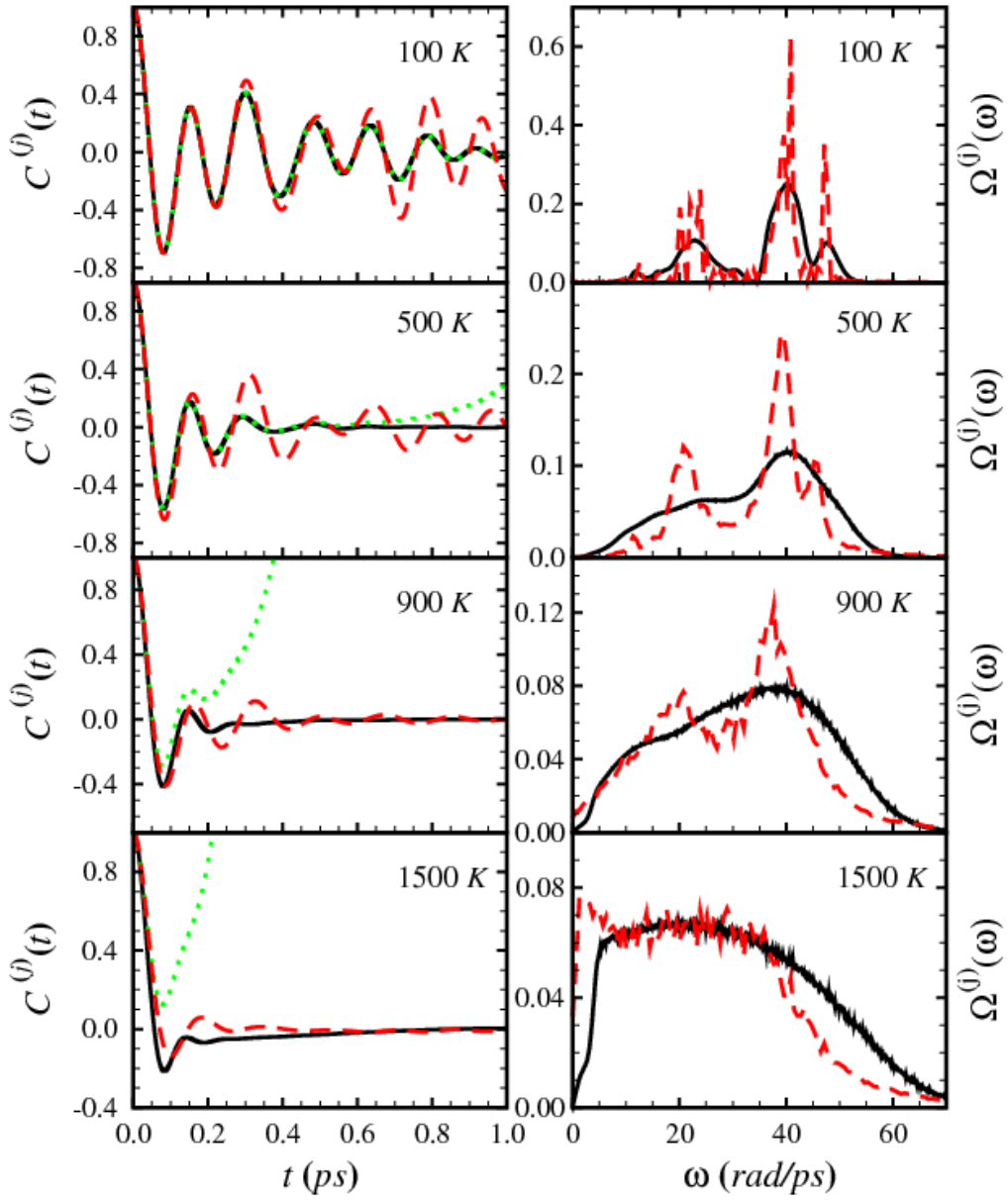


Fig. 5.9. VAF $C_j(t)$ and power spectrum $\Omega^{(i)}(\omega)$ of a Cu atom in $Ag_{17}Cu_2$ at 100, 500, 900, and 1500 K. The Cu atom is in the $Cu^{(2)}$ subset [see Fig. 3.4]. For $C_j(t)$ and $\Omega^{(i)}(\omega)$, the full lines are the results calculated in the stable-INM approximation and the dashed lines are the results from MD simulations. The dotted lines in $C_j(t)$ are results calculated with both real- and imaginary-frequency INMs. All vibrational INM spectra used in the calculations are obtained by *Method II*..

## 5.3 Temperature variation of $I_j$

We are now in a position to study the temperature variations of $I_j$ for the four subsets of atoms. In the upper part of Fig. 5.10, the $I_j$ , which is calculated with the vibrational INM that follows *Method II*, is plotted at a temperature increment of 10 K from $T$ =10 to 1500 K. The $I_j$ values of the $Cu^{(2)}$ subset of atoms are almost constant at low temperatures and, around 500 K, start to decrease gradually with increasing temperature. Though having a declining behavior with temperature, the $I_j$ of $Cu^{(2)}$ is well separated from those other three subsets of Ag atoms for the range of temperature considered here due to the difference in masses of Ag and Cu atoms. In the lower part of Fig. 5.10, we compare the $I_j$ of each subset of atoms calculated with the vibrational INM applying either *Method I* or *Method II*. It is evident that the calculated results by the two methods for the three subsets of Ag atoms are rather similar. On the other hand, we find that both $I_j$ of $Cu^{(2)}$ subset of atoms obtained by the two methods exhibit similar temperature behavior and coincide at low temperatures but are well separated at high temperatures, with the temperature change for the $I_j$ value by *Method I* starting to decrease around 800 K.

It is interesting to see in the upper part of Fig. 5.10 that the $I_j$ of the three subsets of Ag atoms split into three branches below 450 K and, as $T \rightarrow 0K$, the $I_j$ values of the three subsets of atoms converge to the values of $I_j^{(LES)}$ defined in Eq. (2.44). From $T$ = 450 to 600 K, the three branches of the subsets of Ag atoms are still visibly separated. These well-resolved branches are, however, somewhat defiled by exchanges between two branches which correspond physically to site permutations between Ag atoms (for examples, $Ag^{(2)} \leftrightarrow Ag^{(10)}$ and $Ag^{(5)} \leftrightarrow Ag^{(10)}$). Between $T$ = 600 and 900 K, the $I_j$ of the three subsets of Ag atoms start to mix interchangeably and these branches are no longer discernible. The $I_j$ gradually lose the identities of the original subsets of atoms with increasing temperature. After $T$ = 900 K, the $I_j$ of all Ag atoms merge into one so that the cluster is distinguished by two $I_j$ branches corresponding to a thorough mixing of the two Cu atoms and among the Ag atoms.

We delve further into the dynamics of Ag atoms by the $I_j$ temperature variation of each subset of Ag atoms illustrated in the lower part of Fig. 5.10. Below $T$ = 450 K, the structures of the three subsets of Ag atoms mimic that of the LES implying that these atoms possibly vibrate with small amplitudes about their solid-like equilibrium positions. From $T$ = 450 to 600 K, the thermal variation of the $I_j$ of each subset of Ag atoms indicates that the Ag atoms are undergoing sites exchange between subsets of atoms whose structures remain dynamically similar to those of the LES configuration. In this temperature segment, it is also possible that the three subsets of Ag atoms are displaced in their sites and driven to higher local minima by thermal activations over the barriers in the potential energy landscape; At much higher temperatures falling between $T$ = 600 and 900 K, the probability to surmount energy barriers into even higher energy states increases and such large probabilities indicate that the cluster at this point will stray far from the lowest energy structure. Correspondingly, within this temperature range, the $C_V$ shown in Fig. 5.1 increases dramatically and reaches a maximum at $T$ = 900 K. Above $T$ = 900 K, the solid-like structure could have "melted," with the Ag atoms completely indistinguishable under an ensemble average, and as a result the $C_V$ undergoes a sharp drop with the temperature increasing further.

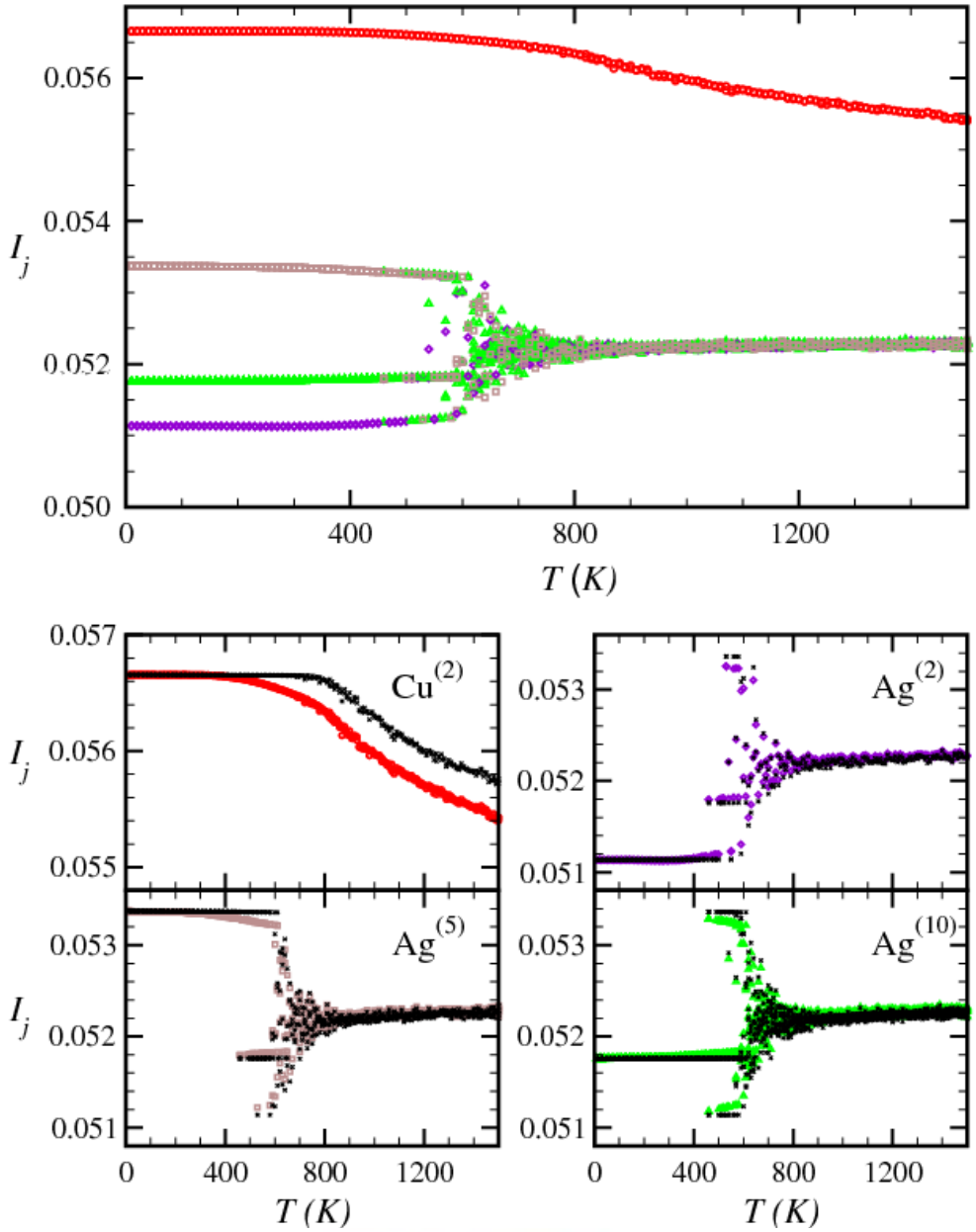


Fig. 5.10 Temperature variations of $I_j$ for the atoms in the four subsets of $Ag_{17}Cu_2$: $Cu^{(2)}$ (red circles), $Ag^{(2)}$ (magenta diamonds), $Ag^{(5)}$ (brown squares), and $Ag^{(10)}$ (green triangles) (see Fig. 3.4). The $I_j$ values in the upper panel are obtained from the vibrational INM by *Method II*. In the lower four panels, each figure compares the $I_j$ of a subset of atoms with its vibrational INM obtained by *Method I* (black crosses) and that by *Method II* (same symbols as in the upper panel).

## 5.4 Order parameter $\tau(T)$ for melting of $Ag_{17}Cu_2$

In physics, the melting phenomena are commonly described by some appropriately chosen order parameters. In bulk systems, the first-order melting transition is characterized by a discontinuous jump in the order parameter, which can be $C_V$, at the melting temperature, whereas in finite-sized systems such as clusters the same kind of transition is featured by a continuous change of $C_V$ with temperature and it embodies the coexistence of the solid-like and liquid-like isomers [21, 22, 25, 75, 78, 98]. Several other order parameters have been reported also and applied to understand the solid-like to liquid-like transition in clusters. On the issue of coexisting the solid-like and liquid-like isomers, the microcanonical ensemble simulations [35, 47- 49] have associated the bimodality in the probability distribution of the short-time averaged temperature as *prima facie* evidence. These simulation studies have aroused subsequent interest in finding the solid-like and liquid-like states separated by a barrier in the Landau free energy, and the potential energy then serves as the order parameter of the free energy [51]. Parallel to appealing to the energy order parameters, the geometric order parameters that base upon the short-time average are used as well for addressing the transition between two stable isomers and their coexistence [52], and also the bond-orientational order parameters for investigating the structural variation along pathways in configuration space [53, 54]. We should perhaps mention the continual use of the root-mean-square bond length fluctuation constant $\delta$ as a Lindemann-like order parameter in more recent computer simulations [46, 57, 58]. Despite the drastic change of this order parameter with temperature indicating some kind of structural or phase transformation in bulk systems, the information of the transition deduced from $\delta$ for clusters is, however, not always consistent [45, 57] with that inferred from $C_V$ thus lending less credence to choosing $\delta$ as an insightful order parameter to study phase transition.

Within the context of the INM analysis developed in Chapter 2, the new order parameter given in Eqs. (2.62)-(2.64) by INM is defined for pure clusters. Since $Ag_{17}Cu_2$ is a bimetallic cluster, we, thus, define the order parameter for this cluster in a similar way but only for Ag atoms. Toward this goal, the equation $\tau(T) = \sigma_I(T)/\sigma_I(0)$ in Eq. (2.62) is unchanged, where $\sigma_I(T)=\left(\overline{I_j^2} - (\overline{I_j})^2\right)^{1/2}$. Here, the average denoted by bar is among the Ag atoms so that

$$\overline{I_j^\ell} = \frac{1}{n_{Ag}} \sum_{j=1}^{n_{Ag}} I_j^\ell \tag{5.2}$$

where $n_{Ag} = 17$. The calculated $\tau(T)$ is shown in Fig. 5.11. With the $I_j$ values obtained by *Method II*, $\tau(T)$ is almost one below $T$ = 300 K signaling that the ground-state structure is well preserved. From $T$ = 300 to 600 K, $\tau(T)$ declines from 1 to 0.85 which again indicates that the LES structure is generally maintained. The $\tau(T)$ starts to drop sharply at $T \approx$ 600K and approaches asymptotically to a small value at a temperature close to $T_m \approx$890 K. This sharply decaying range of $\tau(T)$ marks a melting shake-up of the ground-state structure. The $\tau(T)$ stays constant at temperatures $T > T_m$ and is non-zero due to the finite size of the cluster. Physically, it describes the atomic distributions that, under ensemble averages,

exhibit no further distinction among the Ag atoms at much higher (than $T_m$) temperatures. Thus, the phenomenon of cluster melting described by $\tau(T)$ is consistent with the thermal behavior of $C_V$ shown in Fig. 5.1. Except for the constant one extending up to ~600 K, the temperature variation of $\tau(T)$ calculated from the $I_j$ values following either *Method I or Method II* is quite similar. This result indicates that the decline of $\tau(T)$ from $T$ = 300 to 600 K by *Method II* is related to the rotation-vibration coupling in the $Ag_{17}Cu_2$ cluster with the Gupta potential.

In recapitulation, we remark that the INM averages in $\tau(T)$ are carried out for the configurations that evolve along the long-time cluster trajectories, and that the underlying statistical average for the order parameter is based upon the canonical ensemble at each temperature. Though under different statistical averages, the indication of $\tau(T)$ for the transition of cluster melting are complementary to those obtained by another INM analysis under the short-time average in the microcanonical ensemble [49].

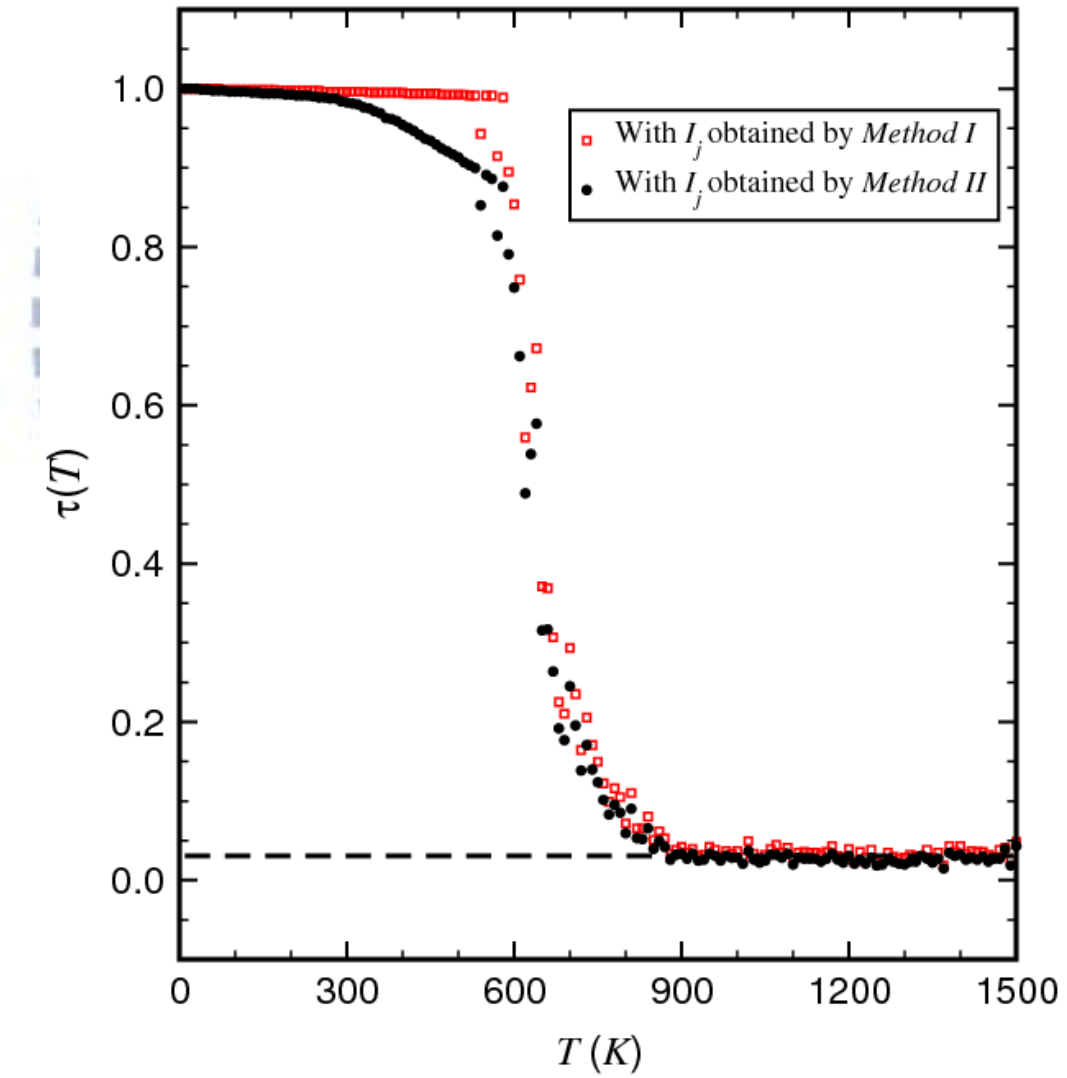


Fig. 5.11 Order parameter $\tau(T)$ *vs* temperature $T$ (K) calculated with the $I_j$ values of Ag atoms in $Ag_{17}Cu_2$ (shown in Fig. 5.10) obtained by *Method I* (open squares) or *Method II* (filled circles). The dashed line is the asymptotic high-$T$ value of $\tau(T)$.

## 5.5 Summary

We have the isothermal Brownian-type molecular dynamics to calculate the specific heat $C_V$ of the $Ag_{17}Cu_2$ cluster. Velocity autocorrelation function, and its time Fourier-transformed power spectral density. These quantities were analyzed and the dynamical behavior of individual atoms as a function of temperature, the power spectral density, in particular, was examined. In Fig. 5.9, we found that the highest frequency mode $\Omega^{(\mathrm{Cu})}(\omega_H)$ of the Cu atom, which is located at $\omega_H \approx 45$ rad/ps, disappears identically at a temperature within $800 < T \leq 900K$. This temperature was used to infer the melting temperature of the $Ag_{17}Cu_2$ cluster, which we define the main peak position of $C_V$ at $\mathrm{T_m} \approx 890\mathrm{K}$ as the melting temperature of the $Ag_{17}Cu_2$ cluster. The dynamical properties of $Ag_{17}Cu_2$ were further diagnosed using the INM analysis. In addition to the vibrational mode DOS agreeing favorably with the simulation results, we observe that the frequency integrated value $I_j$ which is an ensemble average of all vibrational projection operators for the *j*-th atom in the cluster changes with temperature in a characteristic manner that sheds considerable light on the melting behavior. A detailed examination of the $I_j$ of Ag atoms leads furthermore to a new order parameter $\tau(T)$. The INM analysis shows that $\tau(T)$ contains cluster dynamic information and also predicts the $T_m$ of $Ag_{17}Cu_2$ reasonably close to that inferred from $C_V$. In view of this finding, the $\tau(T)$ derived in this work is a promising order parameter for understanding the cluster thermal property as well.

# Chapter 6
# INM Analysis for Melting Behavior of $Ag_{14}$ Cluster

## 6.1 Introduction

In the previous chapter, I have studied the dynamics and melting behavior of $Ag_{17}Cu_2$ from the viewpoint of potential energy landscape [59, 60] by exploiting the INM analysis [61, 62] in the context of the canonical ensemble average. In that study, a new order parameter was proposed in terms of the INM vibrational density of states (DOS) that are associated with the Ag atoms in the cluster [79]. This order parameter interprets pretty well the melting behavior of $Ag_{17}Cu_2$ and the predicted $T_m$ is in fairly good agreement with that inferred from the specific heat $C_V$ of the cluster [81].

In this chapter, I study the melting transition of metallic cluster $Ag_{14}$ based on a generalization of the INM analysis described in Chapter 2. In the $C_V$ curve of $Ag_{14}$, an additional prepeak occurs at a lower temperature, which is not observed in the $C_V$ of $Ag_{17}Cu_2$. The reason can be traced back to that their respective lowest-energy structure (LES), which have been described in Chapter 3, are quite different geometrically. According to previous studies for $Cu_{14}$ whose $C_V$ also shows a main peak and a prepeak as that of $Ag_{14}$, the origin of the prepeak is due to the migrational relocation of the floating atom in the cluster as the temperature of the cluster is raised from the LES. Similarly, one may expect that the migrational relocation of the floating atom in $Ag_{14}$ causes the occurrence of the prepeak in the $C_V$ curve. To confirm this argument further, I apply the INM for the $Ag_{14}$ cluster and examine the applicability of the new order parameter for the prepeak phenomenon, whose mechanism is further investigated by probing the potential energy landscape.

The calculated $C_V$ of $Ag_{14}$ has been shown in Fig. 6.1, which is referred from Ref. [81]. As shown there, the main maximum of $C_V$, which is defined as the melting temperature $T_m$, is located at approximately 920 K. Besides the main peak, one notices a prepeak structure near 300 K. However, one can find from Fig. 6.2 that the drastic change of the root-mean-square bond length fluctuation

constant $\delta$ is not consistent with the positions of the main peak and the prepeak of $C_V$ data. The first drastic change in $\delta$ roughly occurs from 150 to 200K and the second occurs at 450K with an extension to 500K; both drastic changes happen before the melting of the cluster as raising temperature. This inconsistence also happens to $Ag_{17}Cu_2$.

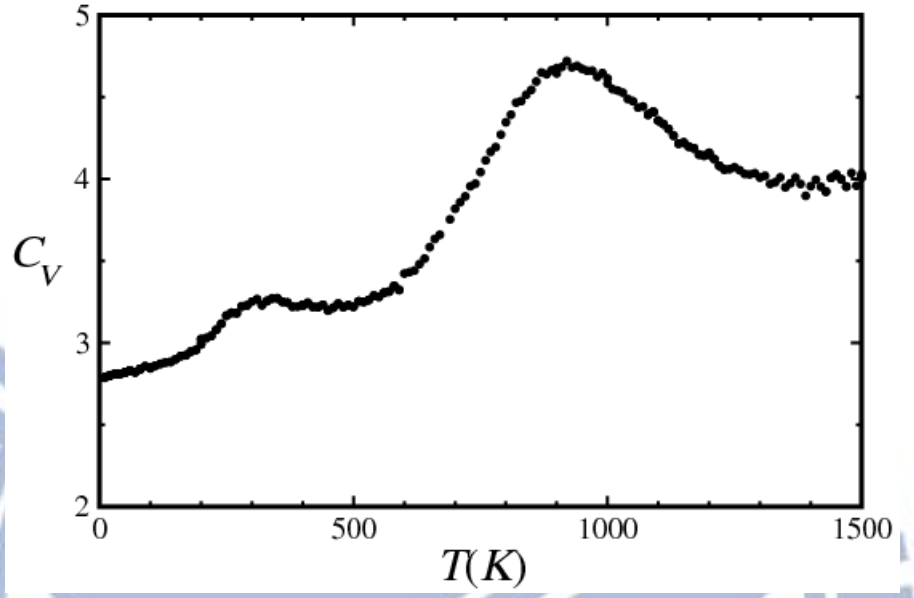


Fig. 6.1 Specific heat $C_V$ of $Ag_{14}$ (closed circle) calculated using the isothermal Brownian-type MD simulation [81].

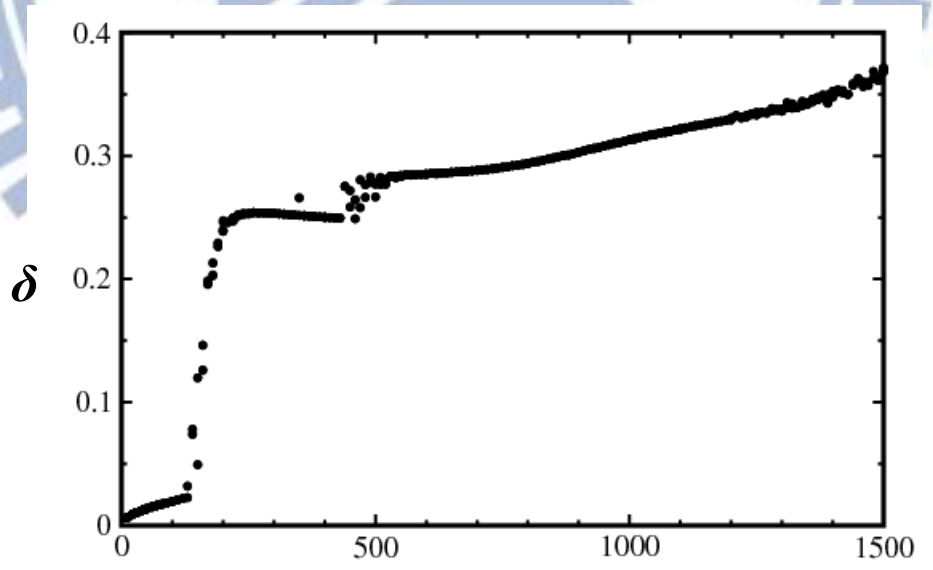


Fig. 6.2 The variation of the root-mean-square bond length fluctuation constant δ with temperature for $Ag_{14}$ [95].

## 6.2 Vibrational DOS of lowest energy state by decomposition method

Several theoretical studies on the structures and the vibrational modes of metallic clusters that employ the Gupta potential have been reported in the literature [83, 99]. Depicted in Fig. 6.3(a) are the vibrational modes of $Ag_{14}$ in the LES. Due to the $C_{3v}$ symmetry, the vibrational frequencies are either nondegenerate or doubly degenerate. Removing away the floating (*F*) atom, I also calculate and compare the vibrational modes of the deformed icosahedron and the relaxed perfect one and these latter two results are shown in Fig. 6.3 (b) and Fig. 6.3 (c), respectively. As indicated by the degeneracies of the vibrational modes, the deformed icosahedron reflects the symmetry of the $C_{3v}$ point group, whereas the relaxed icosahedron, with the $I_h$ symmetry, correctly produces the vibrational modes with fivefold, fourfold, and threefold degeneracies [99].

Some vibrational modes of $Ag_{14}$ are interesting. The three highest-frequency modes, the singlet at 40.8 rad/ps and the doublet at 41.8 rad/ps, generally describe central (*C*) atom inside the deformed icosahedron oscillating parallel and perpendicular to the principal axis, respectively. The singlet at 31 rad/ps is the breathing mode, describing the motion of atoms along lines from the atoms to the *C*-atom. Comparing the vibrational modes of the Ag clusters with and without the *F* atom, we find three extra modes due to the presence of the *F* atom and they are the singlet at 33.2 rad/ps and the doublet at 7.35 rad/ps, which describe generally the stretching and shearing vibrations between the *F* atom and the deformed icosahedron, respectively. The other modes with frequencies 10–26 rad/ps mainly come from the vibrational modes of the perfect icosahedron, with a reduction in some degeneracies due to the change in group symmetry from $I_h$ to $C_{3v}$ and a shift in their frequencies by the presence of the *F* atom.

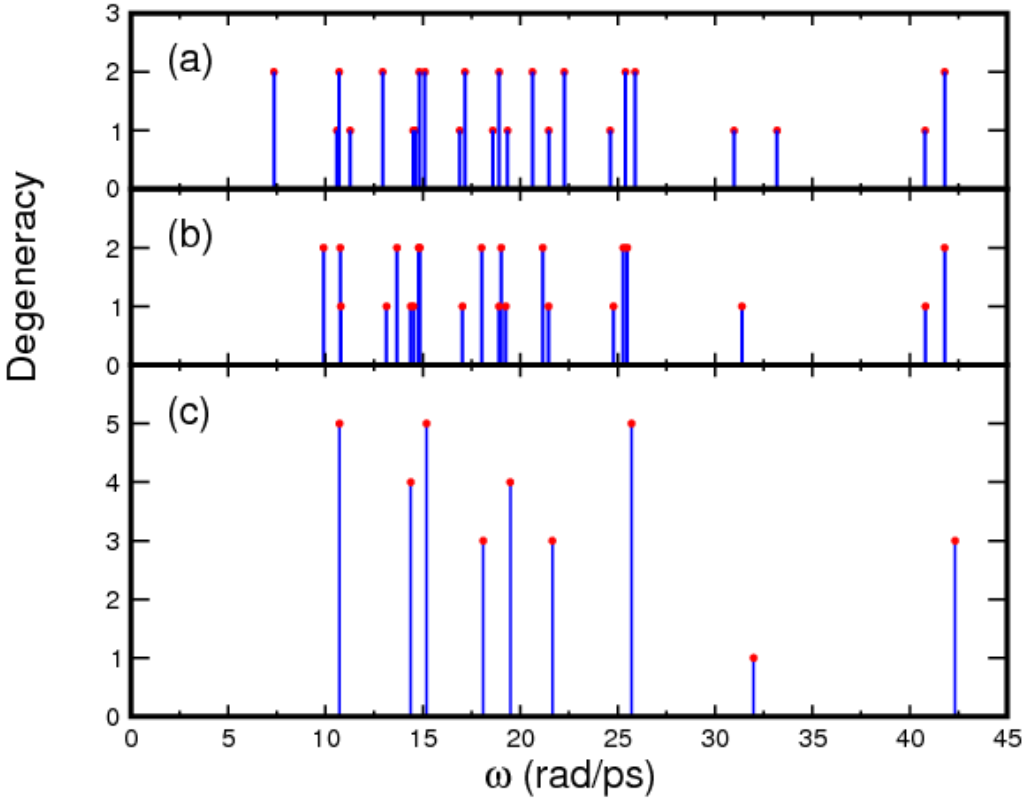


Fig. 6.3 Vibrational frequencies of Ag clusters: (a) the LES of $Ag_{14}$, (b) the deformed icosahedron obtained by removing away the *F* atom from the LES, (c) the perfect icosahedron obtained by relaxing the deformed icosahedron. In each panel, the blue straight lines indicate the frequencies of the vibrational modes and the red dots specify the degeneracies of the modes.

## 6.3 Temperature variation of the INM spectra

### 6.3.1 Vibational DOS

A total number of $10^6$ configurations was generated by the Brownian-type MD simulations that run at a time step of 1 fs corresponding to a total time interval of 100 ns. Fig. 6.4 depicts the normalized INM vibrational spectra of $Ag_{14}$, obtained by subtracting the contribution of the rotational INMs described in Sec. 2.2.2 by two methods. From low to high temperatures, we find no noticeable difference in the vibrational spectra obtained by the *Method I* and *Method II*. I also calculate the projection $J(L_k)$ to measure the rotation-vibration coupling and results are presented in Fig. 6.5. The two subspaces spanned by the two sets of rotational eigenvectors obtained by Method I and Method II completely overlap at zero temperature and still overlap to a large extent at low temperatures, with a temperature range less than that in Fig. 5.4 for $Ag_{17}Cu_2$. Among the three INMs of $(L_1, L_2, L_3)$, the order in the $J(L_k)$ magnitudes from the largest to least values still follows the sequence of the three INMs $(L_1, L_2, L_3)$ at all temperatures. The overlapping of the two subspaces from low to high temperatures decays faster than that for $Ag_{17}Cu_2$ but the $J(L_k)$ values at $T$ = 1500 K, with $J(L_1)$ roughly lowering to 70% and $J(L_3)$ to 45%, are relatively larger than those of $Ag_{17}Cu_2$ at the same temperature, implying a weaker rotation-vibration coupling as compared with $Ag_{17}Cu_2$ at the same temperatures. Therefore, I still discuss the vibrational INM spectra calculated by *Method II* and calculate the $I_j$ and $\tau(T)$ by *Method I* or/and *Method II* for comparison.

Back to Fig. 6.4, the $D_{vib}(\omega)$ of $Ag_{14}$ at $T$=100K possesses only the real-frequency lobe, indicating that the cluster displays by and large a solid-like characteristic. Examining closely the cluster configurations at this temperature, we find that they are still around the LES of the potential energy landscape, preserving generally the structure in the LES. As the temperature increases to 200 and 300K, the INM spectra are more smoothed out than 100K and the vibrational modes with imaginary frequencies emerges very early at 200K, which suggests a transition process has already occurred at lower temperature for the barrier between the LES and the first-excited energy state is relatively low to overcome. For the real-frequency branch of vibrational DOS, one noticeable feature is that the high frequency peak at 40rad/ps gradually decrease as temperature increasing from 450K to 700K, while the vibrational DOS display a significant portion of imaginary-frequency INM, which implies the cluster may possesses enough kinetic energy to crossover the energy barriers to the first- or higher-excited minima, the high frequency peak of 40rad/ps at T=300K becomes as shoulder at 450K and almost disappears at 700K. As temperature is increased further to 900 K, the INM spectra display a large portion of imaginary-frequency vibrational INM and the high frequency peak of 40rad/ps is disappeared. This structural traits are similar as the case of $Ag_{17}Cu_2$.

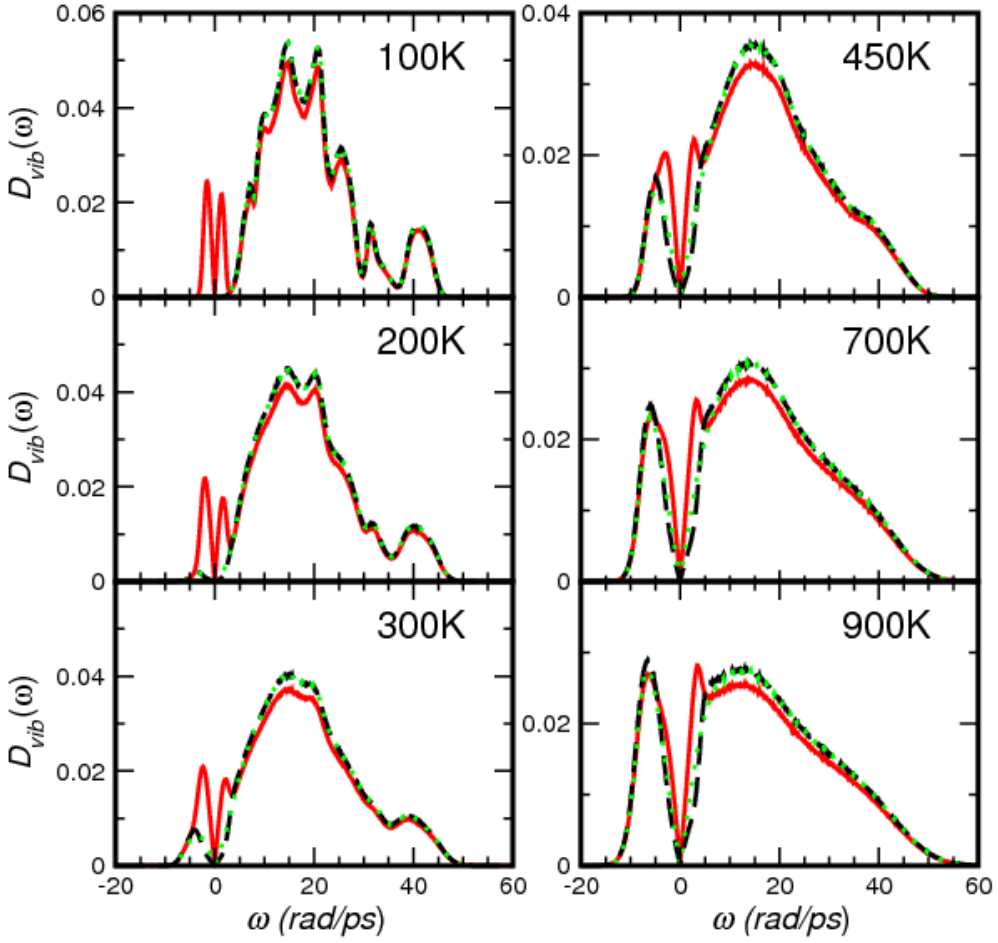


Fig. 6.4 Normalized INM spectra $D_{vib}(\omega)$ of $Ag_{14}$ at 100, 200, 300, 450, 700, and 900 K. The red-solid lines are the spectra showing the contributions of both rotations and vibrations. The back-dashed and green-dotted lines are the spectra obtained by removing the rotational contribution following *Method I and Method II* described in Sec. 2.2.2, respectively.

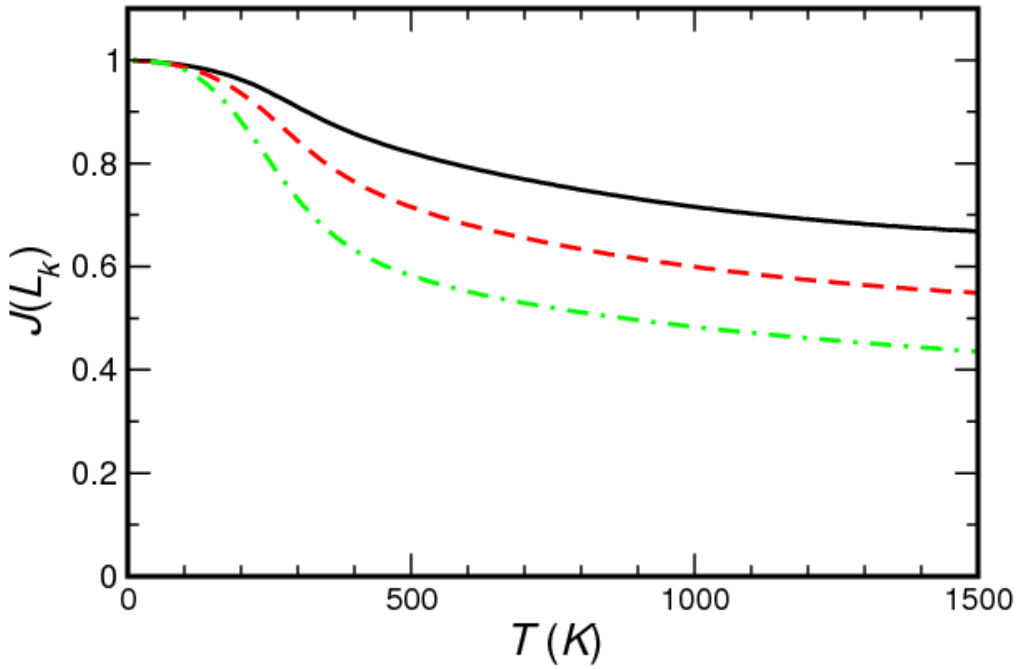


Fig. 6.5 Temperature variation of $J(L_k)$ for measuring the projection of the INM with $L_k$ onto the subspace spanned by the three purely rotational eigenvectors for $Ag_{14}$ cluster. The black-solid, red-dashed, and green-dotted-dashed lines are for the INM with $L_1$, $L_2$ and $L_3$, respectively.

### 6.3.2 Projected vibrational DOS

It is instructive to dig out the relation between the projected vibrational spectral of a subset of atoms and the symmetry of cluster structure. To this end, I use the average projected vibrational spectrum of a subset *X* of atoms, defined in Eq. (5.1), with *X* denoted as one of the six subsets *C*, *F*, $S_1$, $S_2$, $S_3$ and $S_4$ (see Fig. 3.2). The structural information in $D_X(\omega)$ reflects the effects of cluster symmetry on the vibrational spectrum. The comparison between $D_X(\omega)$ of $Ag_{14}$ at 100 K and that of the LES is given in Fig. 6.6. The $D_X(\omega)$ spectra of the *C* atom at 100 K have two main distributions whose positions of peaks are at $\omega \approx 17$ and 41.5 rad/ps coinciding with the thin straight lines of $D_X(\omega)$ at the LES. Hence, the spectra of $D_X(\omega)$ at 100 K are the consequence of the thermal effect driving the cluster structure to deviate from the LES of the potential energy landscape. The spectrum of the *F* atom has three main peaks at $\omega \approx 7$, 11.2, and 34 rad/ps, a plateau around 20 rad/ps, and almost without any mode with $\omega > 40$ rad/ps. Among these the peaks at 7 and 34 rad/ps are related to the shearing and stretching vibrations between the *F* atom and the deformed icosahedron, respectively. For the subsets of $S_1$, $S_2$, $S_3$, and $S_4$, an ubiquitous feature of their $D_X(\omega)$ is a continuous frequency distribution that extends the range $\omega \approx$ 5–45 rad/ps with a deep valley around 36 rad/ps. Scrutinizing these four spectra in great details, we find their $D_X(\omega)$ around 31 rad/ps at which the breathing mode occurs in the LES have an

almost equal magnitude. On the other hand, one can tell apart the difference between the spectrum of the $S_1$ subset, which directly links to the *F* atom, and those of the other $S_i$ ($i$ = 2, 3, 4) subsets. At LES and 100 K, the $D_X(\omega)$ spectrum of the $S_1$ subset has a relatively larger magnitude at around 34 rad/ps than the other three subsets. However, both $D_X(\omega)$ of the $S_1$ and $S_2$ subsets have almost equal magnitude at $\omega \approx 7$ rad/ps, which is larger than those of the $S_3$ and $S_4$ subsets. These results point to the quite general feature that the stretching vibration between the *F* atom and the deformed icosahedron only extends to atoms of the $S_1$ subset but the shearing vibration extends further to those of the $S_2$ atoms.

To explore further the temperature effect on the projected vibrational spectrum of individual atom in $Ag_{14}$, we display in Fig. 6.7 the variations of $D_j(\omega)$ from 50 to 1000 K for all atoms. At 50 K, the structural characteristics of $D_j(\omega)$ are well discernible for the *C*, *F*, and $S_i$ atoms. Up to 100 K, the $D_j(\omega)$ spectra do not contain any imaginary-frequency INM and are rather similar to the power spectra obtained by the Fourier-transform of the velocity autocorrelation functions of individual atoms presented in Ref. [81]. The $D_j(\omega)$ of the surface atoms are generally indiscernible at 150 K, and they are seen to merge with the spectrum of the *F* atom at 200 K into an almost single spectrum, with the appearance of some imaginary frequency modes and weak structures in the real frequency lobe. This mergence of $D_j(\omega)$ indicates that the *F* atom has indistinguishably integrated with the surface atoms at 200 K. For temperature higher than 200–400 K, only two kinds of distinguishable $D_j(\omega)$ spectra are observed and they come from the *C*-atom and the rest of atoms. However, some interesting things happen at 450 K. Discernible from other subsets as well, the $D_j(\omega)$ spectra of the $S_3$ atoms clearly show a shoulder at 40 rad/ps, a value close to the frequencies of the *C*-atom oscillating inside the cage of the deformed icosahedrons in the LES. The occurrence of the shoulder suggests that at this temperature there is some possibility for the $S_3$ atoms to occupy the central position of the deformed icosahedron. When entering into 500 K, the $D_j(\omega)$ of the *C*-atom is still separated from those of the rest of atoms. At this temperature its high-frequency peak is located at around 40 rad/ps but shifts slightly toward smaller frequency accompanying by a decline in amplitude. In contrast, the originally merged $D_j(\omega)$ of the rest of atoms are somewhat blurred and have a conspicuous hump falling in the frequency range of the shoulder observed in the spectra of the $S_3$ atoms at 450 K. As the temperature goes up further to 600 K, the $D_j(\omega)$ spectra of all atoms, including the *C*-atom, are mixed up. In fact, one still detects a weak hump on the high-frequency side at $\omega \approx 40$ rad/ps. The occurrence of this high-frequency hump demonstrates that the structure of the cluster at this temperature still has an atom centrally resided inside the cage formed by other atoms but this central atom may not be the *C*-atom. The hump disappears for $T > 600$ K and all $D_j(\omega)$ spectra are seen to coalesce and display a large portion of imaginary frequency INMs, whereas the real-frequency lobe develops into a roughly triangular shape that is often observed in the INM spectra of simple liquids [64, 100]. These characteristics of $D_j(\omega)$ are reminiscent of $Ag_{17}Cu_2$ in the liquid-like phase and point to same behaviors of $Ag_{14}$ whose atoms at such high temperatures would have gone around everywhere the potential energy landscape [79].

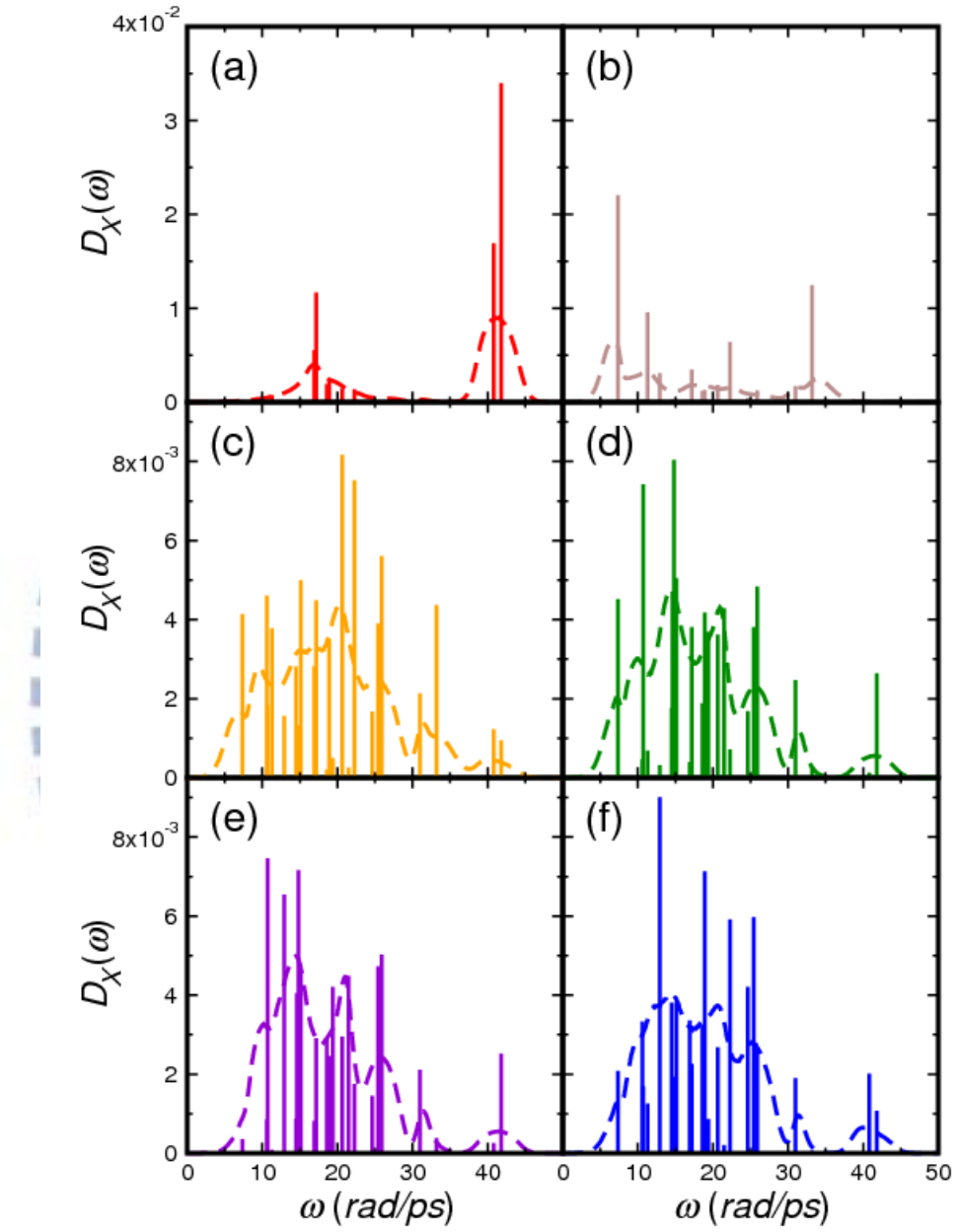


Fig. 6.6 Vibrational DOSs, $D_X(\omega)$, of subset $X$ of $Ag_{14}$, with (a) $X$=$C$, (b)$X$=$F$, (c) $X$=$S_1$, (d) $X$=$S_2$, (e) $X$=$S_3$, and (f) $X$=$S_4$. The six subsets are referred to in Fig. 3.2. In each panel, the thin straight lines are for the LES and the dashed curve is an ensemble average over cluster configurations at 100 K

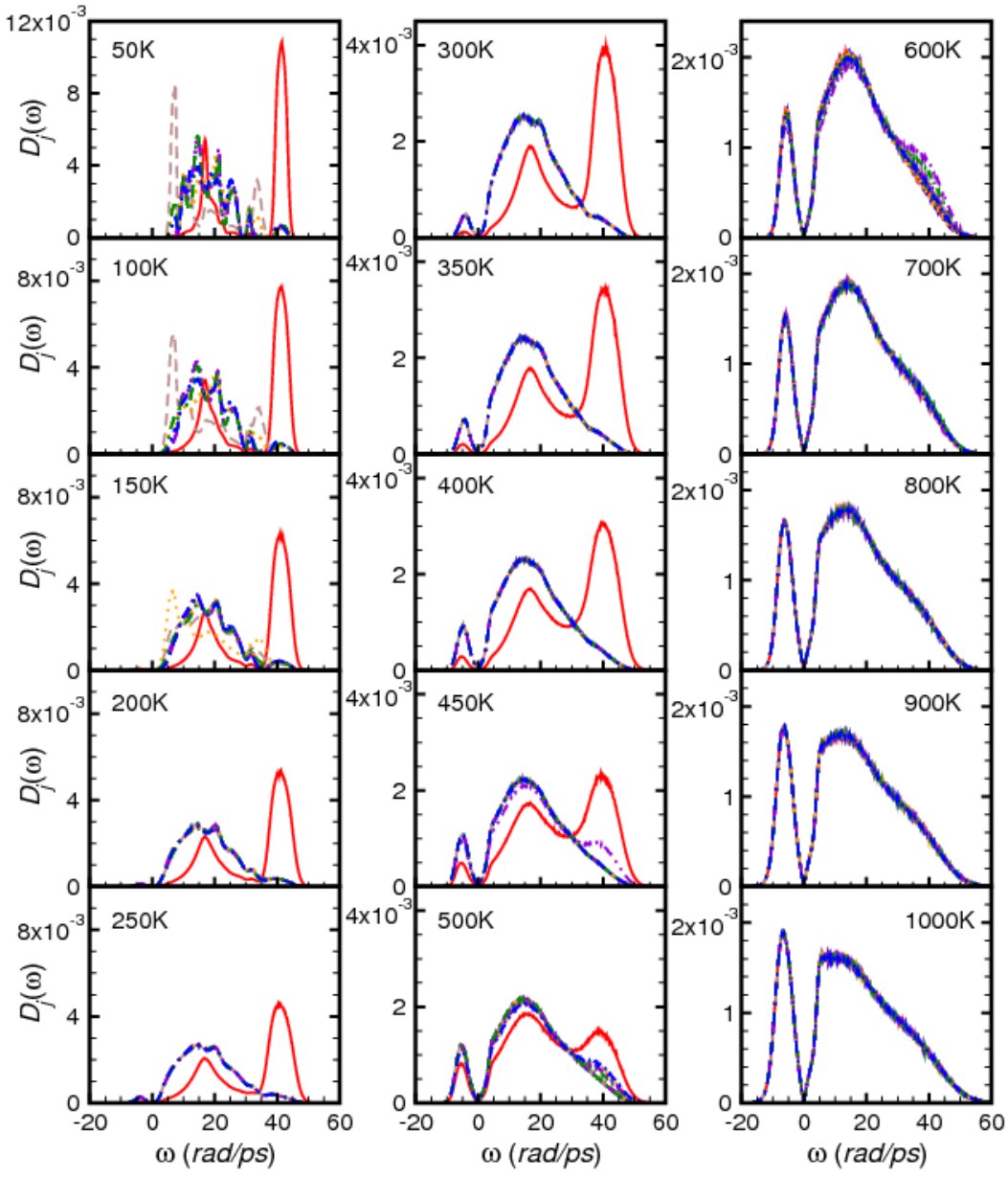


Fig. 6.7 Projected vibrational spectra $D_j(\omega)$ of individual atoms in $Ag_{14}$ at indicated temperatures. The spectra are obtained by following *Method II*. The solid (red) and dashed (brown) lines are for the *C* and *F* atoms, respectively. The dotted (orange), dotted-dashed (green), dotted-dotted-dashed (violet), and dotted-dashed-dashed (blue) lines refer to the atoms of the $S_1$, $S_2$, $S_3$, and $S_4$ subsets, respectively.

## 6.4 Temperature variation of $I_j$

The temperature variations of the $I_j$ values for all atoms are presented in Fig. 6.8. With a temperature increment of 10 K from $T$ = 10 up to 1500 K, the data at each $T$ are calculated by averaging over $10^6$ configurations. In the upper panel of Fig. 6.8, the $I_j$ values of the six subsets of atoms are specified by different symbols and they are obtained by an integration of each $D_j(\omega)$ curve (see Fig. 6.7) with the vibrational INMs described by the *Method II*. In the lower panel of Fig. 6.8, we make a comparison between the $I_j$ values obtained by two different methods, one via the integral of $D_j(\omega)$ and the other via Eq. (2.41) in which the translational projection is calculated straightforwardly and the rotational projection is evaluated with the purely rotational eigenvectors given in Eq. (2.23). As evidenced in Fig. 6.8, the two methods for the six subsets of atoms yield rather similar results in $I_j$.

Let us look first at the lower panel of Fig. 6.8. One sees that the $I_j$ curves of all atoms below 150 K are well split into six branches, with each branch corresponding to a subset of atoms. The six branches show that the LES is well preserved. For the *F* and *C* atoms, it is easy to understand their branches as due to their unique positions in the LES, whereas for the four $S_i$ subsets of atoms, it is, however, relatively less simple to interpret the splitting of their $I_j$ branches as connecting to the geometry of the deformed icosahedron. To delve more deeply into the $I_j$ branches, we examine Fig. 6.8 more closely. First of all, we find that between 100 and 150 K the *F* atom declines weakly in the $I_j$ value obtained by *Method II*. What happens to the *F* atom in this temperature range is that the atom possibly relocates from a triangular facet to a nearby one by migrating over their common edge. This mechanism, which involves two steps, is shown in Fig. 6.9 by a potential energy barrier which is estimated to be 97 K. These migration and relocation movements of the *F* atom were previously observed also in $Cu_{14}$ [46]. Shown in Fig. 6.9 , this two-step mechanism can be elucidated further as follows: From (a) to (b), a bond that connects the F (brown) and one of $S_2$ (green) atoms is formed, in contrast to the breaking of the bond between the two $S_1$ (orange) atoms connecting to the $S_2$ atom. From (d) to (e), the broken bond is re-bonded, whereas the bond connecting the F and the third $S_1$ atoms is broken. In all calculations, the bond length is set equal 3.5 Å .

In Fig. 6.8, we find exchanges in the $I_j$ values among the *F* and the $S_i$ atoms spanning the temperature range 150–200 K. These exchanges can be understood by a three-step mechanism shown in Fig. 6.10, where the role of the *F* atom as one floating outside the deformed icosahedron is replaced by one $S_1$ atom with the occurrence of site exchanges among other $S_i$ atoms. The overall potential energy barrier in this three-step mechanism is about 127 K. The following describes in more details the site-permutation mechanism illustrated in Fig. 6.10 for the F (brown) atom exchanging with one of $S_1$ (orange) atoms and, as a result, the $S_1$ atom playing the role as the one floating outside the deformed icosahedron. The path from (a) to (c) results in the bonding of the F atom with one of $S_2$ (green) atoms and the breaking of the bond between two $S_1$ atoms both linked to the $S_2$ atom. As in Fig. 6.9, we set two atoms as bonded when their distance is within 3.5 Å . From (c) to (d), the F and C (red) atoms are thus connected, while the $S_1$ and $S_2$ atoms that are simultaneously linked to the F atom are unbonded.

From (d) to (e), the $S_1$ atom which is disconnected from the $S_2$ atom plays the role as a new floating atom after its bond with the C atom breaks up, while the F and one $S_3$ (violet) atoms which both connected to the new floating atom are bonded. From (f) to (g), the F and another $S_2$ atoms are bonded and, on the same occasion, the new floating atom is seen to be disconnected from the $S_3$ atom that has linked to the F atom.

At temperatures higher than 200 K, the five branches of the $I_j$ values, presented in Fig. 6.8, for the subsets of *F* and $S_i$ atoms show tendency to coalesce and become completely indiscernible at $T \approx 300$ K. Dynamically, this would correspond to the picture that the *F* atom seeps into the deformed icosahedron and merges with the $S_2$, $S_3$, and $S_4$ atoms. The complete merger of the five branches at around 300 K implies that the structure of $Ag_{14}$ possesses no more floating atom but a central atom plus its surrounding 13 atoms. This latter temperature corresponds to the position of the prepeak observed in the $C_V$ curve [81].

At temperatures up to 400 K, the $I_j$ branch of the *C*-atom is clearly well separated from the branches of other subsets of atoms. Structurally, this manifests the solid-like behavior of the *C*-atom being remained at the center of the cluster. Between 400 and 500 K, the $I_j$ value of the *C*-atom is observed to drop in a scattered manner. This thermal behavior is apparently opposite to the increase in the $I_j$ value of the $S_3$ atoms and may be traced to the contribution from the high-frequency shoulder in the $D_j(\omega)$ spectra at 450 K (see Fig. 6.7). This suggests furthermore that the structure of the cluster in this temperature range still maintains a firm "solid-state" center, even though the *C*-atom has a preference to dynamically permute its site with any of the $S_3$ atoms. The $I_j$ branches of all atoms start to mix at temperatures above 500 K and gradually lose the identities of their original subsets. The panorama of the $I_j$ branches described here is reminiscent of the premelting of the *F*-atom into the surface atoms at $T \approx 300$ K. As the temperature goes up much higher, the $I_j$ branches of all atoms completely align into one single value, exhibiting a picture of complete indistinguishability of atoms and the cluster by now is appropriately described as a liquid-like phase.

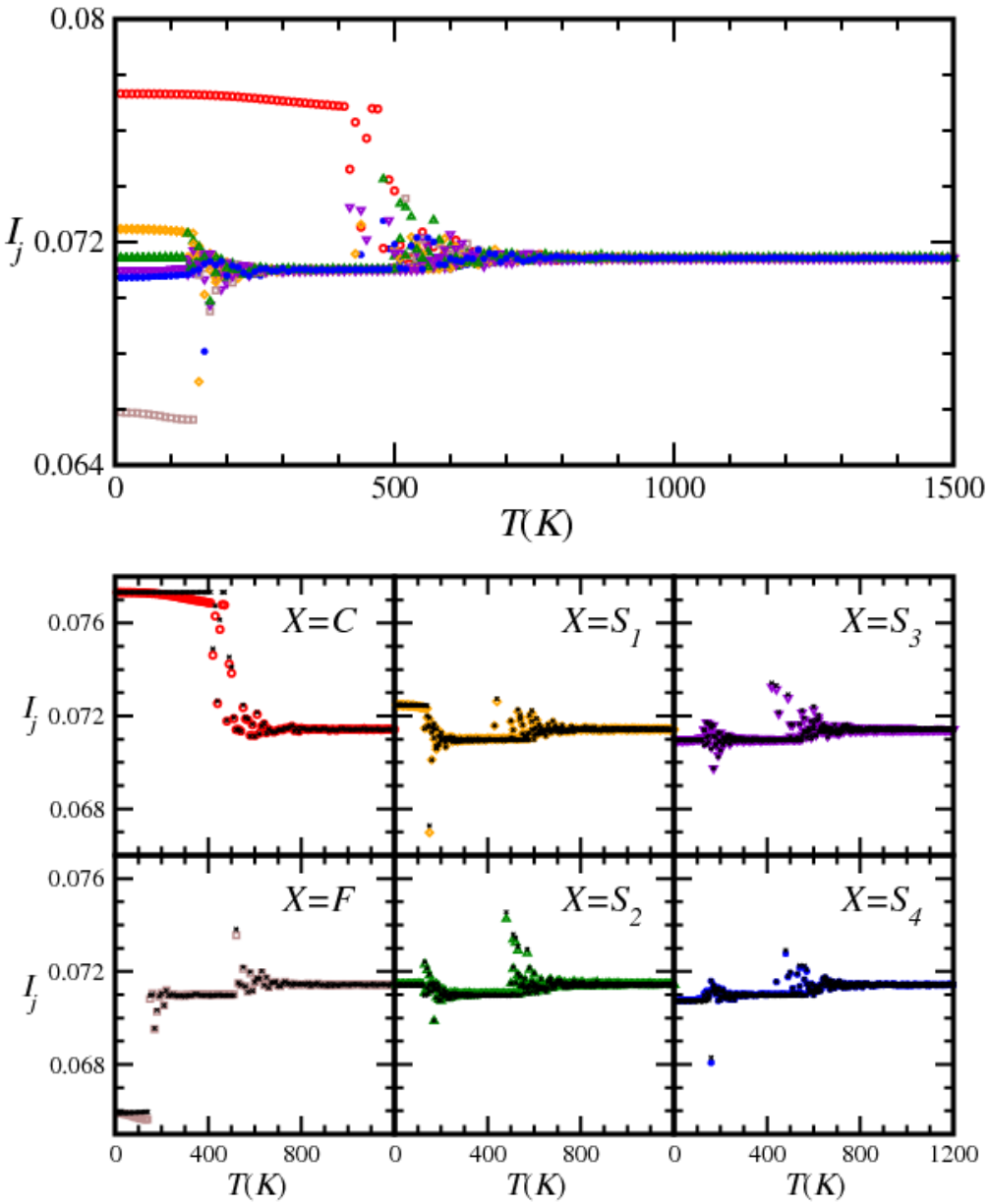


Fig. 6.8 Temperature variations of $I_j$ with atoms specified by the six subsets of $Ag_{14}$: $X=C$ (red circles), $X=F$ (brown squares), $X=S_1$ (orange diamonds), $X=S_2$ (green upper-triangles), $X=S_3$ (violet down-triangles), and $X=S_4$ (blue stars). In the upper panel, the $I_j$ value is the integral of $D_j(\omega)$ shown in Fig. 6.5 Each figure in the lower panel compares the integral $I_j$ value of a subset of atoms and the corresponding value obtained via Eq. (2.41) with the approximate rotational projection operators given in Eqs. (2.69) and (2.70) (black crosses).

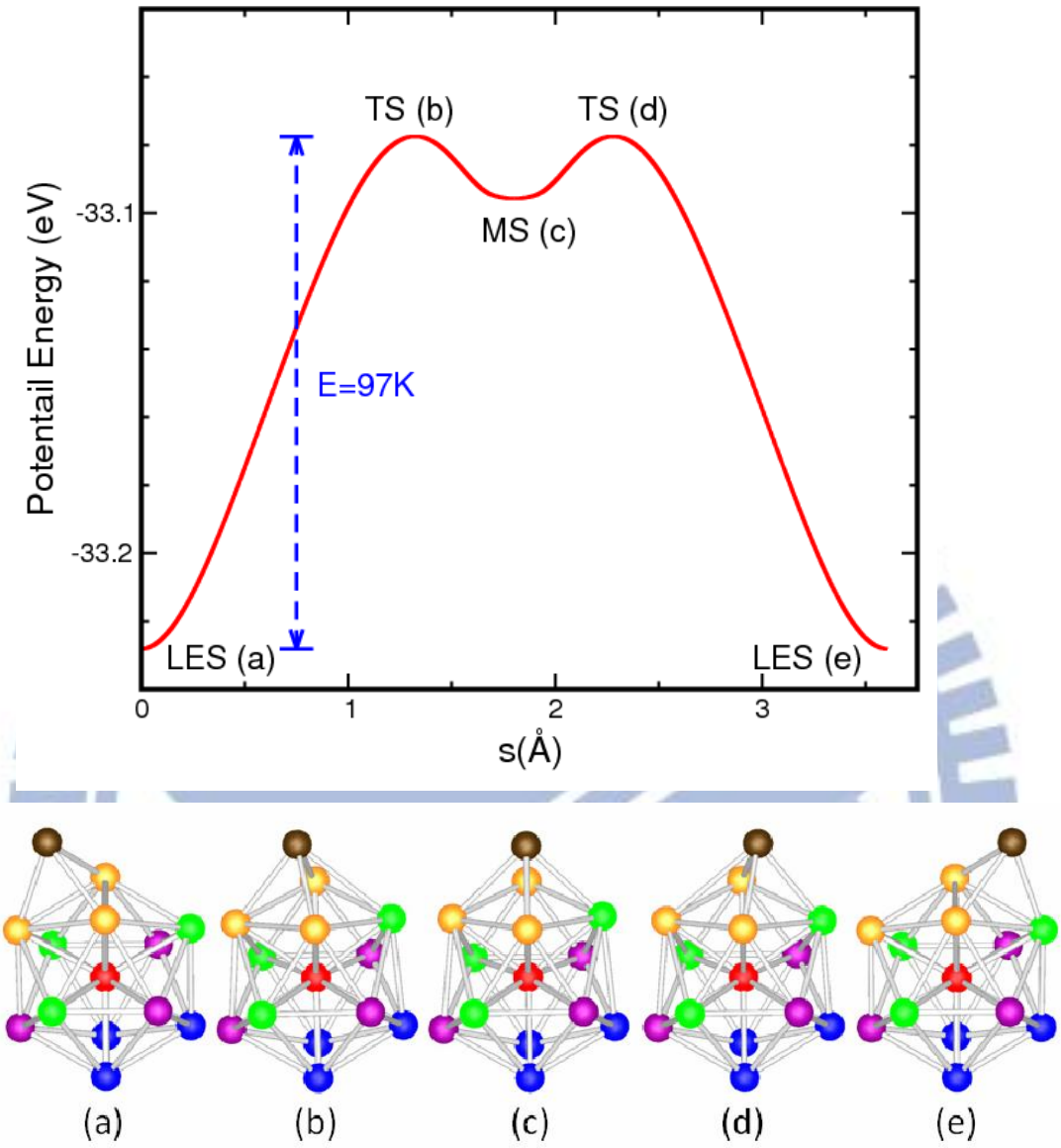


Fig. 6.9 The potential energy (red curve) as a function of the integrated path length *s* for a two-step path via two transition states, (b) and (d), and one metastable state (c) of $Ag_{14}$. The path connects to the two LESs, (a) and (e). Along the path, shown in the lower part, the *F*-atom (brown) migrates between two nearby triangular facets by crossing their common edge. In the LES (a), the *F* atom links to three $S_1$ (orange) atoms; in the LES (e), the *F* atom links to two $S_1$ atoms and one $S_2$ (green) atom. The metastable state (c) is a first excited state of the cluster [81]. The transition state (b) is found by using the OPTIM program [101- 103] from the LES (a) as the Hessian matrix possesses a unique negative eigenvalue. The path from (a) to (c) is obtained by using the steepest-decent algorithm [104] with the starting point chosen at (b) along the two opposite directions of the eigenvector corresponding to the unique negative eigenvalue. The transition state (d) and the path from (e) to (c) are obtained similarly. Note that the potential energy is calculated along the steepest-decent path [105, 106] and the potential energy barrier from (a) to (b) is estimated to be 97 K.

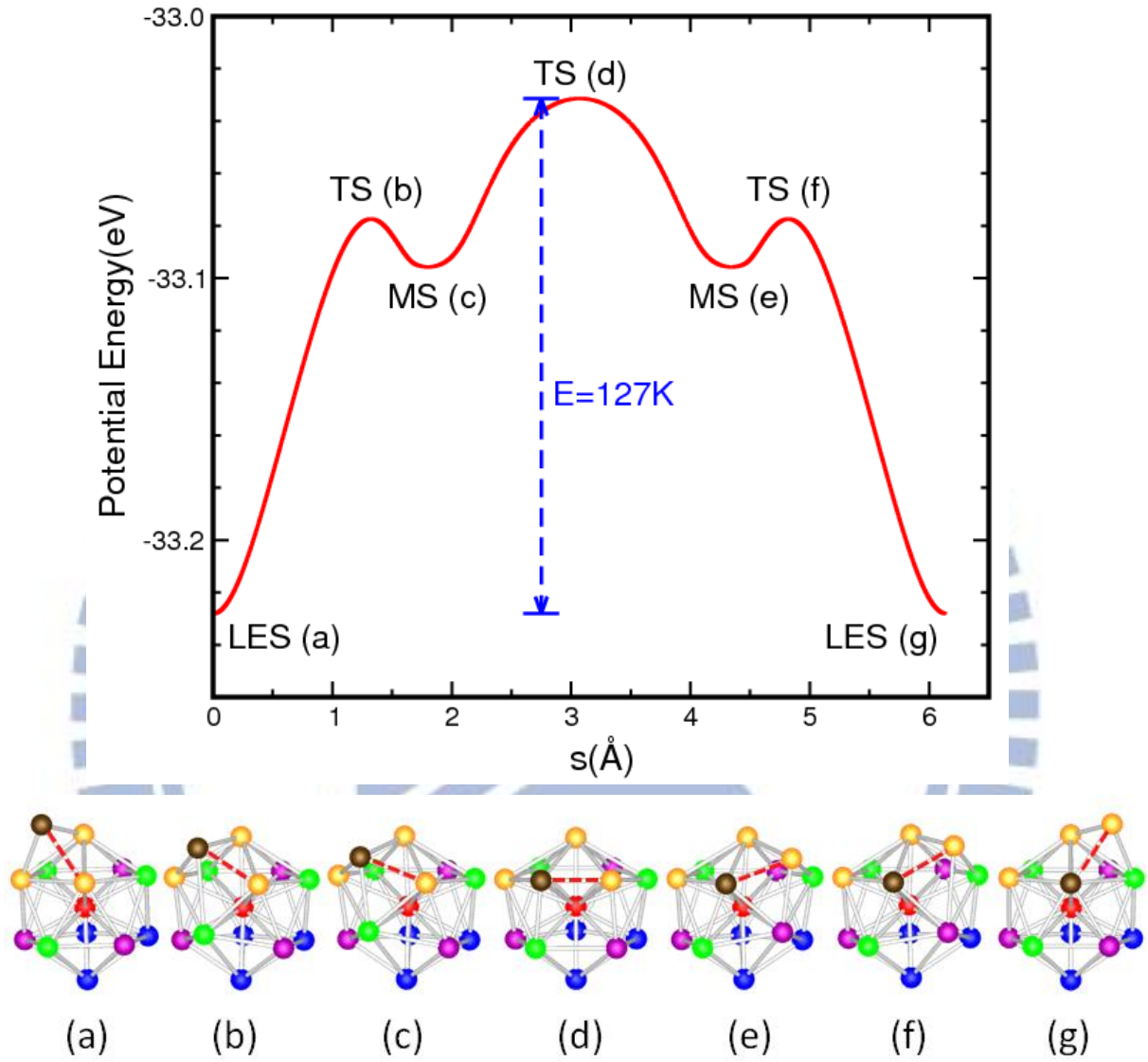


Fig. 6.10 The potential energy (red curve) as a function of the integrated path length *s* for a three-step path via three transition states, (b), (d), and (f), and two metastable states, (c) and (e), of $Ag_{14}$. The path connects to the two LESs, (a) and (g). The low part illustrates the path for the mechanism of site-permutation between the *F* (brown) and one of $S_1$ (orange) atoms, which are linked by a dashed red line. In the LES (a), the *F* atom is the one floating outside the deformed icosahedron, whereas in the LES (g), the floating atom has been replaced by one of $S_1$ atoms. The (c) and (e) are the two first excited states of the cluster [81]. The three transition states and the path are obtained by the method as described in Fig. 8. Similar as in Fig. 8, the potential energy is calculated along the path and the potential energy barrier from (a) to (d) is estimated to be 127 K.

## 6.5 Order parameter $\tau(T)$ for melting of $Ag_{14}$ prepeak

We show in Fig. 6.11, the order parameters $\tau(T)$ calculated with either the $I_j$ values according to Eqs.(2.62)- (2.64) or the average values of the rotational projection by employing the purely rotational eigenvectors according to Eqs. (2.65) (2.66) (2.71) and (2.72). A glimpse of Fig. 6.11 shows that the $\tau(T)$ obtained by the two methods are strikingly similar except in the region between 200 and 500 K. The correspondence between $\tau(T)$ and $C_V$ [81] can be made by comparing them side by side.

Below 150 K, $\tau(T)$ is almost one, reflecting the small amplitude vibrations of atoms around the LES and these vibrations result in a mild increase in $C_V$ with temperature. It is interesting to see that $\tau(T)$ undergoes a sudden decline between 150 and 200 K, which may be interpreted as the migration and relocation of the *F*-atom near the surface of the deformed icosahedrons [46, 81] or site-permutations between the *F* atom and the surface atoms. The significant jump of $\tau(T)$ from 1 to 0.70 corresponds to the first sharp rise in $C_V$ at 150 K before the prepeak. Following this jump, the behavior of $\tau(T)$ in the temperature window 200–450 K has a small decrease by the method with the integral $I_j$ values, which contrasts to the constant values by the purely rotational eigenvectors. Physically, this temperature region marks the dissolution of the *F*-atom into the surface of the deformed icosahedron. The almost flat region of $\tau(T)$ thus has intimate relevance to the prepeak structure of $C_V$, with the middle of the flat region roughly matching the prepeak position of $C_V$ at $T \approx 300$ K.

The behaviors of $\tau(T)$ and $C_V$ beyond the temperature region mentioned above are rather similar to those for $Ag_{17}Cu_2$. First, we see a sharp drop in the $\tau(T)$ of $Ag_{14}$ around 500 K, at which temperature a second sharp rise in $C_V$ occurs. As the temperature is raised above 500 K, we see another drastic change of $\tau(T)$. A conspicuous characteristic of $\tau(T)$ is its abrupt drop and approaches asymptotically to a small value (see the inset in Fig. 6.11) at a temperature close to 920 K. The latter is strikingly close to the position of the main peak of $C_V$. This temperature range thus describes the mixing process of the central atom with its surrounding atoms, where the cluster is driven thermally into configurations of higher energy excited states. The behavior of the sudden decline in $\tau(T)$ of $Ag_{14}$ is also observed in $Ag_{17}Cu_2$. Both clusters point to a transition during which the solid-like and liquid-like isomers coexist. At temperatures above $T_m$, the finite size of the cluster yields a small non-zero constant $\tau(T)$ value, which suggests no further distinction among the atoms in the cluster; correspondingly, $C_V$ decays with increasing temperature. The cluster at this moment behaves more liquid-like.

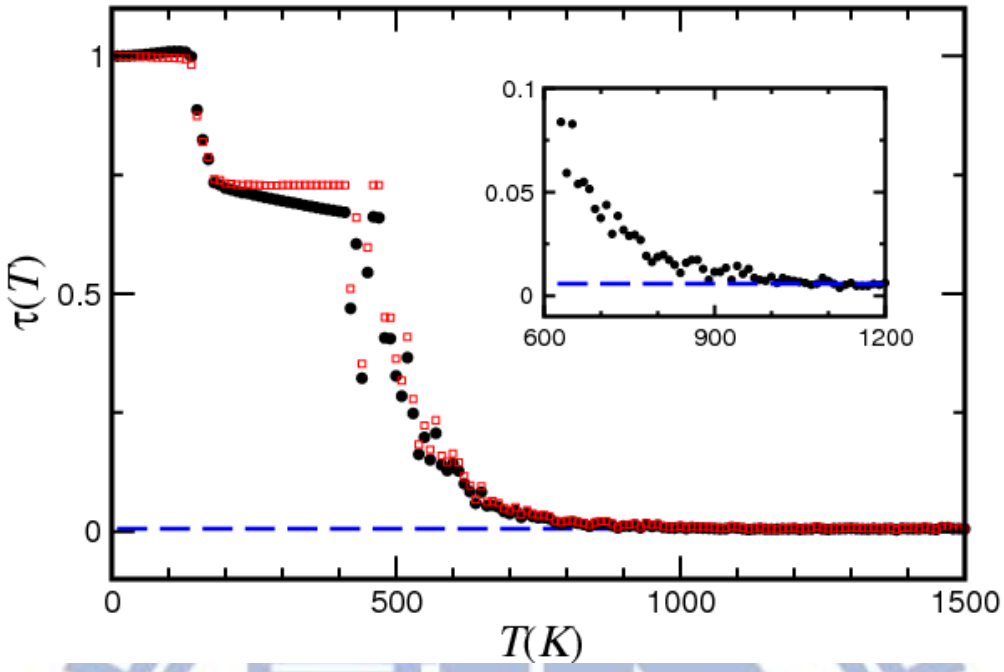


Fig. 6.11 Temperature variation of order parameter $\tau(T)$ for $Ag_{14}$ cluster. The filled circles are calculated via Eqs. (2.62) and (2.63) with the integral $I_j$ values shown in Fig. 6.8 and the open squares are obtained via Eqs. (2.65) and (2.66) with the approximate rotational projections given in Eqs. (2.71) and (2.72). The dashed line indicates the values of $\tau(T)$ above 1000 K. The inset enlarges $\tau(T)$ function for better visualization of the thermal behavior of $\tau(T)$ near 900 K.

## 6.6 Summary

In recapitulation, I have demonstrated with concrete illustrations for the results of $Ag_{14}$ in this Chapter and for $Ag_{17}Cu_2$ in the preceding chapter that $\tau(T)$ is an insightful order parameter capable of describing consistently the phenomenon of cluster melting and its intimate relevance to the thermal variation of $C_V$ even for clusters containing a prepeak and a main peak.

The mechanism associated with the prepeak in the $C_V$ curve of $Ag_{14}$ cluster can be interpreted as the melting between the adatom and the surface atoms of the deformed icosahedron in the cluster; while the mechanism associated with the main peak in the $C_V$ curve can be referred as the melting of all atoms in the cluster together. My arguments for the melting mechanism have been demonstrated from the viewpoint of potential energy landscape. This interpretation for the melting mechanism of a cluster is also consistent with the temperature variations of the $I_j$ values for the subsets of atoms classified by the symmetry characters of the LES of the cluster. Thus, this is why the order parameter $\tau(T)$ deduced from the standard deviation of the $I_j$ values gives a well prediction about the positions of the prepeak and the main peak in $C_V$ curve.

# Chapter 7
# Diffusion Phenomenon by INM Theory

In this Chapter, I introduce another approach to evaluate the diffusion coefficient of cluster at finite temperatures, besides by investigating the long-time behavior of VAF $C(t)$ given in Eq.(2.46). As a result of the difference in diffusion between clusters in the solid-like and liquid-like phases, this approach also provides a method to investigate the melting phenomenon of clusters. The diffusion coefficient of a bulk system is related to the zero-frequency value of the power spectrum $\Omega(\omega)$ defined similarly as Eq. (2.47). This result can be derived from the Green-Kubo formula [107] and the self-diffusion constant $D$ can be calculated via a time integral of $C(t)$. That is,

$$D = (\frac{k_B T}{m}) \int_0^\infty C(t) dt \, . \tag{7.1}$$

The time integral in Eq.(7.1) is associated with the Fourier cosine transform of $C(t)$ at $\omega=0$ which is explicitly proportional to the diffusion constant $D$. Eq. (7.1) works well for bulk systems but may not be so for finite-size systems, such as clusters. Since the $C(t)$ of a cluster possesses a small incessant oscillation in the long-time scale, one is unable to specifically determine the diffusion coefficient of a cluster via Eq. (7.1).

By a subsequent procedure, which is an extension of some earlier work by Zwanzig [108], Madan, Keyes and Seeley [63] proposed an intuitive way to evaluate the diffusion coefficient of a cluster with the stable and unstable INMs. They assumed that the VAF of a cluster is contributed from both a set of stable, relatively local vibrations of frequency $\omega$ and the occasional excursions, with a characteristic frequency $\omega_\nu$, that take the cluster away from its stable configuration. If the stable vibrational INM DOS, $D_{vib}^{(s)}(\omega)$, governs the stable vibrations, then we can write approximately that

$$C(t) = \int_0^\infty D_{Vib}^{(s)}(\omega) \cos(\omega t) \mathrm{sech}(\omega_\nu t) d\omega \tag{7.2}$$

The reason implied in this particular form is that $C(t)$ is required to be an even function of time by Newton's laws, whereas the existence of an excursion with frequency $\omega_\nu$ means that the envelope of the simple harmonic $\cos(\omega t)$ behavior should decay asymptotically as $\exp(-\omega_\nu t)$. The hyperbolic

secant factor in Eq.(7.2) allows both criteria to be satisfied. By substituting Eq.(7.2) into Eq. (7.1), a workable expression for *D* is yielded as

$$D = \left(\frac{k_B T}{m}\right)\int_0^\infty d\omega D_{Vib}^{(s)}(\omega)\left(\frac{\pi}{2\omega_\nu}\right)\mathrm{sech}\left(\frac{\pi\omega}{2\omega_\nu}\right) \tag{7.3}$$

On the other hand, a relation between the diffusion constant and the characteristic frequency $\omega_\nu$ can be found by exploiting an analogy with the calculations of chemical reaction rates in liquids, Madan, Keyes, and Seeley have derived an expression giving the excursion frequency self-consistently in terms of the diffusion constant,

$$\omega_\nu = (\frac{n}{2\pi})(\frac{m}{k_B T}) f_u \langle\omega\rangle_s \langle\omega\rangle_u D \tag{7.4}$$

where $\langle\omega\rangle_s$ is the average frequency of the stable-mode vibrations and $f_\mu$ and $\langle\omega\rangle_u$ are, respectively, the fraction and the average magnitude of the unstable-mode vibrational frequencies. The quantity *n* represents the number of stable configuration states which are, in some sense, neighbors of a given stable state, that is, it reflects the number of states into which the system can hop from its present state.

There are three undetermined coefficients, $\omega_\nu$, *D* and *n*, in Eqs. (7.3) and (7.4). Besides the two equations, one more equation is required for solving the three unknowns. A clue also proposed by Madan, Keyes, and Seeley is that at high temperatures it turns out to be possible to estimate the excursion frequency $\omega_\nu$ directly from the instantaneous normal mode data. Once a value of $n$ is obtained in such a way, one can solve Eq. (7.3) and (7.4) for simultaneously determining the estimated $\omega_\nu$ and diffusion coefficient *D* at high temperatures. Suggested by Madan, *et al.*, with the same value of $n$ for all temperatures, the diffusion constant can be computed for lower temperatures by continuing to solve Eqs. (7.3) and (7.4) simultaneously.

To estimate *n* in detail in the INM theory, the VAF implied by the instantaneous normal mode spectrum is exact at short times. In the Taylor series expansion of *C*(*t*) given in Eq.(2.52), which is obtained by expanding $\cos(\omega t)$ up to the second order in *t*, the first few terms in the expansion are given as

$$C(t) = 1 - A_2 t^2 + A_4 t^4 + \cdots \tag{7.5}$$

with

$$A_2 = \left(\frac{1}{2!}\right)(3N-6)^{-1}\left\langle\sum_{\alpha=1}^{3N-6}\omega_\alpha^2\right\rangle \tag{7.6}$$

and

$$A_4 = \left(\frac{1}{4!}\right)(3N-6)^{-1}\left\langle\sum_{\alpha=1}^{3N-6}\omega_\alpha^4\right\rangle \tag{7.7}$$

where the summations are over all real and imaginary modes for each system configuration with the

translations and rotations being subtracted out and the average is over the equilibrium distribution of system configurations. Now, I can rewrite this correlation function so that it remains exact through the same order in time by saying

$$C(t) = \cos(at)sech(bt) \tag{7.8}$$

I express the constant $a$ and $b$ in terms of $A_2$ and $A_4$ by comparing the expansion coefficients with Eq.(7.5). It suggests that, at least in an Einstein-like approximation, the constant $b$ is precisely the asymptotic decay frequency $\omega_v$. In other words, it leads us to the high temperature estimate

$$\omega_v = \left[\frac{3A_4}{A_2} - \frac{A_2}{2}\right]^{\frac{1}{2}} \tag{7.9}$$

In principal, this equation could be used to help for evaluating the diffusion constant $D$ at all temperatures, but it is only at relatively highest temperatures that it is really plausible. It is after all, only at the highest temperatures that the asymptotic relaxation time $1/\omega_v$ will be short enough to be given so directly by the time correlation function determined by instantaneous normal modes. Associated with the diffusion coefficient evaluated from Eq. (7.3), I can obtain $n$ in high temperatures, so that the diffusion coefficient from low to high temperature can be solved from Eq. (7.3) and Eq. (7.4) with the same $n$ evaluated from high temperature.

The abrupt change in the diffusion coefficient that is evaluated in terms of the theory proposed by Madan, Keyes, and Seeley can predict the solidlike-liquidlike phase transition for the liquid-like phase exhibits much larger diffusion coefficient than the solid-like phase and the results for $Ag_{14}$ cluster is shown Fig. 7.1. Indicated by the figure, the diffusion coefficient is zero until the temperature increase above 870K. Roughly, this temperature is referred as the melting temperature from diffusion coefficient, although it is not precisely the melting temperature at 920K inferred form $C_V$ curve in Fig. 6.1. In addition, one is unable to find any diffusion information related to the prepeak in the $C_V$ curve. In conclusions, this method is not so good to predict the melting temperature of the cluster systems.

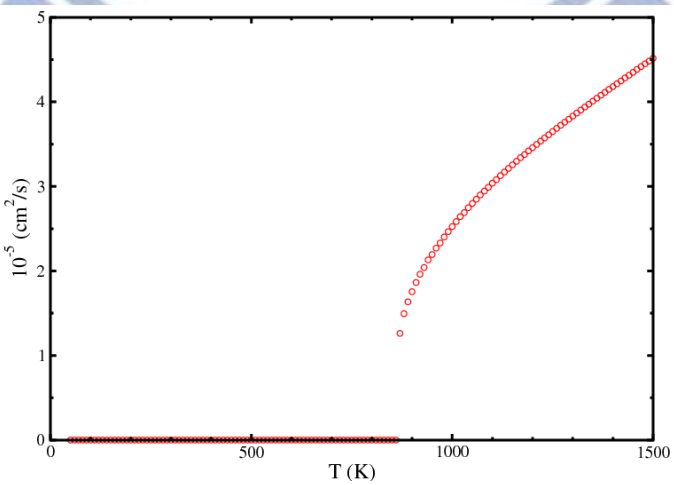


Fig. 7.1 Diffusion coefficient evaluated in terms of the theory proposed by Madan, Keyes, and Seeley. The diffusion phenomenon roughly occurs at temperatures above 870K.

# Chapter 8
# Conclusions

The isothermal Brownian-type MD simulations with the Gupta potentials of $Ag_{14}$ and $Ag_{17}Cu_2$ clusters have been carried out from 0K (LES) to 1500 K, whose specific heat $C_V$ exhibits a single main peak or a main peak with a prepeak at a lower temperature. Methodologically, I used the INM analysis, which has been developed for clusters in general. In this thesis, I proposed a new order parameter $\tau(T)$, which is defined as the normalized standard deviation of the integral $I_j$ of the INM vibrational DOSs associated with all atoms in a cluster.

In Chapter 5 and Chapter 6, I gave, respectively, a general description about melting scenario of $Ag_{17}Cu_2$ and $Ag_{14}$ clusters via the temperature variation of the $I_j$ values for all atoms in a cluster. For simplicity, we discuss here only the case for pure clusters. At the LES, the $I_j$ values of atoms may be classified according to the point group character of the cluster structure. The group character of the lowest energy structure is well identified so that the $I_j$ values of these atoms may be split into a number of branches each of which corresponds to a subgroup of the structure. At low temperatures, the cluster structures are near the LES and hence the $I_j$ values are almost unchanged. As the temperature is increased into an intermediate range, the atoms in the cluster may have undertaken dynamical site permutations or the cluster is thermally driven into higher excited states. In either case, the group characters of cluster structures are different from that of the LES. In this temperature range, nevertheless, one may still recognize the split of the $I_j$ values into branches. These $I_j$ values start in fact to mix after a further rise in temperature and gradually they lose their original discernible branches as the temperature is raised higher and higher. Eventually, the $I_j$ branches completely disappear and merge indistinguishably at certain temperature, say $T_m$, indicating that the positions of atoms in the cluster are completely dislocated. The $T_m$ is naturally referred to as the melting temperature of the cluster. At $T > T_m$, the cluster can thus be looked upon as in a liquid-like state.

I address further the $\tau(T)$ defined in the INM approach. The integral $I_j$ value of a pure cluster is found to be related to the rotational projection of the *j*-th atom in the cluster, where the projection consists of a sum of three ratios with each ratio measuring the ensemble-averaged contribution of the

atom in the moment of inertia of the whole cluster calculated with respect to one of its principal axes. Thus, the order parameter $\tau(T)$ can be defined in a scheme associated with the vibrational motions of individual atoms or the rotational motion of the whole cluster assuming to be rigid. I demonstrate that almost equivalent results were obtained by the two definitions of $\tau(T)$. Physically, the description of the melting for both $Ag_{14}$ and $Ag_{17}Cu_2$ by $\tau(T)$ agrees very well with that inferred from $C_V$, even with a prepeak in the $C_V$ curve. Our results strengthen our belief that $\tau(T)$ is an order parameter that sheds considerable light on cluster melting and provides a means to ravel the microscopic dynamics of clusters from the point of view of potential energy landscape.

The reason why the order parameter $\tau(T)$ works so well is not fortuitous but stems from the fact that the $I_j$ values are fundamentally related to the symmetry of the cluster structures at different temperatures. The split of $I_j$ values at lower temperatures into several branches follows the symmetry of the LES of a cluster according to the group theory. At high temperatures, the $I_j$ values merge into one since the cluster configurations stray far from its LES resulting in the loss of symmetry. It is well known in condensed matter physics that the phase transition in bulk systems from a crystal to a liquid is described by the concept of broken symmetry [82]. The results of the $I_j$ values presented in this thesis imply that the broken symmetry is also a useful concept for understanding the melting of clusters. The main difference in the melting transition between clusters and bulk systems lies in the extent of the symmetry breaking: For bulk systems, the broken symmetry is associated with an infinite number of degrees of freedom so that the transition is abrupt at a melting temperature, whereas in clusters the symmetry broken is associated with a finite number of degrees of freedom so that the transition is gradual and, therefore, occurring within a temperature interval. The quantitative estimate for the broken symmetry during cluster melting would have to refer to a similar discussion of examining the distance of a distorted molecule from any chosen element of symmetry [109].

By following the concept of broken symmetry, it is worth re-thinking of why the $C_V$ of $Ag_{14}$ has an additional prepeak, whereas none in $Ag_{17}Cu_2$. Based on our studies so far, I conjecture that the plausible reason is probably related to the difference in the LESs of the two clusters: The LES structure, $Ag_{17}Cu_2$, which has the $D_{5h}$ axial point group, possesses a highly symmetry center close to, but not exactly, an inversion center, while that of $Ag_{14}$, with the $C_{3v}$ axial point group for a floating atom outside a deformed icosahedron, possesses only the rotational symmetry about its principal axis. According to our findings, the prepeak of $C_V$ seen in $Ag_{14}$ is associated with the dissolution of the floating atom into the surface of the deformed icosahedron so that the structures of $Ag_{14}$ change to ones with a stabilized central atom which is surrounded by the rest of the atoms. Accordingly, the cluster $Ag_{14}$ melting at higher temperatures is associated with the symmetry breaking as the structural center is being destroyed by the thermal motion of atoms, similar to that for $Ag_{17}Cu_2$, corresponding to the main peak in $C_V$ curve. As far as the cluster melting is concerned, it would be intriguing to examine melting transition with the concept of broken symmetry especially between clusters whose LESs have different structural symmetries. On the other hand, an INM investigation for the temperature variation of the imaginary-part contribution is another interesting issue for future works.

# Appendix

## A.1 Derivation for purely rotational eigenvectors of clusters

For a cluster of *n* atoms with mass $m_j$ ($j = 1, \ldots, n$), the elements of Hessian matrices are given in Eq. (11.5). Derived from the conservation law for total translational momentum of the cluster, the three translational eigenvectors of the $3n \times 3n$ Hessian matrices are given as the following:

$$\mathbf{e}_j^{T_x} = \sqrt{\frac{m_j}{M}}\begin{bmatrix}1\\0\\0\end{bmatrix},\ \mathbf{e}_j^{T_y} = \sqrt{\frac{m_j}{M}}\begin{bmatrix}0\\1\\0\end{bmatrix},\ \mathbf{e}_j^{T_z} = \sqrt{\frac{m_j}{M}}\begin{bmatrix}0\\0\\1\end{bmatrix} \tag{9.1}$$

where *M* is the total mass of the cluster. One can easily examine that the eigenvalues of the three translational eigenvectors are indeed zero. In this Appendix, I will prove that the three purely rotational eigenvectors of a cluster can be derived from the conservation law for total angular momentum of the cluster.

Let's consider the total angular momentum of a cluster of *n* atoms as

$$\boldsymbol{L} = \sum_i \boldsymbol{L}_i = \sum_i \boldsymbol{r}_i \times \boldsymbol{p}_i \tag{9.2}$$

where $\boldsymbol{r}_i$ and $\boldsymbol{p}_i$ are the position and linear momentum of particle *i*, respectively. Without externally applied forces and torques, the dynamics of the system is only influenced by the internal forces between particles so that its total angular momentum is conserved. Therefore, the derivative of $\boldsymbol{L}$ with respect to time is zero. So, we have

$$\dot{\boldsymbol{L}} = \sum_i \boldsymbol{r}_i \times \boldsymbol{F}_i = -\sum_i \boldsymbol{r}_i \times \frac{\partial V}{\partial \boldsymbol{r}_i} = 0 \tag{9.3}$$

where the force on a particle is the negative of the gradient of the total potential energy $\boldsymbol{V}$ of the cluster with respect to the particle position. The equation for the $\mu$ component of $\boldsymbol{L}$ can be written as

$$\dot{L}_\mu = -\sum_i \epsilon_{\mu\upsilon\eta} r_{i\upsilon} \frac{\partial V}{\partial r_{i\eta}} = 0 \tag{9.4}$$

where the three-dimensional Levi-Civita symbol $\epsilon_{\mu\nu\eta}$ ($\mu, \nu, \eta = x, y, z$) has been used and a summation for a subscript appearing twice on one side of an equation is implied. By differentiating this equation with respect to the 3-dimensinal real space coordinates $r_{k\xi}$, with $k = 1, \ldots n$, and $\xi = x, y, z$, one may obtain

$$\frac{\partial}{\partial r_{k\xi}}\left(\sum_i \epsilon_{\mu\upsilon\eta} r_{i\upsilon} \frac{\partial V}{\partial r_{i\eta}}\right) = \epsilon_{\mu\xi\eta} \frac{\partial V}{\partial r_{k\eta}} + \sum_i \epsilon_{\mu\upsilon\eta} r_{i\upsilon} \frac{\partial^2 V}{\partial r_{k\xi} \partial r_{i\eta}} = 0 \tag{9.5}$$

Consider the cluster configuration at a local minimum of *V*, which implies that $\partial V/\partial \boldsymbol{r}_k = 0$ and the first term in Eq. (9.5) is zero. So, we have

$$\sum_i \epsilon_{\mu\nu\eta} r_{i\upsilon} \frac{\partial^2 V}{\partial r_{k\xi} \partial r_{i\eta}} = 0 \tag{9.6}$$

Multiply and divide with the same factor $\sqrt{m_i m_k}$ and relate each term in the summation to the elements of the Hessian matrix. Then, the equation becomes

$$\sum_i \sqrt{m_i m_k}\ \epsilon_{\mu\nu\eta} r_{i\upsilon} \frac{1}{\sqrt{m_i m_k}} \frac{\partial^2 V}{\partial r_{i\eta} \partial r_{k\xi}} = \sum_{i\eta} H_{k\xi,i\eta} \left\{ \sqrt{m_i} \sum_\upsilon \epsilon_{\mu\nu\eta} r_{i\upsilon} \right\} = 0 \tag{9.7}$$

By comparing this equation with the eigenvalue equation of a matrix, one can find that

$$e_{i\eta}^{R_\sigma} = A_\sigma \sqrt{m_i} \sum_\nu \epsilon_{\sigma\nu\eta} r_{i\nu}, \quad with\ \sigma = x,\ y,\ z \tag{9.8}$$

are three eigenvectors of the Hessian matrix with zero eigenvalue and $A_\sigma$ is a factor for normalization. Therefore, by deriving from the conservation law for total angular momentum, we obtain three rotational eigenvectors with zero eigenvalue of the Hessian matrix and the three rotational eigenmodes are denoted as $R_x$, $R_y$, and $R_z$. Besides a normalization factor, the three rotational eigenvectors can be expressed explicitly as

$$e_{i\eta}^{Rx} = A_x \sqrt{m_i} \begin{bmatrix} 0 \\ -r_{iz} \\ r_{iy} \end{bmatrix},\ e_{i\eta}^{Ry} = A_y \sqrt{m_i} \begin{bmatrix} r_{iz} \\ 0 \\ -r_{ix} \end{bmatrix},\ e_{i\eta}^{Rz} = A_z \sqrt{m_i} \begin{bmatrix} -r_{iy} \\ r_{ix} \\ 0 \end{bmatrix} \tag{9.9}$$

One should notice that we have not yet checked the orthogonality between the eigenvectors of the translational and rotational modes. Next, I will prove that in order to keep the orthogonality between the rotational and translational modes, the origin for describing the cluster configuration should be chosen at the center-of-mass of the cluster and select the principal axes of the cluster configuration to be the rotational axis for constructing the rotational modes. After this proof, we will obtain six orthogonal bases for describing the subspace related to the translational and rotational modes of the cluster.

By making a cluster configuration a translational shift in three-dimensional space, the Hessian matrix of the cluster configuration does not change, due to the same cluster structure before and after the translational shift. But, according to Eq. (9.8), the translational shift of the atomic positions in the cluster will result in different rotational eigenvectors. This implies that we may find the rotational eigenvectors as many as possible from Eq. (9.8) for cluster configurations with different translational displacements from the original cluster configuration. Accordingly, a translational displacement of the whole cluster is controlled by a set of three parameters $d_x, d_y, d_z$ and corresponding to this displacement the rotational eigenvectors of the Hessian matrix can be written as

$$\mathbf{e}_{i\eta}^{R_x} = A_x'\sqrt{m_i}\begin{bmatrix} 0 \\ -r_{iz}-d_z \\ r_{iy}+d_y \end{bmatrix},\ \mathbf{e}_{i\eta}^{R_y} = A_y'\sqrt{m_i}\begin{bmatrix} r_{iz}+d_z \\ 0 \\ -r_{iy}-d_y \end{bmatrix},\ \mathbf{e}_{i\eta}^{R_z} = A_z'\sqrt{m_i}\begin{bmatrix} -r_{iy}-d_y \\ r_{ix}+d_x \\ 0 \end{bmatrix} \quad (9.10)$$

which can be proved to satisfy the eigenvalue equation of the same Hessian matrix with zero eigenvalue in the following

$$\begin{aligned} &\sum_{i\eta} H_{k\xi,i\eta}\sqrt{m_i}\left(\sum_{\nu}\epsilon_{\mu\upsilon\eta}\left(r_{i\nu}+d_\nu\right)\right) \\ &=\sum_{i\eta} H_{k\xi,i\eta}\sqrt{m_i}\left(\sum_{\nu}\epsilon_{\mu\nu\eta}r_{i\nu}\right)+\sum_{\nu\eta}\epsilon_{\mu\nu\eta}d_\nu\sum_i\sqrt{m_i}H_{k\xi,i\eta}=0 \end{aligned} \quad (9.11)$$

where the second term equals zero due to the sum rule on the Hessian elements in the same row or the same column. Thus, for the shifted cluster configuration, the translational eigenvectors are still given by Eq. (9.1) but the rotational eigenvectors are given as Eq. (9.12) with a different normalization constant $A'$.

$$\begin{cases} e_{i\eta}^{R_\mu} = A_\mu'\sqrt{m_i}\left(\sum_{\nu}\epsilon_{\mu\nu\eta}\left(r_{i\nu}+d_\nu\right)\right) & \text{rotational eigenvectors} \\ e_{jk}^{T_\nu} = \sqrt{\dfrac{m_j}{M}}\delta_{\nu k} & \text{translational eigenvectors} \end{cases} \quad (9.13)$$

In the following, I consider the orthogonality between the rotational and translational eigenvectors of a shifted cluster configuration. The orthogonality requires $\sum_j \mathrm{e}_{jk}^{R_\mu}\cdot\mathrm{e}_{jk}^{T_\nu}=0$ for all possible pairs of $R_\mu$ and $T_\nu$. The orthogonality equations are given explicitly as

$$\sum_j A_\mu'\sqrt{m_j}\left(\epsilon_{\mu lk}\left(r_{jl}+d_l\right)\right)\cdot\sqrt{\frac{m_j}{M}}\delta_{\nu k}=\sum_{jl}A_\mu'\frac{m_j}{\sqrt{M}}\left(r_{jl}+d_l\right)\epsilon_{\mu l\nu}=0 \quad (9.14)$$

This result yields

$$\sum_j m_j\left(r_{jl}+d_l\right)\epsilon_{\mu l\upsilon}=0 \quad (9.15)$$

For the three cases with $\mu=\nu$, the equation is automatically satisfied due to the properties of the Levi-Civita symbols. For the other six possible cases with $\mu\neq\nu$, for each $l$, we have

$$\begin{cases} \sum_j m_j\left(r_{jx}+d_x\right)=0 & \text{for } \ell=x \\ \sum_j m_j\left(r_{jy}+d_y\right)=0 & \text{for } \ell=y \\ \sum_j m_j\left(r_{jz}+d_z\right)=0 & \text{for } \ell=z \end{cases} \quad (9.16)$$

These equations are inferred that

$$\begin{cases} d_x = -\sum_j m_j r_{jy} \Big/ \sum_j m_j \\ d_y = -\sum_j m_j r_{jx} \Big/ \sum_j m_j \\ d_z = -\sum_j m_j r_{jz} \Big/ \sum_j m_j \end{cases} \tag{9.17}$$

This result indicates that the three parameters $d_x$, $d_y$ and $d_z$ are nothing but the *x*, *y*, and *z* coordinates of the center-of-mass of the original cluster configuration, respectively. Therefore, if the origin of the coordinate system is chosen at the center-of-mass of the cluster, the set of the three rotational eigenvectors is orthogonal to the three translational eigenvectors. Therefore, the corresponding rotational eigenvectors in this new coordinate system should be changed as

$$e_{i\eta}^{R_{x'}} = A\sqrt{m_i}\begin{bmatrix} 0 \\ -r'_{iz} \\ r'_{iy} \end{bmatrix},\ e_{i\eta}^{R_{y'}} = A\sqrt{m_i}\begin{bmatrix} r'_{iz} \\ 0 \\ -r'_{ix} \end{bmatrix},\ e_{i\eta}^{R_{z'}} = A\sqrt{m_i}\begin{bmatrix} -r'_{iy} \\ r'_{ix} \\ 0 \end{bmatrix} \tag{9.18}$$

where the atomic coordinates $r'_{i\eta}$ are relative to the center-of-mass of the cluster configuration.

So far, we have not yet checked the orthogonality between the rotational eigenvectors themselves given in Eq. (9.18). Actually, any linear combinations of the three rotational eigenvectors are also another eigenvectors with zero eigenvalue. That is,

$$e_{i\eta}^{R_\mu} = \sum_\gamma C_{\mu\gamma}\sqrt{m_i}\sum_\nu \epsilon_{\gamma\nu\eta} r'_{i\nu} \tag{9.19}$$

where $C_{\mu\gamma}$ are the coefficients of the linear combination and are arbitrarily chosen. Suppose that the coefficients $C_{\mu\gamma}$ are chosen to be the elements of an orthogonal matrix that describe a rotation of the coordinate axes in three-dimensional space. That is,

$$\boldsymbol{r}'' = \boldsymbol{C}\boldsymbol{r}' \tag{9.20}$$

Then, the inner product of any two of the rotational eigenvectors is written as

$$\sum_i e_{i\omega}^{R_\mu} \cdot e_{i\omega}^{R_k} = \sum_i m_i \left(\delta_{\mu k} r''_{i\nu} r''_{i\nu} - r''_{ik} r''_{i\mu}\right) \tag{9.21}$$

The inner products between any two of three rotational eigenvector and including their self-products in the rotated coordinated systems can be written in a matrix form, which is expressed as

$$\begin{pmatrix} \sum_i e_{i\omega}^{R_{x'}} \cdot e_{i\omega}^{R_{x'}} & \sum_i e_{i\omega}^{R_{x'}} \cdot e_{i\omega}^{R_{y'}} & \sum_i e_{i\omega}^{R_{x'}} \cdot e_{i\omega}^{R_{z'}} \\ \sum_i e_{i\omega}^{R_{y'}} \cdot e_{i\omega}^{R_{x'}} & \sum_i e_{i\omega}^{R_{y'}} \cdot e_{i\omega}^{R_{y'}} & \sum_i e_{i\omega}^{R_{y'}} \cdot e_{i\omega}^{R_{z'}} \\ \sum_i e_{i\omega}^{R_{z'}} \cdot e_{i\omega}^{R_{x'}} & \sum_i e_{i\omega}^{R_{z'}} \cdot e_{i\omega}^{R_{y'}} & \sum_i e_{i\omega}^{R_{z'}} \cdot e_{i\omega}^{R_{z'}} \end{pmatrix} = \begin{pmatrix} \sum_i m_i (r''^2_{iy} + r''^2_{iz}) & -\sum_i m_i r''_{ix} r''_{iy} & -\sum_i m_i r''_{ix} r''_{iz} \\ -\sum_i m_i r''_{iy} r''_{ix} & \sum_i m_i (r''^2_{ix} + r''^2_{iz}) & -\sum_i m_i r''_{iy} r''_{iz} \\ -\sum_i m_i r''_{iz} r''_{ix} & -\sum_i m_i r''_{iz} r''_{iy} & \sum_i m_i (r''^2_{ix} + r''^2_{iy}) \end{pmatrix} \tag{9.22}$$

The matrix in Eq. (9.22) is actually the inertia tensor of the cluster configuration in the rotated coordinate system. If we choose the coordinate system with the origin at the center-of-mass of the

cluster and the coordinate axes as the three principal axes of the cluster configuration, this coordinate system defines the body frame of the cluster configuration, in which, the off-diagonal elements of the inertia tensor in Eq. (9.22) are zero and the diagonal elements give the moments of inertial of the cluster configuration about its principal axes. Therefore, in the body frame of the cluster configuration, the three rotational eigenvectors after normalization are given as

$$\mathbf{e}_i^{R_{x''}} = \sqrt{\frac{m_i}{I_x}}\begin{bmatrix} 0 \\ -r_{iz}'' \\ r_{iy}'' \end{bmatrix}, \mathbf{e}_i^{R_{y''}} = \sqrt{\frac{m_i}{I_y}}\begin{bmatrix} r_{iz}'' \\ 0 \\ -r_{ix}'' \end{bmatrix}, \mathbf{e}_i^{R_{z''}} = \sqrt{\frac{m_i}{I_z}}\begin{bmatrix} -r_{iy}'' \\ r_{ix}'' \\ 0 \end{bmatrix} \tag{9.23}$$

where $r_{ix}'', r_{iy}'', r_{iz}''$ are the coordinates of atom *i* in the body frame of the cluster configuration, and the moments of inertia $I_x,\ I_y,\ I_z$ are defined as follows,

$$\begin{aligned} I_x &= \sum_i m_i \left( r_{iy}''^2 + r_{iz}''^2 \right) \\ I_y &= \sum_i m_i \left( r_{ix}''^2 + r_{iz}''^2 \right) \\ I_z &= \sum_i m_i \left( r_{ix}''^2 + r_{iy}''^2 \right) \end{aligned} \tag{9.24}$$

# A.2 Velocity autocorrelation function in the INM approximation

In Sec. 2.1, the short-time evolution of a cluster in the mass-weighted coordinates can be obtained from the Eq. (2.21) and the inverse transformation of Eq. (2.13). This would implies that the $C(t)$ defined in Eq. (2.46) can be connected to the vibrational motions of atoms in the cluster in the context of INM. According to Eq. (2.21) and (2.13), the real-space coordinates of the *j*-th atom in the vibrational motions of a cluster can be transformed from the *3n-6* vibrational normal modes coordinates via the following formula

$$\boldsymbol{r}_j = \frac{1}{\sqrt{m_j}} \sum_{\alpha}^{3n-6} \mathbf{e}_j^{\alpha} q_{\alpha} \tag{10.1}$$

where $\alpha$ is the index for the *3n-6* vibrational INMs with eigenvectors $\mathbf{e}_j^{\alpha}$ and the normal coordinates $q_{\alpha}$.This formula implies that the corresponding velocity of the *j*-th atom can be given by the equation

$$\boldsymbol{v}_j = \frac{1}{\sqrt{m_j}} \sum_{\alpha=1}^{3n-6} \mathbf{e}_j^{\alpha} \dot{q}_{\alpha} \tag{10.2}$$

By substitute the Eq. (10.2) into Eq.(2.46), we obtain

$$C(t) \approx \frac{\left\langle \sum_j^n \frac{1}{m_j} \sum_{\alpha\beta}^{3n-6} \mathbf{e}_j^{\alpha} \cdot \mathbf{e}_j^{\beta} \dot{q}_{\alpha}(0) \dot{q}_{\beta}(t) \right\rangle}{\left\langle \sum_j^n \frac{1}{m_j} \sum_{\alpha\beta}^{3n-6} \mathbf{e}_j^{\alpha} \cdot \mathbf{e}_j^{\beta} \dot{q}_{\alpha}(0) \dot{q}_{\beta}(0) \right\rangle} \tag{10.3}$$

With the INM solutions given in Eq. (2.21) and its time derivatives, C(t) can be approximated as

$$C(t) \approx \frac{\left\langle \sum_j^n \frac{1}{m_j} \sum_{\alpha\beta}^{3n-6} \mathbf{e}_j^{\alpha} \cdot \mathbf{e}_j^{\beta} \dot{x}_{\alpha}(0) \left( \dot{x}_{\beta}(0) \cos(\omega_{\beta} t) - x_{\beta}(0) \omega_{\beta} \sin(\omega_{\beta} t) \right) \right\rangle}{\left\langle \sum_j^n \frac{1}{m_j} \sum_{\alpha\beta}^{3n-6} \mathbf{e}_j^{\alpha} \cdot \mathbf{e}_j^{\beta} \dot{x}_{\alpha}(0) \dot{x}_{\beta}(0) \right\rangle} \tag{10.4}$$

By making the ensemble average for each term in the summation first, each term associated with the indices α and β in the numerator can be decomposed into two factors as the following

$$\begin{aligned} &\left\langle \mathbf{e}_j^{\alpha} \cdot \mathbf{e}_j^{\beta} \dot{x}_{\alpha}(0) \left( \dot{x}_{\beta}(0) \cos(\omega_{\beta} t) - x_{\beta}(0) \omega_{\beta} \sin(\omega_{\beta} t) \right) \right\rangle \\ &= \left\langle \dot{x}_{\alpha}(0) \dot{x}_{\beta}(0) \right\rangle \left\langle \mathbf{e}_j^{\alpha} \cdot \mathbf{e}_j^{\beta} \cos(\omega_{\beta} t) \right\rangle - \left\langle \dot{x}_{\alpha}(0) \right\rangle \left\langle \mathbf{e}_j^{\alpha} \cdot \mathbf{e}_j^{\beta} x_{\beta}(0) \omega_{\beta} \sin(\omega_{\beta} t) \right\rangle \end{aligned} \tag{10.5}$$

where one factor is related to the ensemble average for a product of two velocities associated with different coordinates or a product of a coordinate and a velocity of another coordinate and the other factor is associated with the inner product of two INM eigenvectors. In statistical mechanics, the

coordinates and velocities of particles in a system at equilibrium are recognized as two sets of independent random variables, which are also independent in statistics with the INM eigenvector components. Because of the statistical average for the two sets of random variables, $\langle \dot{x}_\alpha(0)\rangle = 0$, the second term on the R.H.S of Eq. (2.52) will zero. Also, following the equipartition theorem, we have $\langle \dot{x}_\alpha(0)\dot{x}_\beta(0)\rangle = k_B T\delta_{\alpha\beta}$. One can do the similar thing for the denominator, in which the average associated with the indices α and β will become

$$\left\langle \mathbf{e}_j^\alpha \cdot \mathbf{e}_j^\beta \dot{x}_\alpha(0)\dot{x}_\beta(0)\right\rangle = \left\langle \mathbf{e}_j^\alpha \cdot \mathbf{e}_j^\beta \right\rangle \left\langle \dot{x}_\alpha(0)\dot{x}_\beta(0)\right\rangle \tag{10.6}$$

After substituting Eqs. (10.5) and (10.6) into Eq. (10.4), carrying out the summation for the index of $\beta$, and replacing $\mathbf{e}_j^\alpha \cdot \mathbf{e}_j^\alpha$ with $\hat{P}_j^\alpha$ given in Eq. (10.4), we obtain

$$C(t) \approx \frac{\sum_j^n \frac{1}{m_j} \sum_\alpha^{3n-6} \left\langle \hat{P}_j^\alpha \cos(\omega_\beta t)\right\rangle}{\sum_j^n \frac{1}{m_j} \sum_\alpha^{3n-6} \left\langle \hat{P}_j^\alpha \right\rangle} \tag{10.7}$$

Decomposing the vibrational INMs into the real- and imaginary-frequencies lobes, both numerator and denominator in Eq. (10.7) can be separated into two terms. Subsequently, by inserting the equalities $\int_0^\infty \delta(\omega-\omega_\alpha)d\omega = 1$ and $\int_0^\infty \delta(\lambda-\lambda_\alpha)d\lambda = 1$ into the terms associated the real- and imaginary-frequency lobes, respectively, the following is obtained

$$C(t) \approx \frac{\sum_j^n \frac{1}{m_j}\left(\int_0^\infty \left\langle \sum_\alpha^{\mathrm{Re}} \hat{P}_j^\alpha \delta(\omega-\omega_\alpha)\right\rangle \cos(\omega t)d\omega + \int_0^\infty \left\langle \sum_\alpha^{\mathrm{Im}} \hat{P}_j^\alpha \delta(\lambda-\lambda_\alpha)\right\rangle \cosh(\lambda t)d\lambda\right)}{\sum_j^n \frac{1}{m_j}\left(\int_0^\infty \left\langle \sum_\alpha^{\mathrm{Re}} \hat{P}_j^\alpha \delta(\omega-\omega_\alpha)\right\rangle d\omega + \int_0^\infty \left\langle \sum_\alpha^{\mathrm{Im}} \hat{P}_j^\alpha \delta(\lambda-\lambda_\alpha)\right\rangle d\lambda\right)} \tag{10.8}$$

where cos(ωt) for imaginary frequency ω=iλ has been replaced by cosh(λt). According to the definition of $D_j^{(s)}(\omega)$ and $D_j^{(u)}(\lambda)$ in Eq. (2.39), we have

$$C(t) \approx \frac{\sum_j^n \frac{1}{m_j}\left(\int_0^\infty D_j^{(s)}(\omega)\cos(\omega t)d\omega + \int_0^\infty D_j^{(u)}(\lambda)\cosh(\lambda t)d\lambda\omega\right)}{\sum_j^n \frac{1}{m_j}\left(\int_0^\infty D_j^{(s)}(\omega)d\omega + \int_0^\infty D_j^{(u)}(\lambda)d\lambda\right)} \tag{10.9}$$

# A.3 Hessian matrix of Gupta potential

For simplicity, we rewrite the general Gupta potential of a metallic cluster of $n$ atoms with mass $m_j$ ($j=1,\ldots n$), which may be of different species, in the form,

$$E_n(\boldsymbol{R}) = \sum_{i=1}^{n} \sum_{j=1(j\neq i)}^{n} u_{ij}(r_{ij}) - \sum_{i=1}^{n} U_i^{1/2} \tag{11.1}$$

where

$$u_{ij}(r) = A_{ij} \exp\left[-p_{ij}\left(\frac{r}{r_{ij}^{(0)}} - 1\right)\right] \tag{11.2}$$

and

$$U_i = \sum_{j=1(j\neq i)}^{n} \phi_{ij}(r_{ij}) \tag{11.3}$$

In which

$$\phi_{ij}(r) = \xi_{ij}^2 \exp\left[-2q_{ij}\left(\frac{r}{r_{ij}^{(0)}} - 1\right)\right] \tag{11.4}$$

The first and second terms of $E_n(\boldsymbol{R})$ describe pairwise and many-body interactions, respectively. The Hessian matrix elements $K_{j\mu,k\nu}(\boldsymbol{R})$ of the Gupta potential can be calculated by Eq. (2.9). For the pairwise interactions, they have been given previously, but for the many-body interactions the derivation of the Hessian matrix elements is, however, complicated. Here, we give only the explicit expressions, which are

$$K_{j\mu,k\nu}(R) = \begin{cases} \dfrac{-1}{\sqrt{m_j m_k}} W_{j\mu,k\nu}(\boldsymbol{R}) & j \neq k \\ \dfrac{1}{m_j} \displaystyle\sum_{l=1(l\neq j)}^{n} W_{j\mu,l\nu}(\boldsymbol{R}) & j \neq k \end{cases} \tag{11.5}$$

where

$$\begin{aligned} W_{j\mu,k\nu}(\boldsymbol{R}) = {} & 2\left(\overleftrightarrow{T}_{jk}(\vec{r}_{jk})\right)_{\mu\nu} - \frac{1}{2}\left(U_j^{-1/2} + U_k^{-1/2}\right)\left(\overleftrightarrow{S}_{jk}(\vec{r}_{jk})\right)_{\mu\nu} \\ & - \sum_{\substack{p=1 \\ (p\neq j, p\neq k)}}^{n} G_{jkp}\left(\overleftrightarrow{R}_{jkp}\right)_{\mu\nu} + \sum_{\substack{p=1 \\ (p\neq k)}}^{n} G_{jpk}\left(\overleftrightarrow{R}_{jpk}\right)_{\mu\nu} + \sum_{\substack{p=1 \\ (p\neq j)}}^{n} G_{pkj}\left(\overleftrightarrow{R}_{pkj}\right)_{\mu\nu} \end{aligned} \tag{11.6}$$

The first and second terms in $W_{j\mu,k\nu}(\boldsymbol{R})$ involve two particles and the last three terms involve three particles. For the two-body terms in $W_{j\mu,k\nu}(\boldsymbol{R})$, $\overleftrightarrow{T}_{jk}(\vec{r}_{jk})$ and $\overleftrightarrow{S}_{jk}(\vec{r}_{jk})$ are the 3 × 3 matrices expressed explicitly as

$$\overleftrightarrow{T}_{jk}(\vec{r}) = \frac{u'_{jk}(r)}{r}\overleftrightarrow{I}_3 + \left(u''_{jk}(r) - \frac{u'_{jk}(r)}{r}\right)\hat{r}\hat{r} \tag{11.7}$$

$$\overleftrightarrow{S}_{jk}(\vec{r}) = \frac{\phi'_{jk}(r)}{r}\overleftrightarrow{I}_3 + \left(\phi''_{jk}(r) - \frac{\phi'_{jk}(r)}{r}\right)\hat{r}\hat{r} \tag{11.8}$$

where $\hat{\mathrm{r}} = \vec{\mathrm{r}}/|\vec{\mathrm{r}}|$ and $\hat{\mathrm{r}}\hat{\mathrm{r}}$ is a $3 \times 3$ tensor and the prime and double-prime on $u_{jk}(r)$ and $\phi_{jk}(r)$ mean the first and second $r$ derivatives, respectively. Also, $\overleftrightarrow{I}_3$ is a $3 \times 3$ unit tensor. In contrast, for the three-body terms in $W_{j\mu,k\nu}(\boldsymbol{R})$, $j$ and $k$ denote the root particles and $p\ (\neq j,k)$ is a field particle, which is one to be summed. The quantity $\overleftrightarrow{R}_{jkp}$ is a $3 \times 3$ tensor given as $\overleftrightarrow{R}_{jkp} \equiv \hat{r}_{jp}\hat{r}_{kp}$ whose transpose, $\overleftrightarrow{R}^{+}_{jkp}$ satisfies $\overleftrightarrow{R}^{+}_{jkp} = \overleftrightarrow{R}_{jkp}$. Finally, the quantity $G_{jkp}$ is a three-body scalar function, which is related to $\phi_{jk}(r)$ as

$$G_{jkp} \equiv G_{jkp}(r_{jp}, r_{kp}) = \frac{U_p^{-3/2}}{4}\phi'_{jp}(r_{jp})\phi'_{kp}(r_{kp}) \tag{11.9}$$

Obviously, we have $G_{jkp} = G_{kjp}$. We shall apply Eq. (11.5) to determine the INM.

# Bibliography


[1] O. Echt, K. Sattler, and E. Recknagel, Phys. Rev. Lett. **47**, 1121 (1981).

[2] O. Echt *et al.*, Phys. Chem. **86**, 860 (1982).

[3] A. Ding, and J. Hesslich, Chem. Phys. Lett. **94**, 54 (1983).

[4] I. A. Harris, R. S. Kidwell, and J. A. Northby, Phys. Rev. Lett. **53**, 2390 (1984).

[5] J. C. Phillips, Chem. Rev. **86**, 619 (1986).

[6] I. A. Harris *et al*., Chem. Phys. Lett. **130**, 316 (1986).

[7] W. Miehle *et al*, J. Chem. Phys. **91**, 5940 (1989).

[8] D. C. Easter, *et al*., Chem. Phys. Lett. **157**, 277 (1989).

[9] D. C. Easter, R. L. Whetten, and J. E. Wessel, J. Chem. Phys. **94**, 3347 (1991).

[10] S. M. Beck, and J. H. Hecht, J. Chem. Phys. **96**, 1975 (1992).

[11] J. Farges *et al*., Surf. Sci. **106**, 95 (1981).

[12] S. S. Kim, and G. D. Stein, J. Colloid. Interface Sci. **87**, 180 (1982).

[13] J. Farges *et al*., J. Chem. Phys. **78**, 5067 (1983).

[14] J. Farges *et al*., J. Chem. Phys. **84**, 3491 (1986).

[15] J. W. Lee, and G. D. Stein, J. Phys. Chem. **91**, 2450 (1987).

[16] J. Farges *et al*., Adv. Chem. Phys. **70**, 45 (1988).

[17] P. Pawlow, Z. Phys. Chem. **65**, 1 (1909).

[18] P. Pawlow, Z. Phys. Chem. **65**, 545 (1909).

[19] M. Takagi, J. Phys. Soc. Jpn. **9 (3)**, 359 (1954).

[20] Ph. Buffat, and J. P. Borel, Phys. Rev. A **13**, 229 (1976).

[21] M. Schmidt *et al.*, Phys. Rev. Lett. **79**, 99 (1997).

[22] M. Schmidt *et al.*, Nature (London) **393**, 238 (1998).

[23] M. Schmidt *et al.*, Phys. Rev. Lett. **87**, 203402 (2001).

[24] M. Schmidt *et al.*, Phys. Rev. Lett. **86**, 1191 (2001).

[25] M. Schmidt, and H. Haberland, C. R. Physique **3**, 327 (2002).

[26] M. Schmidt *et al.*, Phys. Rev. Lett. **90**, 103401 (2003).

[27] Collen M. Neal, Anne K. Starace, and Martin F. Jarrold, J. Am. Soc. Mass Spectrum **18**, 74 (2007).

[28] D. J. Wales, *Energy Landscapes, with Applications to Clusters, Biomolecules and Glasses* (Cambridge University Press; Cambridge 2003).

[29] Y. Imry, Phys. Rev. B **21**, 2042 (1980).

[30] A. Hüller, Z. Phys. D **95**, 63 (1994).

[31] D. J. McGinty, J. Chem. Phys. **58**, 4733 (1973).

[32] C. L. Briant, and J. J. Burton, J. Chem. Phys. **63**, 2045 (1975).

[33] R. D. Etters, and J. Kaelberer, Phys. Rev. A **11**, 1068 (1975).

[34] R. D. Etters, and J. Kaelberer, J. Chem. Phys. **66**, 5112 (1977).

[35] J. Jellinek, T. L. Beck, and R. S. Berry, J. Chem. Phys. **84**, 2783 (1986).

[36] R. S. Berry et al., Adv. Chem. Phys. **90**, 75 (1988).

[37] R. S. Berry, Chem. Rev. **93**, 2379 (1993).

[38] H. P. Cheng, and R. S. Berry, Phys. Rev. A **45**, 7969 (1992).

[39] R. E. Kunz, and R. S. Berry, Phys. Rev. E **49**, 1895 (1994).

[40] R. S. Berry, *in Theory of Atomic and Molecular Clusters: with a Glimpse at Experiments* p. 1(Ed. J Jellinek, Springer Verlag, 1999).

[41] R. S. Berry, and B. M. Smirnov, Usp. Fiz. Nauk **175**, 367 (2005). [Phys. Usp. 48, 345 (2005)]

[42] C. M. Neal, A. K. Starace, and M. F. Jarrold, Phys. Rev. B **76**, 054113 (2007).

[43] B. Cao, A. K. Starace, C. M. Neal, M. F. Jarrold, S. Núñez, J. M. López, and A. Aguado, J. Chem. Phys. **129**, 124709 (2008).

[44] B. Cao, A. K. Starace, O. H. Judd, I. Bhattacharyya, and M. F. Jarrold, J. Chem. Phys. **131**, 124305 (2009).

[45] T.W. Yen, S. K. Lai, N. Jakse, and J. L. Bretonnet, Phys. Rev. B **75**, 165420 (2007).

[46] P. J. Hsu, J. S. Luo, S. K. Lai, J. F.Wax, and J. L. Bretonnet, J. Chem. Phys. **129**, 194302 (2008).

[47] T. L. Beck, J. Jellinek, and R. S. Berry, J. Chem. Phys. **87**, 545 (1987).

[48] T. L. Beck and R. S. Berry, J. Chem. Phys. **88**, 3910 (1988).

[49] D. J. Wales, J. Chem. Soc., Faraday Trans. **87**, 2399 (1991).

[50] J. D. Honeycutt and H. C. Andersen, J. Phys. Chem. **91**, 4950 (1987).

[51] R. M. Lynden-Bell and D. J. Wales, J. Chem. Phys. **101**, 1460 (1994).

[52] J. P. K. Doye and D. J. Wales, J. Chem. Phys. **102**, 9673 (1995).

[53] D. J. Wales, J. Chem. Phys. **101**, 3750 (1994).

[54] F. Calvo, Phys. Rev. E **82**, 046703 (2010).

[55] L. Zhan, J. Z. Y. Chen, and W. K. Liu, J. Chem. Phys. **127**, 141101 (2007).

[56] M. Picciani, M. Athènes, J. Kurchan, and J. Tailleur, J. Chem. Phys. **135**, 034108 (2011).

[57] F. Calvo and F. Spiegelmann, J. Chem. Phys. **112**, 2888 (2000).

[58] S. K. Lai, W. D. Lin, K. L. Wu, W. H. Li, and K. C. Lee, J. Chem. Phys. **121**, 1487 (2004).

[59] F. H. Stillinger and T. A. Weber, Phys. Rev. A **25**, 978 (1982); **28**, 2408 (1983).

[60] F. H. Stillinger and T. A. Weber, Science **225**, 983 (1984).

[61] R. M. Stratt, Acc. Chem. Res. **28**, 201 (1995).

[62] T. Keyes, J. Phys. Chem. A **101**, 2921 (1997).

[63] B. Madan, T. Keyes, and G. Seeley, J. Chem. Phys. **92**, 7565 (1990).

[64] T. M. Wu and R. F. Loring, J. Chem. Phys. **97**, 8568 (1992); Y. Wan and R. M. Stratt, J. Chem. Phys. **100**, 5123 (1994).

[65] S. D. Bembenek and B. B. Laird, Phys. Rev. Lett. **74**, 936 (1995); J. Chem. Phys. **104**, 5199 (1996).

[66] R. Schulz, M. Krishnan, I. Daidone, and J. C. Smith, Biophys. J. **96**, 476 (2009); C. Peng, L.

Zhang, and T. Head-Gordon, Biophys. J. **98**, 2356 (2010).
[67] D. J. Wales and T. V. Bogdan, J. Phys. Chem. B **110**, 20765 (2006).
[68] J. E. Adams and R. M. Stratt, J. Chem. Phys. **93**, 1332 (1990).
[69] J. E. Adams and R. M. Stratt, J. Chem. Phys. **93**, 1358 (1990).
[70] J. E. Adams and R. M. Stratt, J. Chem. Phys. **93**, 1632 (1990).
[71] G. Natanson, F. Amar, and R. S. Berry, J. Chem. Phys. **78**, 399 (1983); R. S. Berry, J. Jellinek, and G. Natanson, Phys. Rev. A **30**, 919 (1984).
[72] F. G. Amar and R. S. Berry, J. Chem. Phys. **85**, 5943 (1986).
[73] H. L. Davis, J. Jellinek, and R. S. Berry, J. Chem. Phys. **86**, 6456 (1987).
[74] T. L. Beck, D.M. Leitner, and R. S. Berry, J. Chem. Phys. **89**, 1681 (1988).
[75] R. S. Berry and D. J. Wales, Phys. Rev. Lett. **63**, 1156 (1989).
[76] D. J. Wales and R. S. Berry, J. Chem. Phys. **92**, 4473 (1990).
[77] D. J. Wales and R. S. Berry, J. Chem. Phys. **92**, 4283 (1990).
[78] D. J. Wales and R. S. Berry, Phys. Rev. Lett. **73**, 2785 (1994).
[79] P. H. Tang, T.M.Wu, T. W. Yen, S. K. Lai, and P. J. Hsu, J. Chem. Phys. **135**, 094302 (2011).
[80] P. H. Tang, T.M.Wu, P. J. Hsu, and S. K. Lai, J. Chem. Phys. **137**, 244304 (2012).
[81] T. W. Yen, P. J. Hsu, and S. K. Lai, e-J. Surf. Sci. Nanotechnol. **7**, 149 (2009).
[82] P. M. Chaikin and T. C. Lubensky, *Principles of Condensed Matter Physics* (Cambridge University Press, Cambridge, 1995).
[83] I. L. Garsón and A. Posada-Amarillas, Phys. Rev. B **54**, 11796 (1996).
[84] J. Jellinek and D. H. Li, Phys. Rev. Lett. **62**, 241 (1989).
[85] M. Page and J. W. Mclver, J. Chem. Phys. **88**, 922 (1988).
[86] T. M. Wu and R. F. Loring, J. Chem. Phys. **99**, 8936 (1993).
[87] M. Buchner, B. M. Ladanyi, and R. M. Stratt, J. Chem. Phys. **97**, 8522 (1992).
[88] R. L. Carter, *Molecular Symmetry and Group Theory* (Wiley, New York, 1998).
[89]R. Mcweeny, B. Sc and D. Phil, *Symmetry* Chaps. 3 (Pergamon Press, Oxford, London,1963).
[90] P. J. Hsu and S. K. Lai, J. Chem. Phys. **124**, 044711 (2006).
[91] G. Rossi, A. Rapallo, C. Mottet, A. Fortunelli, F. Baletto, and R. Ferrando, Phys. Rev. Lett. **93**, 105503 (2004).
[92] A. Rapallo, G. Rossi, R. Ferrando, A. Fortunelli, B. C. Curley, L. D. Lloyd, G. M. Tarbuck, and R. L. Johnston, J. Chem. Phys. **122**, 194308 (2005).
[93] R. P. Gupta, Phys. Rev. B **23**, 6265 (1981).
[94] C. Mottet, G. Treglia, and B. Legrand, Phys. Rev. B **46**, 16018 (1992).
[95] Private communication with Prof. S. K. Lai at Department of physics, National Central University, Taiwan.
[96] T. M. Wu and S. F. Tsay, J. Chem. Phys. **105**, 9281 (1996).
[97] T. M. Wu, S. L. Chang, S. F. Tsay, and K. H. Tsai, J. Non-Cryst. Solids **352**, 4615 (2006).
[98] D. J. Wales and J. P. K. Doye, J. Chem. Phys. **103**, 3061 (1995).

[99] A. Posada-Amarillas and I. L. Garzón, Phys. Rev. B **54**, 10362 (1996).

[100] Y. Wan and R. M. Stratt, J. Chem. Phys. **100**, 5123 (1994).

[101] D. J. Wales, J. P. K. Doye, M. A. Miller, P. N. Mortenson, and T. R. Walsh, "Energy landscapes: From clusters to biomolecules," in *Advances in Chemical Physics*, edited by I. Prigogine and S. A. Rice (Wiley, 2000), Vol. 115, Chap. I.

[102] Y. Kumeda, L. J. Munro, and D. J. Wales, Chem. Phys. Lett. **341**, 185 (2001).

[103] S. A. Trygubenko and D. J. Wales, J. Chem. Phys. **120**, 2082 (2004).

[104] W. H. Press, S. A. Teukolsky, W. T. Vetterling, and B. P. Flannery, *Numerical Recipes in C*, 2nd ed. (Cambridge University Press, Cambridge 1992).

[105] D. J. Wales, Mol. Phys. **100**, 3285 (2002).

[106] D. J. Wales, Mol. Phys. **102**, 891 (2004).

[107] D. A. McQuarrie, *Statistical Mechanics* Chaps. 21, 22 (Harper & Row, New York, 1976).

[108] R.Zwanzig, J. Chem. Phys. **79**, 4507 (1983).

[109] H. Zabrodsky, S. Peleg, and D. Avnir, J. Am. Chem. Soc. **114**, 7843 (1992).